Department of Physics and Astronomy

University of Heidelberg

Master thesis in Physics

submitted by

Lukas Josef Spieß

born in Wangen im Allgäu (Germany)

2018

Setup of a vibration-suppressed cryogenic system for a RF ion trap with minimum micromotion

This Master thesis has been carried out by Lukas Josef Spieß
at the Max Planck Institute for Nuclear Physics
under the supervision of
Priv.-Doz. Dr. José Ramón Crespo López-Urrutia

Aufbau eines schwingungsarmen kryogenen Systems für eine RF-Ionenfalle mit reduzierter Mikrobewegung:

Neuste Fortschritte ermöglichen das sympathetische Kühlen von hochgeladenen Ionen (HCI) auf mK Temperaturen in einer kryogenen linearen Paul-Falle. Dies macht Hochpräzisionsspektroskopie von HCI möglich, was den Weg für die Suche nach neuer Physik und neuartigen optischen Uhren ebnet. Dafür wird eine hochstabile und gut verstandene Paul-Falle benötigt. Besonders zusätzliche Mikrobewegung muss charakterisiert und reduziert werden, da diese die niedrigste erreichbare Ionentemperatur und somit Präzision von Spektroskopie limitieren kann. Während dieser Arbeit wurde eine neue kryogene Zuleitung teilweise aufgebaut, welche durch Vibrationsentkopplung die Stabilität der Speicherung erhöht. Bei der ersten Abkühlung wurde eine Temperatur von 4,23 K in der Fallenumgebung erreicht, wodurch der vorgesehene RF Paul-Fallen-Resonator aus Niob supraleitend betrieben werden kann. Weiterhin wurde eine Photonkorrelationsmethode an der bereits existierenden kryogenen linearen Paul-Falle mit $^{9}Be^{+}$ Ionen angewandt um die Fallenfrequenz aus einer Messung der Phasenverschiebung zwischen der Bewegung getriebener Ionen und der treibenden Kraft zu bestimmen. Aus der Fallenfrequenz wurde die Vergrößerung des Abbildungsystems ermittelt???. Dieselbe Photonkorrelationstechnik wurde verwendet um die zusätzliche Mikrobewegung zu messen und um deren Reduktion um einen Faktor von nahezu 100, im Vergleich zu einer früheren Messung, zu zeigen.

Setup of a vibration-suppressed cryogenic system for a RF ion trap with minimum micromotion:

Recent advancements allow for sympathetic cooling of highly charged ions (HCI) to mK temperatures in a cryogenic linear Paul trap. This makes high precision spectroscopy of HCI possible, paving the way to the search for new physics and novel optical clocks. For this, a highly stable and well-understood Paul trap is required. In particular, excess micromotion needs to be characterized and reduced, since it can limit the lowest achievable ion temperature and therefore spectroscopic precision. Within this thesis, a new cryogenic supply system was partly assembled, which allows for vibrational decoupling of the trap, increasing storage stability. The first cool down test achieved a temperature of 4.23 K in the trap environment, which is sufficiently low for superconductive operation of the intended RF-resonator made from niobium. Additionally, a photon-correlation technique was used on the existing cryogenic linear Paul trap using $^{9}Be^{+}$ ions for determination of the trap frequency by measuring the phase shift between the driven ions motion and the driving field. From the trap frequency the magnification of the imaging system is deduced. The same photon-correlation technique is used to measure excess micromotion and to demonstrate its reduction by a factor of 100 compared to a previous measurement by using new electronics.

Contents

1 Motivation **1**

2 Theory **5**

2.1 The linear Paul trap 5

2.2 Doppler cooling 9

2.3 Coulomb crystallization 14

2.3.1 Ion chains 15

2.4 The driven harmonic oscillator 19

2.5 Nonlinear optics 20

2.5.1 Second harmonic generation 21

2.5.2 Three-wave mixing 22

2.6 Optical resonators 24

2.6.1 The Fabry-Pérot resonator 24

2.6.2 Frequency stabilization 27

2.6.2.1 Hänsch-Couillaud method 27

2.6.2.2 Pound-Drever-Hall method 29

3 The cryogenic Paul trap **35**

3.1 The cryogenic system 35

3.2 Electronics 37

3.3 Optical arrangement 38

4 Generation and cooling of $^{9}Be^{+}$ **41**

4.1 Beryllium oven 41

4.2 Photoionization laser 41

4.3 Laser cooling of $^{9}Be^{+}$ 43

4.4 Temperature estimation 48

5 Measuring coherent ion motion **51**

5.1 Characterization of the ADC 53

5.1.1 Temporal resolution 53

5.1.2 Normalisation 53
5.1.3 Time calibration 54
5.2 Centre of mass mode 55
5.3 Magnification of the imaging system 62
5.4 Axial excess micromotion 65

6 CryPTEx II **69**
6.1 The cryogenic supply 69
6.2 Cooling down 75

7 Summary and outlook **79**

Bibliography **81**

Chapter 1

Motivation

Todays most successful physics model is arguably the Standard Model of particle physics. It describes the weak, strong and electromagnetic interaction as well as all known fundamental particles; only gravity remains unexplained in this approach. Within the Standard Model all forces are mediated by gauge bosons and their coupling strength is described by a constant. These fundamental constants of nature can not be predicted by theory and have to be measured. For the electromagnetic force the carrier is the photon, coupling to electric charge and the interaction strength is given by the fine structure constant

$$\alpha = \frac{e^2}{4\pi\epsilon_0\hbar c}, \tag{1.1}$$

with e the elementary charge, ϵ_0 the vacuum permittivity, $\hbar$ the reduced Planck constant and c the speed of light. The currently recommended value from CODATA for α is for historical reasons often given in the form $1/\alpha = 137.035999139(31)$ [1].

In the search for physics beyond the Standard Model, a variety of theories were developed of which some predict that the fundamental constants, including α, are actually not constant but vary on cosmological time scales [2]. The earliest argument for varying constants goes probably back to Dirac, who in 1937 argued for a variation of the gravitational constant G over time [3, 4]. Since then many experiments have been performed in the search for such behaviour, for example of G, α and the proton-to-electron mass ratio $\mu = m_p/m_e$ [5]. These measurements are usually performed either in laboratories with high precision on the time scale of a few years or using cosmological measurements which provide large times scales but have limited precision [5].

So far no measurement revealed a significant change in any fundamental constant expect for a result from Webb et al. [6], where the spectra of quasars taken with

the Keck and Very Large Telescope were analysed. This showed a significant spatial variation of α at the 4.2σ level, which was best described by a dipole, often called the Australian dipole. This result is ground-breaking if correct though it needs to be verified independently, preferably with a laboratory experiment. As of now this was not possible due to the required precision. The predicted spatial variation throughout the universe would on earth correspond to a temporal variation due to the movement of the earth through the proposed dipole, resulting in a relative change of [7]

$$\frac{\dot{\alpha}}{\alpha}\Big|_{\text{earth}} \approx 10^{-19}\,\text{yr}^{-1}. \tag{1.2}$$

One promising candidate to achieve such an accuracy are optical clocks [7, 8, 9]. For these, the frequency of an electronic transition in the optical regime is measured with high precision. These frequencies are optimal candidates for the search of α variation, since relative uncertainties below 10^{-17} have been achieved [10, 11, 12]. The change δE of a transition energy E_0 due to a variation of α is usually described by

$$\frac{\delta E}{E_0} = \frac{2q'}{E_0}\frac{\delta\alpha}{\alpha} \equiv K\frac{\delta\alpha}{\alpha}, \tag{1.3}$$

where q' is a factor describing the sensitivity of the particular transition to a change of α and K is the dimensionless analogue. For most transitions of atoms and singly charged ions (e.g. Sr, Al^+, Hg^+) used in optical clocks today, K is of the order of 1 or below as given in Tab. 1. The currently best limit with respect to α variation using conventional ions is

$$\frac{\dot{\alpha}}{\alpha} = (1.6 \pm 2.3) \times 10^{-17}\,\text{yr}^{-1} \tag{1.4}$$

from Rosenband et al. [13], showing no significant deviation from zero. For this measurement, the frequencies of an Al^+ and a Hg^+ optical transition ($\Delta K \approx -2.9$) were compared over the course of a year. Though this result already achieved a high precision, it is still two orders of magnitudes short of the predicted change by Webb et al. For a further improvement, either the precision needs to be increased or transitions with larger values for K need to be used.

For this purpose, highly charged ions (HCI) were suggested as candidates for new optical clocks due to a high sensitivity to α variation for certain transitions [14, 16]. Most transitions of HCI are in the X-ray regime due to the valence electrons being bound closely to the nucleus and the correspondingly large electric fields. In some cases though, level crossings appear which generate optical transitions. Some of these have been shown to exhibit large values for K. Examples are given in Tab. 1. A particular interesting candidate is Ir^{17+}, since it not only

Table 1: Sensitivity factor K for α variation for some commonly used clock atom and singly charged ion transitions as well as some proposed transitions in HCI [8, 14, 15, 16].

Atom	**Sensitivity factor K**	**Wavelength λ (nm)**
Sr	0.06	689
Al^+	0.008	267
Hg^+	-2.9	282
Ir^{17+}	-20.6	≈ 267
Ir^{17+}	145	≈ 1960
Pr^{10+}	40	≈ 2700
Pr^{10+}	22	≈ 1400

has multiple transitions with large K values, but also with opposite signs for K, further increasing the sensitivity [14]. This allows for $\Delta K > 100$ using two transitions of the same HCI, an increase of more than one order of magnitude compared to the ions used by Rosenband et al.

The production of HCI requires high energies to remove the necessary amount of electrons. This results in high temperatures ($\approx$ MK) and a cooling scheme is required to allow for high precision spectroscopy. At CryPTEx (cryogenic Paul trap experiment) [17], Ar^{13+} was the first sympathetically cooled HCI in a cryogenic linear Paul trap, bringing its temperatures down to $\approx 10\,\mathrm{mK}$ [18, 19, 20]. For this, $^9Be^+$ ions are stored and laser cooled inside a cryogenic linear Paul trap. Ar^{13+} ions are produced in an electron beam ion trap (EBIT) at MK and are transferred to the Paul trap through a beam line. There they are injected and thermalise with the $^9Be^+$ ions achieving temperatures in the mK regime. This progress gives access to the advantages of the large variety of HCI compared to neutral or singly charged ions for spectroscopy.

While α variation is certainly an important and interesting application for cold, stored HCI, other tests of fundamental physics are possible [21]. For example, trapped ions can be used in a Michelson-Morley like experiment to test local Lorentz invariance (LLI). For this, the wavepacket of an electron is split anisotropically and recombined after some time. The interference of the two parts of the wavepacket gives access to LLI due to the motion of the earth. This has so far only been done with Ca^+ ions [22], but it has been shown that certain HCI have a particularly high sensitivity to LLI violation [23].

Electronic transitions of HCI are mostly in the extreme ultraviolet regime (XUV), since the valence electrons experience much larger electric fields compared to neutral atoms with the same amount of electrons. Recent advancements allowed for

operation of frequency combs in the XUV from the infrared using high harmonic generation [24, 25]. This might open a way to new frequency standards based on HCI, with higher precisions than currently achievable with optical clocks [26].
In this thesis CryPTEx II, the successor experiment of CryPTEx, was partly assembled. It is expected to achieve longer storage times for HCI, due to better mechanical stability as well as a more stable trapping potential. This will make ground-state cooling and quantum logic spectroscopy [27] available for high precision spectroscopy. Assembly of CryPTEx II is still going on by the end of this thesis. Therefore, laser cooled $^{9}Be^{+}$ ions were stored in its predecessor CryPTEx and a photon-correlation technique [28] was used to demonstrate characterization of the trapping frequencies, imaging system and micromotion. In particular, a reduction of axial excess micromotion is shown compared to a previous measurement [29]. This is important, since micromotion can limit the temperature achievable through Doppler cooling [28] and can cause time-dilations shifts, which can restrict high precision spectroscopy [30]. The used techniques can also be applied to CryPTEx II, where a small micromotion is important, since ground-state cooling requires an initial temperature close to the Doppler limit.

Chapter 2

Theory

In this chapter the theoretical models relevant for this thesis are discussed. At the beginning, the linear Paul trap for storage of ions is explained as well as the resulting motion in such a trap, consisting of a secular motion and micromotion. Then Doppler cooling is examined, which makes it possible to cool stored ions to temperatures in the mK regime. The next part covers the ordered structures of such cold, stored ions form, called Coulomb crystals. In particular, the case of a 1-dimensional ion chain is looked at. Furthermore, the driven harmonic oscillator is reviewed, which can be used to approximately describe the ion motion if it becomes driven. In the last two parts nonlinear optics and optical resonators are discussed, which are vital to the used optical setups and permit the generation of lasers beams for production and cooling of $^9Be^+$ ions.

2.1 The linear Paul trap

Electric fields are a natural choice for the storage of ions due to their strong coupling to charges. Earnshaw's theorem makes it impossible to generate a purely electrostatic potential with a global minimum. Therefore, a combination of dynamic and static electric fields is used to confine ions. The linear Paul trap is one example of such an ion trap. The following chapter is based on [28] and [31].
For the radial confinement a quadrupole field is used, which is described by the electric potential

$$\phi = \frac{\phi_0}{r_0^2}(\alpha x^2 + \beta y^2 + \gamma z^2). \tag{2.1}$$

The generated potential of four hyperbolically shaped electrodes in the setup shown in Fig. 2.1 gives for Eq. (2.1)

$$\phi = \frac{\phi_0}{r_0^2}(x^2 - y^2), \tag{2.2}$$

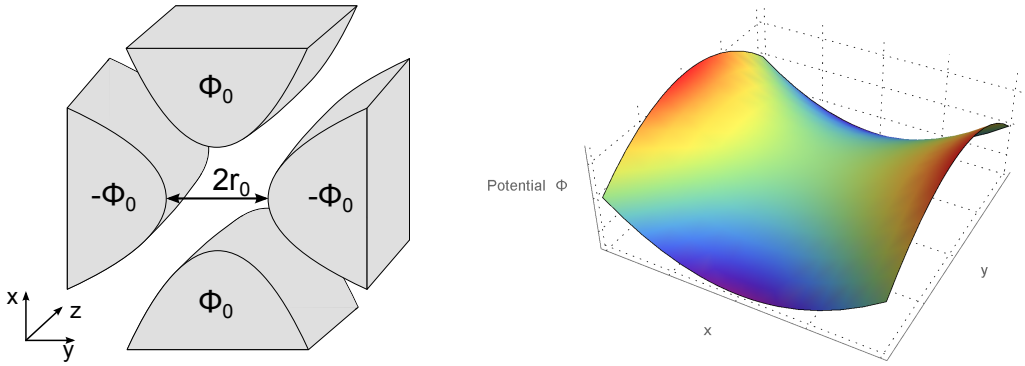

Figure 2.1: Left: Scheme of an ideal Paul trap with hyperbolic electrodes for radial trapping. The end-cap electrodes for axial trapping are not shown. **Right**: Resulting radial electric potential from the setup on the left. Both images are taken from [29].

where $\pm\phi_0/2$ is the electrode voltage on each pair of opposite lying electrodes and $2r_0$ is the length of the trap diagonal. The resulting radial potential shown in Fig. 2.1 has a saddle point at $(x, y) = (0, 0)$ and therefore a particle resting at this position is unstable, as predicted by Earnshaw's theorem. To overcome this a periodic change of the polarity of $\phi(t)$ is used, which can be described by

$$\phi(t) = \frac{V}{r_0^2}(x^2 - y^2)\cos(\Omega t), \tag{2.3}$$

where $V\cos(\Omega t)$ is a radio frequency (RF) voltage supplied to each quadrupole electrode. For axial confinement, two end-cap electrodes at a DC voltage of U are used. The potential near the centre caused by these can be approximated by

$$\phi_z = \frac{\kappa U}{z_0^2}\left[z^2 - \frac{1}{2}(x^2 + y^2)\right], \tag{2.4}$$

where κ is a geometric factor and $2z_0$ is the distance between the end-cap electrodes. The total potential is then given by

$$\phi(x, y, z, t) = \frac{V}{r_0^2}(x^2 - y^2)\cos(\Omega t) + \frac{\kappa U}{z_0^2}\left[z^2 - \frac{1}{2}(x^2 + y^2)\right]. \tag{2.5}$$

The equations of motion of a particle with mass m and charge Q in such a potential are

$$\frac{\mathrm{d}^2 u}{\mathrm{d}\tau^2} + (a_u + 2q_u\cos(2\tau))u = 0 \qquad (u = x, y, z), \tag{2.6}$$

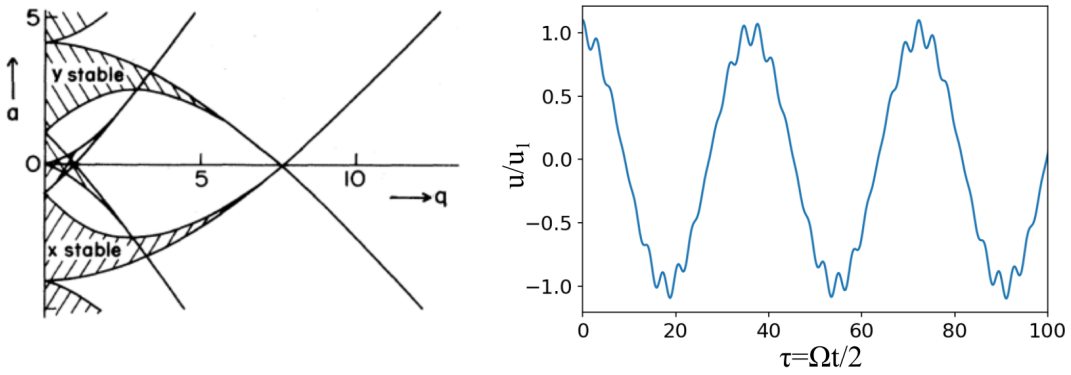

Figure 2.2: Left: Stability diagram for the motion of an ion in an ideal Paul trap in x- and y-direction for $a = a_x = a_y$ and $q = q_x = -q_y$. Only the overlapping region for $0 < a, q < 1$ is experimentally relevant. Adapted from [31]. **Right**: Motion of an ion in an ideal Paul trap in radial direction for $q = 0.2$ and $a = 0.01$. The motion is dominated by the secular motion at a frequency $\omega_{x/y}$ given by Eq. (2.11). Modulations at frequency Ω are caused by micromotion and increase with the distance to the trap centre.

with the dimensionless parameters

$$a_x = a_y = -\frac{1}{2}a_z = -\frac{4q\kappa U}{m\Omega^2 z_0^2}, \tag{2.7}$$

$$q_x = -q_y = \frac{4QV}{m\Omega^2 r_0^2}, \quad q_z = 0, \tag{2.8}$$

$$\tau = \frac{1}{2}\Omega t. \tag{2.9}$$

The Eq. (2.6) are known as Mathieu equations and have two different types of solutions:

1. Stable solutions: The particle oscillates with a limited amplitude in x- and y-direction for all times.

2. Unstable solutions: The motional amplitude in x- and/or y-direction increases exponentially.

The solution type depends only on the parameters a and q, and the stability diagram for the x- and y-direction is shown in Fig. 2.2. In the overlapping regions where x- and y-motion are simultaneously stable, trapping is possible. Experimentally the region close to $(a, q) = (0, 0)$ is commonly used. The motion in z-direction is always stable if the kinetic energy is smaller than the axial trap depth.
For typical experimental parameters $|a| \ll 1$ and $|q| \ll 1$, the first order solution

of Eq. (2.6) is

$$u(t) \approx u_1 \cos(\omega_u t + \varphi_u) \left[1 + \frac{q_u}{2} \cos(\Omega t)\right], \tag{2.10}$$

with

$$\omega_u \approx \frac{\Omega}{2} \sqrt{a_u + \frac{1}{2} q_u^2}. \tag{2.11}$$

From Eq. (2.10), it can be seen that the motion of the ion in radial direction can be decomposed into a secular motion at frequency ω_u and a a so called micromotion at frequency Ω. The latter is caused by the RF field which drives the ion, hence it is coherent with the RF field. An example for the radial motion in an ideal Paul trap is shown in Fig. 2.2. In axial direction $q_z = 0$ holds, micromotion does not exist and the particle moves harmonically with a frequency ω_z given by equation Eq. (2.11). The secular motion is an incoherent, thermal motion, in contrast to the driven micromotion. Laser cooling can only reduce the energy in secular motion. This reduces its amplitude u_1 and correspondingly the amplitude (and therefore energy) of the micromotion is reduced.

For the case of an ideal Paul trap only micromotion in radial direction, which is proportional to the amplitude of the secular motion exists. In a real trap, additional micromotion can be caused by multiple effects. For example, assuming there exists an additional static electric field $\vec{E}_{\mathrm{DC}}$ interacting with the trapped ion, Eq. (2.6) becomes

$$\frac{\mathrm{d}^2 u}{\mathrm{d}\tau^2} + (a_u + 2q_u \cos(2\tau))u = \frac{Q E_{\mathrm{DC},u}}{m} \tag{2.12}$$

and the solution to lowest order is given by

$$u(t) \approx [u_0 + u_1 \cos(\omega_u t + \varphi_u)] \left[1 + \frac{q_u}{2} \cos(\Omega t)\right], \tag{2.13}$$

where

$$u_0 \approx \frac{Q E_{\mathrm{DC},u}}{m \omega_u^2}. \tag{2.14}$$

The field $\vec{E}_{\mathrm{DC}}$ moves the central position of the ion to u_0 and introduces an oscillation with amplitude $u_0 q_u/2$ and frequency Ω. This additional motion is called excess micromotion, since in principle it can be avoided. It can not be reduced by laser cooling, since it is driven.

Excess micromotion can also be caused by a phase difference φ_{AC} between electrodes of the same phase, e.g. electrodes along the x-axis. This results in an additional driven motion of the ion at frequency Ω with a amplitude $q_x r_0 \rho \varphi_{\mathrm{AC}}$ along the x-axis, where ρ depends on the geometry of the trap (for the calculations see [28]).

Like any other motion, micromotion introduces a Doppler shift, which modifies the interaction of the trapped ion with a light field (see Sec. 2.2). For typical experimental parameters micromotion is harmonic with a velocity $\vec{v}$. The Doppler shift with respect to a light field with wavevector $\vec{k}$ ($|\vec{k}| = 2\pi/\lambda = 2\pi\nu/c$, λ: wavelength of the light, c: speed of light) can to lowest order be described as

$$\vec{k}\vec{v}(t) = v_{\max}\cos(\Omega t + \varphi), \tag{2.15}$$

where $v_{\max}$ is the velocity amplitude and φ describes a phase shift between RF field and ion motion.
Micromotion is the limiting factor when using Doppler cooling (see Sec. 2.2) in a Paul trap. The secular motion can in principle cooled down to the Doppler limit, since it is a thermal motion. Micromotion on the other hand is a driven motion and can therefore not be cooled through laser cooling and it can modify the absorption spectrum in such a way that heating occurs when cooling is expected [28]. Hence, it is essential to reduce excess micromotion to a minimum to allow for temperatures near the Doppler limit. A measurement of the axial excess micromotion at CryPTEx is given in Sec. 5.4.
From Eq. (2.10) it can be seen that the motion is dominated by the secular motion if $|a| \ll 1$ and $|q| \ll 1$. Therefore, it is often convenient to describe the system with a harmonic pseudopotential

$$\phi_{\text{Pseudo}} = \frac{1}{2}m(\omega_x^2 x^2 + \omega_y^2 y^2 + \omega_z^2 z^2) \tag{2.16}$$

with the trap frequencies

$$\omega_x = \omega_y = \sqrt{2\left(\frac{QV}{m\Omega r_0^2}\right)^2 - \frac{Q\kappa U}{mz_0^2}}, \tag{2.17}$$

$$\omega_z = \sqrt{\frac{2Q\kappa U}{mz_0^2}}. \tag{2.18}$$

The system is then identical to a 3-dimensional harmonic oscillator.

2.2 Doppler cooling

Doppler cooling is a commonly used method to cool atoms and ions through their interaction with a light field. It is based on photons having a momentum of $\hbar\vec{k}$ and therefore, if an atom absorbs a photon, the momentum of the atom changes as well as its internal state. This, combined with spontaneous emission

being isotropic, allows for a directed transfer of momentum (and therefore kinetic energy) over many absorption-emission cycles. The atom-light interaction also depends on velocity through the Doppler shift and allows in that way for cooling. For simplicity, only the non-relativistic case will be discussed here and it is assumed that the atom can be approximated by a two-level system with a ground and an excited state, which can be coupled through a laser field. The following discussion is based on [32] and [33].
Assume there to be an atom of mass m with a velocity $\vec{v}$ in the laboratory frame. Let there also be a monochromatic laser beam with a frequency ν parallel or antiparallel to the atoms trajectory and with a detuning of δ with respect to the electronic transition of the atom. Due to their relative motion, the frequency of the photons is Doppler shifted in the reference frame of the atom by

$$\delta_{\text{Doppler}} = -\vec{k} \cdot \vec{v} = \pm|\vec{k}||\vec{v}|. \tag{2.19}$$

The sign depends on whether the atom moves towards the photons (+) or away from them (−). The total detuning is then given by

$$\Delta = \delta + \delta_{\text{Doppler}} = \delta \pm |\vec{k}||\vec{v}|. \tag{2.20}$$

The probability for the atom to absorb a photon depends strongly on the ratio of the natural linewidth of the transition Γ and the total detuning Δ. It becomes most probable for

$$\Delta = 0 \iff \pm|\vec{k}||\vec{v}| = -\delta. \tag{2.21}$$

For $\delta < 0$ (red detuned case), the atom and the laser beam need to move towards each other to match this condition for resonance. For $\delta > 0$ (blue detuned case) they need to move collinearly. In the blue detuned case the momentum of the atom will increase for each absorbed photon, since absorption changes the momentum of the atom by $\hbar\vec{k}$. In the red detuned case the absorption of a photon reduces the momentum. Therefore, only red detuning with the laser beam directed towards the atom is experimentally relevant for cooling.
If the atom absorbs a photon, it becomes excited and gains the momentum $\hbar\vec{k}$. The atom will then deexcite by emitting a photon and return to its ground state. The second step can happen via two different possible processes illustrated in Fig. 2.3a:

1. **Stimulated emission:** the photon is emitted into the direction of the laser. This means the atom gains the momentum $-\hbar\vec{k}$, i.e. the overall state of the atom has not changed after one absorption-emission cycle.

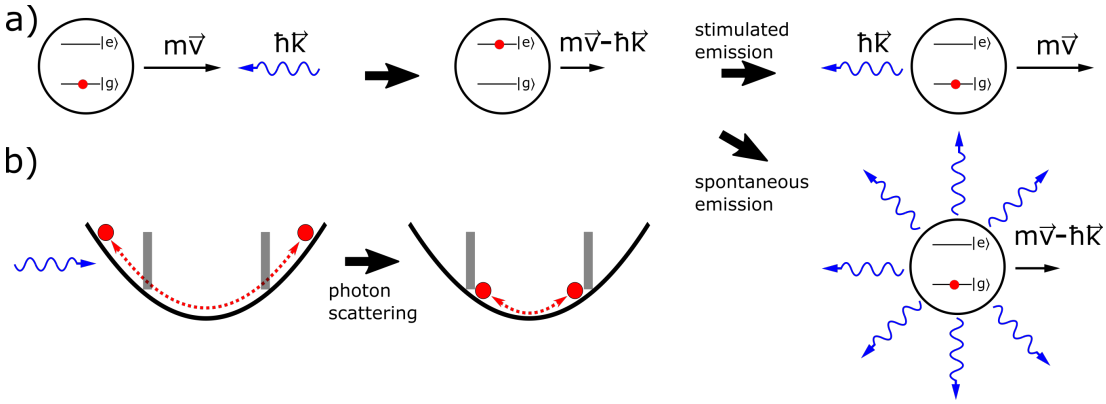

Figure 2.3: **(a)** Illustration of an absorption-emission cycle. An atom (black) of mass m described by a two-level system moves with a velocity $\vec{v}$. A counter propagating red-detuned photon (blue) with momentum $\hbar\vec{k}$ can be absorbed if the Doppler shift caused be the relative motion of photon and atom compensates the detuning. After absorption the atom momentum becomes reduced by $\hbar\vec{k}$ and the atom is excited. For deexcitation of the atom there are two possible pathways. Firstly, stimulated emission, where a photon identical to the initial photon is produced and the overall state of the atom did not change. Alternatively, spontaneous emission generates a photon in a random direction, which on average does not change the momentum of the atom, i.e. the momentum of the atom was reduced by $\hbar\vec{k}$. **(b)** A harmonically trapped particle is only resonant during a certain time window (grey box) when the velocity of the ion allows for resonant coupling of the laser to the particle. Laser cooling reduces its kinetic energy until it no longer becomes resonant with the laser.

2. **Spontaneous emission:** the photon is emitted isotropically. Averaged over many emission cycles this does not change the momentum, and therefore the total averaged momentum change of the atom for each absorption-emission cycle is $\hbar\vec{k}$.

Therefore, only spontaneous emission allows for cooling of the atom. The average reduction in speed per absorption-spontaneous emission cycle is given by the recoil speed

$$v_r = \frac{\hbar|\vec{k}|}{m}. \tag{2.22}$$

Hence, with each cycle of absorption followed by spontaneous emission the laser will be farther red detuned to the transition in the frame of the atom, reducing the likelihood of scattering. To allow for further momentum transfer a change of the laser frequency or the transition energy (e.g. Zeeman Slower [34]) is required. Another possibility is to artificially broaden the transition linewidth (e.g. by power broadening) to stay resonant over a wider range of frequencies.
To get a quantitative description, the average force due to continuous scattering

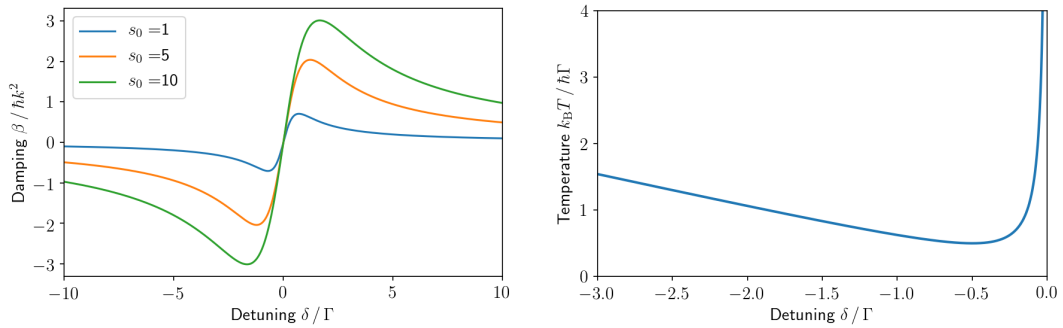

Figure 2.4: Left: Damping coefficient β as a function of the total detuning for different saturation parameters. **Right:** Steady-state temperature of the atom achieved by Doppler cooling as a function of the laser detuning for $\xi = 1$. The lowest temperature is achieved for $\delta/\Gamma = -1/2$.

of photons from the atom is used:

$$\langle \vec{F} \rangle = \hbar \vec{k} \Gamma \rho_{ee} \tag{2.23}$$
$$= \frac{\hbar \vec{k} \Gamma s_0}{2(1 + s_0 + (2(\delta - \vec{k}\vec{v})/\Gamma)^2)}.$$

Here ρ_{ee} is the probability of the atom to be in the excited state and the saturation parameter

$$s_0 = \frac{I}{I_s} \tag{2.24}$$

was introduced, which depends on the saturation intensity of the transition

$$I_s = \frac{\pi \hbar c \Gamma}{3\lambda^3}. \tag{2.25}$$

Assuming that the velocity is small ($|\vec{k}\vec{v}| \ll \Gamma$) a Taylor expansion of Eq. (2.23) to first order yields

$$\langle \vec{F} \rangle \approx \frac{\hbar \vec{k} \Gamma s_0}{2(1 + s_0 + (2\delta/\Gamma)^2)} + \frac{4\hbar \vec{k}(\vec{k}\vec{v})\delta s_0}{\Gamma(1 + s_0 + (2\delta/\Gamma)^2)^2} \tag{2.26}$$
$$= \vec{F}_0 + \beta \vec{v}, \tag{2.27}$$

where F_0 is a velocity-independent force, which does not contribute to cooling and β is a damping coefficient, which is plotted in Fig. 2.4. From Fig. 2.4 it can be seen that only for red detuning the atom's motion is damped, while for blue detuning it becomes accelerated, as previously noted.
So far it was neglected that Doppler cooling is a statistical process, which gives a

lower bound to the achievable temperature. The atom performs a random walk, since during each spontaneous emission it gains the momentum $\hbar\vec{k}$ in a random direction. This leads to an atom temperature

$$k_{\mathrm{B}}T = \frac{(1+\xi)\hbar((\Gamma/2)^2+\delta^2)}{-4\delta}, \tag{2.28}$$

where k_{B} is the Boltzmann constant and ξ takes into account the angular distribution of the photon emission and is of order 1. Eq. (2.28) is plotted in Fig. 2.4 for $\xi = 1$. The lowest energy is achieved for $\delta = -\Gamma/2$ and is given by

$$\begin{aligned} k_{\mathrm{B}}T_{\mathrm{D}} &= \frac{(1+\xi)\hbar\Gamma}{4} \\ &\approx \frac{\hbar\Gamma}{2}, \end{aligned} \tag{2.29}$$

which is the so called Doppler limit. Note that this result only holds in the case of $s_0 \to 0$, since otherwise power broadening occurs and the natural linewidth Γ has to be replaced with the effective linewidth $\Gamma_{\mathrm{eff}} = \Gamma\sqrt{1+s_0}$, i.e. the minimal temperature increases.

The previous discussion treated a free particle with a classical motion, though experimentally the ion is trapped in an approximately harmonic potential characterized by the trap frequency ω (see Sec. 2.1). This is described by the position dependent energy $1/2m\omega^2z^2$ with z the ion distance from centre. In such a case the motion of the ion can be quantized, which leads to resonant sidebands at detunings $\delta = \pm n\omega$ ($n \in \mathbb{N}$). For this thesis such a treatment is not necessary, since the used cooling transition has a linewidth $\Gamma/2\pi \gtrapprox 20\,\mathrm{MHz}$, while typical trap frequencies are on the order of $\omega/2\pi \approx 100\,\mathrm{kHz}$. Therefore the sidebands are not resolved and the motion can be treated classically. The ion can be described as scanning the velocity space and only being resonant during a certain time frame, in which it is cooled. This happens until the ion's velocity is not high enough to become resonant with the laser or the minimal temperature is reached. An illustration is shown in Fig. 2.3.

The Doppler limit for the transition of $^9\mathrm{Be}^+$ used in this thesis is $T_{\mathrm{D}} \approx 500\,\mu\mathrm{K}$ for $s_0 \to 0$. To achieve lower temperatures other cooling methods need to be employed, e.g. resolved sideband-cooling [32], where resolved sidebands ($\Gamma \ll \omega$) are used to remove quanta of motion from the quantized ion motion by driving transitions on the sidebands. Doppler cooling is regularly used as an initial step, since this technique requires temperatures close to the Doppler limit to be started. For a single $^9\mathrm{Be}^+$ ion resolved-sideband cooling has been done [35] using a Raman transition of the hyperfine structure of the ground state (see Fig. 4.1 for the term

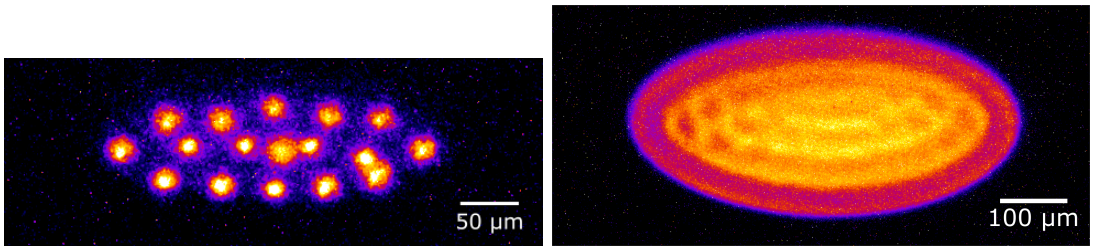

Figure 2.5: CCD images of Coulomb crystals made of $^9Be^+$ ions. **Left:** Small crystal consisting of about 20 ions. Individual ions are distinguishable from each other. **Right:** Large crystal consisting of about 400 ions. The typical shell structure is visible.

diagram), since this allows for a sufficiently narrow linewidth Γ.

2.3 Coulomb crystallization

If a cloud of trapped ions is cooled to a sufficiently low temperature, it forms an order structure called a Coulomb crystal, in which the ions are highly localized. In the following some properties of these ion formations in a Paul trap on the basis of [36] will be discussed.

The thermodynamics of three-dimensional Coulomb crystals can quantitatively be described by the plasma coupling parameter

$$\Sigma = \frac{Q^2}{4\pi\epsilon_0 a_{\mathrm{WS}} k_{\mathrm{B}} T}, \tag{2.30}$$

where a_{WS} is the Wigner-Seitz radius, which is related to the density n_0 through

$$\frac{1}{n_0} = \frac{4}{3}\pi a_{\mathrm{WS}}^3. \tag{2.31}$$

Σ can be understood as the ratio of potential energy, given by the Coulomb interaction of the ions in the plasma, and the kinetic energy, given by the plasma temperature. From numerical simulations it is known that for $\Sigma \gtrapprox 2$ a shell structure starts to form. It becomes fully pronounced for $\Sigma \approx 140$, though within the shells the ions are still best described by a liquid. Only for $\Sigma \gtrapprox 300$, the shells are fully crystallized and the whole object can be described as a solid. See Fig. 2.5 for experimental realizations of Coulomb crystals of $^9Be^+$ ions.

Technically, one could use Σ to estimate the temperature of the crystal, though it is imprecise, since it relies on optical comparisons and the boundaries between different regions are not clear-cut.

Experimentally, the ion density in the Paul trap can be determined from the

radial confinement characterized by the RF frequency Ω and its peak voltage V by using [37]

$$n_0 = \frac{\epsilon_0 V^2}{m\Omega^2 r_0^4}. \tag{2.32}$$

This is derived within the pseudopotential approximation at an plasma temperature of 0 K. Assuming that a given crystal can be described by a perfect spheroid, the number of ions N can be calculate through

$$N = \frac{4\pi}{3} R^2 L n_0, \tag{2.33}$$

where R is the radial and L is the axial extension of the crystal, which can be measured using a CCD image of the trapped ions, given that the magnification is known.
The ratio $\eta = R/L$ gives also access to the ratio of the axial to the radial trap frequency: [36]

$$\frac{\omega_z^2}{\omega_r^2} = \begin{cases} -2\dfrac{\sin^{-1}(1-\eta^2)^{1/2} - \eta(1-\eta^{-2})^{1/2}}{\sin^{-1}(1-\eta^2)^{1/2} - \eta^{-1}(1-\eta^{-2})^{1/2}} & \eta > 1 \\ \\ -2\dfrac{\sinh^{-1}(1-\eta^2)^{1/2} - \eta(1-\eta^{-2})^{1/2}}{\sinh^{-1}(1-\eta^2)^{1/2} - \eta^{-1}(1-\eta^{-2})^{1/2}} & \eta < 1. \end{cases} \tag{2.34}$$

During the work of this thesis only crystals with the prolate case ($L > R$) were used, as they exhibit less micromotion compared to crystals with $R > L$ (see Sec. 2.1). Eq. (2.34) is of particular interest, since ω_z can be determined from ion chains or through excitation (see Sec. 5.2). This is not as easily possible for ω_r, but Eq. (2.34) permits it to estimate ω_r from the geometry off a crystal determined through a CCD image.

2.3.1 Ion chains

The simplest configuration for N ions in a Paul trap is a 1-dimensional string along the trap axis, which can be achieved in a 3-dimensional trap for N ions if

$$\frac{\omega_r}{\omega_z} > 0.73 N^{0.86} \tag{2.35}$$

is satisfied [38]. An example for a chain of five ions is shown in Fig. 2.6. For the following discussion the ion chain is assumed to be made of only a single ion species and the approach given in [38] is followed.

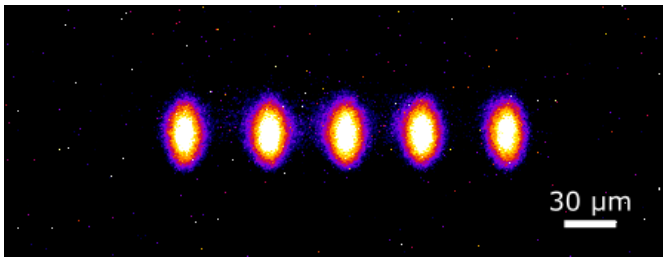

Figure 2.6: CCD image of an ion chain made of five $^9Be^+$ ions, with $\omega_r/2\pi \approx 164\,\text{kHz}$ and $\omega_z/2\pi \approx 40\,\text{kHz}$.

Equilibrium positions

The potential energy of an ion chain consisting of N particles of mass m and charge Q in a static harmonic potential with trap frequency ω_z is given by

$$V = \sum_{i=1}^{N} \frac{1}{2} m\omega_z^2 z_i(t)^2 + \sum_{\substack{i,j=1 \\ i\neq j}}^{N} \frac{Q^2}{8\pi\epsilon_0} \frac{1}{|z_i(t) - z_j(t)|}, \tag{2.36}$$

where $z_i(t)$ denotes the position of the i-th ion. Such a system can for example be given by ions inside a Paul trap, described by its pseudo-potential. For the following calculations the ions are assumed to be sufficiently cold so that the position can be described by

$$z_i(t) \approx z_{i,0} + q_i(t) \qquad i = 1, 2, ..., N, \tag{2.37}$$

where $z_{i,0}$ is the equilibrium position and $q_i(t)$ describes a small motion around it. Experimentally this is realized through laser cooling. The equilibrium position is defined by

$$\left.\frac{\partial V}{\partial z_i}\right|_{z_i = z_{i,0}} = 0, \tag{2.38}$$

which can be shown to result in the following relations for the positions $z_{i,0}$:

$$m\omega_z^2 z_{i,0} - \frac{Q^2}{4\pi\epsilon_0} \left(\sum_{j=1}^{i-1} \frac{1}{(z_{i,0} - z_{j,0})^2} - \sum_{j=i+1}^{N} \frac{1}{(z_{i,0} - z_{j,0})^2} \right) = 0. \tag{2.39}$$

These equations can be solved analytically in the case of $N = 2$ and $N = 3$ and

yield the solutions

$$N = 2: \quad z_{1,0} = -\sqrt[3]{\frac{Q^2}{16\pi\epsilon_0 m\omega_z^2}}, \quad z_{2,0} = \sqrt[3]{\frac{Q^2}{16\pi\epsilon_0 m\omega_z^2}}, \tag{2.40}$$

$$N = 3: \quad z_{1,0} = -\sqrt[3]{\frac{5Q^2}{16\pi\epsilon_0 m\omega_z^2}}, \quad z_{2,0} = 0, \quad z_{3,0} = \sqrt[3]{\frac{5Q^2}{16\pi\epsilon_0 m\omega_z^2}}. \tag{2.41}$$

For larger values of N, numerical calculations are required. The solutions for $N \leq 10$ are given in [38].

Eigenfrequencies

For the calculation of the eigenfrequencies, $q_i(t)$ is assumed to be small and a Taylor expansion of Eq. (2.36) up to second order is performed:

$$V \approx V(\vec{z}_0) + \frac{1}{2}\sum_{i,j=1}^{N} \frac{\partial^2 V}{\partial z_i \partial z_j}\bigg|_{\vec{z}_0} (z_i(t) - z_{i,0})(z_j(t) - z_{j,0}). \tag{2.42}$$

The Lagrangian as a function of the displacements $q_i(t)$ can then be written as

$$\mathcal{L} \approx \frac{m}{2}\sum_{i=1}^{N} \dot{q_i}^2 - \frac{1}{2}\sum_{i,j=1}^{N} \frac{\partial^2 V}{\partial z_i \partial z_j}\bigg|_{\vec{z}_0} q_i(t) q_j(t) \tag{2.43}$$

$$= \frac{m}{2}\left[\sum_{i=1}^{N} \dot{q}_i^2 - \sum_{i,j=1}^{N} A_{ij} q_i q_j\right], \tag{2.44}$$

where the matrix A_{ij} is explicitly given by

$$A_{ij} = \begin{cases} \dfrac{\partial^2 V}{\partial z_i^2}\Big|_{\vec{z}_0} = \omega_z^2 + \dfrac{Q^2}{2\pi\epsilon_0 m}\displaystyle\sum_{\substack{k=1 \\ k\neq i}}^{N} \frac{1}{|z_{i,0} - z_{k,0}|^3} & \text{for} \quad i = j \\ \dfrac{\partial^2 V}{\partial z_i \partial z_j}\Big|_{\vec{z}_0} = -\dfrac{Q^2}{2\pi\epsilon_0 m}\dfrac{1}{|z_{i,0} - z_{j,0}|^3} & \text{for} \quad i \neq j. \end{cases} \tag{2.45}$$

The Euler-Lagrange equations of this system are a set of N coupled differential equations

$$\ddot{q}_i + \sum_{k=1}^{N} A_{ik} q_k = 0. \tag{2.46}$$

The motion of the ion is expected to be oscillatory and therefore $\ddot{q}_i = -\omega_p^2 q_i$ can

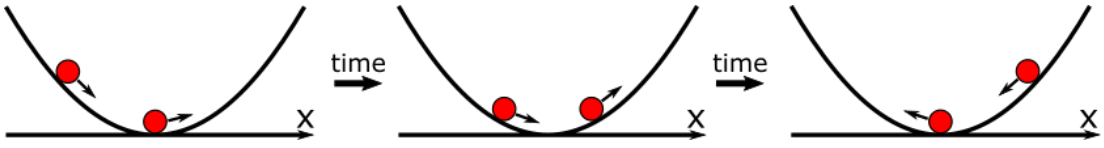

(a) COM mode

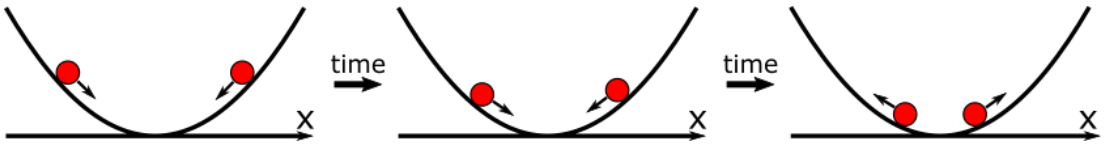

(b) Breathing mode

Figure 2.7: Illustration of the two lowest eigenfrequencies for two ions trapped in a harmonic potential. (a) COM mode, describing a collective motion of all ions in phase and with the same amplitude. (b) Breathing mode, describing a motion where the ions on each side of the trap centre move in phase and are out of phase by π with respect to the other side.

be used, where ω_p is an eigenfrequency of the system. This gives

$$\sum_{k=1}^{N} A_{ik} q_k = \omega_p^2 q_i, \tag{2.47}$$

i.e. the motion is described by the normalised eigenvectors $\vec{v}^p$ ($q_i \propto v_i^p$) and eigenvalues ω_p^2 of A_{ij}. Both the eigenvectors and the eigenfrequencies can be algebraically calculated for $N = 2$ and $N = 3$. Using the equilibrium positions given in Eq. (2.40) and (2.41), they can be expressed as

$$\begin{aligned} N = 2 : \vec{v}^1 &= \frac{1}{\sqrt{2}}(1,1), \quad \omega_1^2 = \omega_z^2, \qquad (2.48)\\ \vec{v}^2 &= \frac{1}{\sqrt{2}}(1,-1), \quad \omega_2^2 = 3\omega_z^2, \\ N = 3 : \vec{v}^1 &= \frac{1}{\sqrt{3}}(1,1,1), \quad \omega_1^2 = \omega_z^2, \qquad (2.49)\\ \vec{v}^2 &= \frac{1}{\sqrt{2}}(-1,0,1), \quad \omega_2^2 = 3\omega_z^2, \\ \vec{v}^3 &= \frac{1}{\sqrt{2}}(1,-2,1), \quad \omega_3^2 = \frac{29}{5}\omega_z^2. \end{aligned}$$

Higher numbers of N require numerical calculations and are given for $N \leq 10$ in [38].

The lowest eigenfrequency for a system of N ions corresponds to the trap frequency and is associated with the so called centre of mass mode (COM). It describes a movement, where all ions move in phase and the distance between the

ions does not change. The second eigenfrequency is the so called breathing mode and describes a movement where all ions on each side of the trap centre are in phase, but the sides have a relative phase difference of π. The amplitude of each ion's motion is proportional to the distance of its equilibrium position to the trap centre. An illustration of these modes is shown in Fig. 2.7.

2.4 The driven harmonic oscillator

The harmonic oscillator is an important physical model and can often be used as an approximate description for various systems. Here it will be discussed shortly based on [39], which gives a more detailed explanation.
The equation of motion for the driven harmonic oscillator for a particle of mass m is typically written in the form

$$\ddot{x} + 2\gamma\dot{x} + \omega_0^2 x = \frac{F(t)}{m}, \tag{2.50}$$

where γ describes a damping force and ω_0 is the eigenfrequency of the undamped system ($\gamma = 0$) without an external driving force F. Only the case of a periodic force $F(t)/m = K_0 \sin(\omega t)$ will be considered. This leads to the nonhomogeneous differential equation

$$\ddot{x} + 2\gamma\dot{x} + \omega_0^2 x = K_0 \sin(\omega t). \tag{2.51}$$

The general solution of such an equation is composed of a homogeneous part (free damped harmonic oscillator) and a particular part and can be written in the form

$$x(t) = A_1 e^{-\gamma t} \cos(\omega_1 t + \varphi_1) + A_2 \cos(\omega t + \varphi), \tag{2.52}$$

with $\omega_1 = \sqrt{\omega_0^2 - \gamma^2}$. From Eq. (2.52) it can be seen, that for $t \gg 1/\gamma$ the first term becomes negligible and only the second term

$$x(t) = A_2 \cos(\omega t + \varphi), \tag{2.53}$$

called the steady-state solution, is relevant. Inserting Eq. (2.53) into Eq. (2.51) yields

$$A_2(\omega) = \frac{K_0}{\sqrt{(\omega_0^2 - \omega^2)^2 + (2\gamma\omega)^2}} \tag{2.54}$$

and

$$\tan(\varphi) = -\frac{2\gamma\omega}{\omega_0^2 - \omega^2}. \tag{2.55}$$

Eq. (2.54) and (2.55) are plotted in Fig. 2.8. The frequency ω_{R} for which the

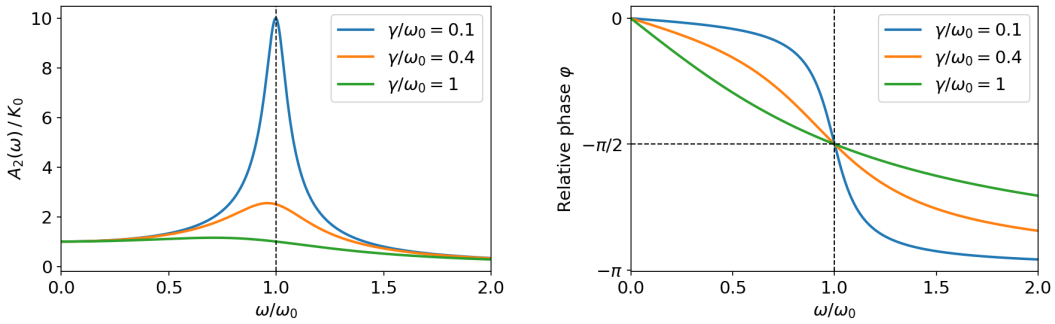

Figure 2.8: Left: Amplitude of the driven harmonic oscillator as a function of the relative driving frequency as given by Eq. (2.54). Note that the peak is not on the eigenfrequency of the free harmonic oscillator, but rather shifted to lower frequencies. **Right:** Phase of driven motion relative to driving force as a function of the relative driving frequency as described by Eq. (2.55).

oscillation amplitude is maximal is found to be

$$\omega_{\mathrm{R}} = \sqrt{\omega_0^2 - 2\gamma^2}. \tag{2.56}$$

This is real for $\gamma/\omega_0 < 1/\sqrt{2}$ and resonance occurs then below the eigenfrequency of the undamped system ($\gamma = 0$). For $\gamma/\omega_0 \geq 1/\sqrt{2}$, the system is overdamped and the amplitude has no maximum. The relative phase φ between driving field and oscillatory motion on the other hand is always $\varphi = -\pi/2$, when $\omega = \omega_0$. However, the shape and curvature of $\varphi(\omega)$ are dependent on γ/ω_0.

2.5 Nonlinear optics

Nonlinear optics describes a nonlinearity in the response of a medium to a electric field $\vec{E}$ associated with a light field. This in general leads to many different effects. Here second harmonic generation and three wave mixing will be discussed, which are used in the optical setups at CryPTEx. For a more detailed discussion see [40] which this section is based on.

From Maxwell's equations it is known that light can be described as an electromagnetic wave. Therefore, light is associated with an electric field $\vec{E}$ which interacts with matter and leads there to a polarization $\vec{P}$. In the following only a homogeneous, isotropic medium will be discussed. The isotropy guarantees that the vectors $\vec{E}$ and $\vec{P}$ are parallel and therefore each component can be examined individually, i.e. vector notation is not necessary. The relationship between them

can then often be expressed as a linear response

$$P = \epsilon_0 \chi E, \tag{2.57}$$

where ϵ_0 is the vacuum permittivity and χ is the medium-dependent electric susceptibility. In many cases though, the response is nonlinear.
The polarization, in general, is a function of the electric field $P(E)$. The external electric field E from a light field is usually small compared to electric fields present inside matter and P can be expanded in a Taylor series

$$P = \epsilon_0(\chi^{(1)}E + \chi^{(2)}E^2 + \chi^{(3)}E^3 + ...), \tag{2.58}$$

which to first order approximation becomes Eq. (2.57). Only the linear and the quadratic term will be taken into account, where the latter one is relevant for the nonlinear effects discussed here:

$$P_{\mathrm{NL}} = \epsilon_0 \chi^{(2)} E^2. \tag{2.59}$$

The wave equation for the propagation of an electromagnetic wave inside a medium, in which a nonlinear response to second order is relevant, is given by

$$\nabla^2 E - \frac{1}{c^2}\frac{\partial^2 E}{\partial t^2} = -\mathcal{S}, \tag{2.60}$$

$$\mathcal{S} = -\mu_0 \frac{\partial^2 P_{\mathrm{NL}}}{\partial t^2}, \tag{2.61}$$

with c the speed of light and μ_0 the vacuum permeability. $\mathcal{S}$ can be seen as a source term for radiation. An incoming light field E_0 generates a source $\mathcal{S}(E_0)$, which produces a field E_1. This again would generate a source $\mathcal{S}(E_1)$ etc., leading to an iterative solution. To simplify this, the nonlinearity is assumed to be sufficiently small so that only the initial wave acts as a source and produces a corresponding field. Any higher orders are neglected. This approach is called the first Born approximation. For the further discussion it is taken to be valid.

2.5.1 Second harmonic generation

The simplest case to consider is that of a monochromatic light field with an angular frequency ω described by

$$E(t) = E_0 \cos(\omega t), \tag{2.62}$$

which interacts with a nonlinear medium. Inserting this into Eq. (2.59) gives

$$P_{\mathrm{NL}} = \epsilon_0 \chi^{(2)} E_0^2 \cos^2(\omega t) \tag{2.63}$$

$$= \epsilon_0 \chi^{(2)} E_0^2 \frac{1}{2}(1 + \cos(2\omega t)) \tag{2.64}$$

$$= \frac{1}{2}\epsilon_0 \chi^{(2)} E_0^2 + \frac{1}{2}\epsilon_0 \chi^{(2)} E_0^2 \cos(2\omega t). \tag{2.65}$$

The nonlinear term leads to a constant polarization and a dynamical polarization with twice the frequency of the incoming fundamental wave. Together with Eq. (2.61) this gives the source term

$$\mathcal{S} \propto E_0^2 \cos(2\omega t), \tag{2.66}$$

i.e. the medium radiates a wave at twice the incoming frequency. The amplitude of this field is proportional to $\mathcal{S}$ and its intensity is then

$$I_{2\omega} \propto |\mathcal{S}|^2 \propto |E_0^2|^2 = I_0^2. \tag{2.67}$$

Therefore, the intensity of the so called second harmonic scales with the square of the intensity I_0 of the incoming harmonic wave. Furthermore, for this process to happen phase matching needs to be employed, which is discussed at the end of the next section.

2.5.2 Three-wave mixing

Next, the case of two monochromatic incoming waves with angular frequencies ω_1 and ω_2 will be examined:

$$E = E_1 \cos(\omega_1 t) + E_2 \cos(\omega_2 t). \tag{2.68}$$

The nonlinear polarization of the medium is then given by

$$P_{\mathrm{NL}} = \epsilon_0 \chi^{(2)} \left[E_1^2 \cos(\omega_1 t)^2 + E_2^2 \cos(\omega_2 t)^2 + 2E_1 E_2 \cos(\omega_1 t)\cos(\omega_2 t)\right] \tag{2.69}$$

$$\begin{aligned} = &\frac{\epsilon_0 \chi^{(2)}}{2}[E_1^2 + E_2^2 + E_1^2 \cos(2\omega_1 t) + E_2^2 \cos(2\omega_2 t) \\ &+ 2E_1 E_2 \cos\left((\omega_1 + \omega_2)t\right) + 2E_1 E_2 \cos\left((\omega_1 - \omega_2)t\right)]. \end{aligned} \tag{2.70}$$

The corresponding source term can be separated as

$$\mathcal{S} = \mathcal{S}_{2\omega_1} + \mathcal{S}_{2\omega_2} + \mathcal{S}_{\omega_1+\omega_2} + \mathcal{S}_{\omega_1-\omega_2} \tag{2.71}$$

with

$$\mathcal{S}_{2\omega_1} \propto E_1^2 \cos(2\omega_1 t), \tag{2.72}$$

$$\mathcal{S}_{2\omega_2} \propto E_2^2 \cos(2\omega_2 t), \tag{2.73}$$

$$\mathcal{S}_{\omega_1+\omega_2} \propto E_1 E_2 \cos\left((\omega_1+\omega_2)t\right), \tag{2.74}$$

$$\mathcal{S}_{\omega_1-\omega_2} \propto E_1 E_2 \cos\left((\omega_1-\omega_2)t\right). \tag{2.75}$$

The first two terms correspond to the second harmonic generation of each individual wave. The third term describes a produced wave with the frequency $\omega_1 + \omega_2$ and which is commonly called sum frequency generation. The fourth term represents a generated wave at the frequency $\omega_1 - \omega_2$ and is correspondingly called difference frequency generation.
For these processes to happen further restrictions need to be employed. These can be understood when considering light as photons. In this case the processes are the interaction of two photons at energy $\hbar\omega_\mathrm{a}$ and $\hbar\omega_\mathrm{b}$ to generate a photon with energy $\hbar\omega_\mathrm{c}$, mediated by the medium. Alternatively one photon with energy $\hbar\omega_\mathrm{c}$ can generate two photons at the energies $\hbar\omega_\mathrm{a}$ and $\hbar\omega_\mathrm{b}$. Employing energy and momentum conservation gives

$$\hbar\omega_\mathrm{a} + \hbar\omega_\mathrm{b} = \hbar\omega_\mathrm{c}, \tag{2.76}$$

$$\hbar\vec{k}_\mathrm{a} + \hbar\vec{k}_\mathrm{b} = \hbar\vec{k}_\mathrm{c}. \tag{2.77}$$

Eq. (2.77) is usually called the phase matching condition (in wave optics, the wavevector $\vec{k}$ is related to the phase) and represents the major constraint for nonlinear processes. If collinear waves in a dispersive medium with refractive index n are considered, the wavevector can be written as $|\vec{k}| = n\omega/c$. Then Eq. (2.77) becomes

$$n_\mathrm{a}\omega_\mathrm{a} + n_\mathrm{b}\omega_\mathrm{b} = n_\mathrm{c}\omega_\mathrm{c}. \tag{2.78}$$

The refractive index of real materials is frequency dependent and Eq. (2.76) and (2.78) are usually not simultaneously satisfied. Often the polarization and angle dependence of birefringent materials is used to overcome this and allow for three-wave mixing. If a suitable material is found, the problem is reduced to precise alignment of the medium to satisfy Eq. (2.78).
At CryPTEx, these processes are used to generate lasers for photoionization of ^{9}Be atoms and laser cooling of $^9Be^+$ ions. The photoionization laser at 235 nm is produced from a 940 nm diode laser, which is twice frequency doubled by second harmonic generation. The nonlinear medium is provided by a periodically poled potassium titanyl phosphate (PPKTP) crystal for the first doubling stage and by

a beta barium borat (BBO) crystal for the second stage. The cooling laser has a wavelength of 313 nm and is produced from two lasers at 1050 nm and 1550 nm. These are used for sum frequency generation using a periodically poled lithium niobate crystal (PPLN), generating light at 626 nm. This is frequency doubled to 313 nm using a BBO crystal.

2.6 Optical resonators

An optical resonator is a system used to confine and store light. The setup usually consists of multiple mirrors and supports only light with a specific wavelength. At CryPTEx, optical resonators are used as a way to generate high intensities, increasing the efficiency of second harmonic generation, which scales quadratic with the intensity of the incoming harmonic wave (see Eq. (2.67)). In this section the Fabry-Pérot resonator will be reviewed as an example for an optical resonator. Then two techniques will be described, which can be used to lock the resonance frequency of a cavity to the frequency of an incoming laser.

2.6.1 The Fabry-Pérot resonator

The simplest setup for an optical resonator is a Fabry-Pérot resonator consisting of two plane mirrors opposite to each other, between which light is reflected multiple times (see Fig. 2.9). This setup will shortly be discussed here as an example. For a more detailed discussion see [40], where this section is adapted from.
For the following discussion the mirrors are taken to be parallel, flat, and highly reflective with a distance d separating them. First a system will be discussed, where the amplitude of the light field after a round trip is the same as the initial wave, i.e. ideal mirrors and no losses due to scattering or absorption inside the resonator. This system can be described by a travelling wave between the two cavity mirrors. A wave that reproduces itself after one round trip is called a mode of the resonator. For a mode, the acquired phase φ needs to be a multiple of 2π:

$$\varphi = 2d|\vec{k}| = \frac{4\pi\nu d}{c} = 2\pi n, \qquad n \in \mathbb{N} \tag{2.79}$$

$$\iff \frac{2\nu d}{c} = n, \tag{2.80}$$

where ν is the frequency of the incoming light field and c the speed of light.
This definition of a mode can be understood, if a wave continuously transmitted through the incoupling mirror entering the resonator is considered. If the

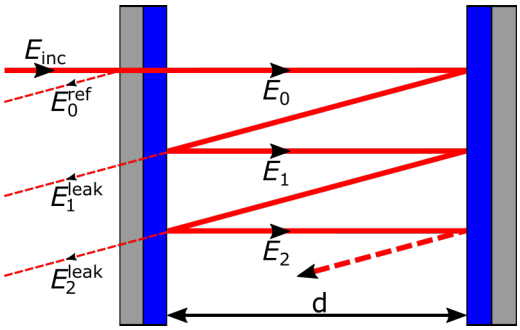

Figure 2.9: Schematic of a Fabry-Pérot resonator. The beams are all overlapping, but are shown separated for clarity. An incoming laser beam E_{inc} is entering through the first mirror into the resonator. Inside, the initial wave E_0 superimposes with the reflected wave E_i after i round trips. At each round trip the light field gains an additional phase and the amplitude is reduced due to losses of the cavity. After i round trips a part of the light field E_i^{leak} is leaked through the incoupling mirror. Additionally, parts of the incoming beam E_{inc} are reflected as E_0^{ref} at the incoupling mirror and overlap with the leakage fields E_i^{leak}.

frequency of the incoming wave matches one mode of the cavity, it will interfere constructively with itself. In any other case the wave will interfere destructively. From Eq. (2.80) it follows that only discrete frequencies can be stored in a resonator. The modes of the resonator are separated by a spacing of

$$\nu_{\text{F}} = \frac{c}{2d}, \tag{2.81}$$

called the free spectral range.

So far only a lossless system was considered for which every wave, regardless of the number of reflections, has the same amplitude. Therefore any phase mismatch leads to complete destructive interference. In a real system this is not the case. There a phase mismatch and loses inside the cavity have to be taken into account. The initial wave E_0 can be described after one round trip by

$$E_1 = hE_0 \tag{2.82}$$

with

$$h = re^{i\delta}, \tag{2.83}$$

where $r < 1 \in \mathbb{R}$ takes into account any losses (e.g. absorption, finite reflectivity of the mirrors) and δ is the phase mismatch with respect to the incoming wave. The after i round trips it can be written as

$$E_i = h^i E_0. \tag{2.84}$$

The wave inside the resonator is the superposition of all components

$$E = E_0 + E_1 + E_2 + ... = \sum_{i=0}^{\infty} h^i E_0 = \frac{E_0}{1-h}. \tag{2.85}$$

In an experiment only the intensity I can be measured. Using Eq. (2.79) it can be shown that

$$I = |E|^2 = \frac{I_{\max}}{1 + (2\mathcal{F}/\pi)^2 \sin^2(\pi\nu/\nu_F)}, \tag{2.86}$$

with

$$I_{\max} = \frac{|E_0|^2}{(1-r)^2}, \tag{2.87}$$

$$\mathcal{F} = \frac{\pi\sqrt{r}}{1-r}, \tag{2.88}$$

where $\mathcal{F}$ is called the finesse of the cavity. Therefore, in a real system the modes have a Lorentzian shape with a finite width in frequency space.
To gain information about the cavity, the reflected beam from the incoupling mirror will be used later on. This is done because the reflected beam does not only contain information about the light inside the cavity through leakage, but also provides information from the incoming beam due to the initial reflection (see Fig. 2.9). To calculate this, it is assumed that all the losses in the cavity are caused by the finite reflectivity of the mirrors, i.e. $h = r_1 r_2 e^{i\delta}$, with $r_1, r_2 < 1$ being the reflectivity of the first and second mirror respectively. Also the transmission t_1 of the first mirror is introduced. The reflected beam consists of the initial reflection

$$E_0^{\text{ref}} = r_1 E^{\text{inc}} \tag{2.89}$$

of the incoming beam E^{inc} and the leakage

$$E_i^{\text{leak}} = \frac{t_1}{r_1} E_i = \frac{t_1^2}{r_1} h^i E^{\text{inc}} \qquad (i > 1), \tag{2.90}$$

where the beam after i-round trips is partially transmitted through the incoupling mirror. The total sum is given by

$$E^{\text{ref}} = E_0^{\text{ref}} + \sum_{i=1}^{\infty} E_i^{\text{leak}} \tag{2.91}$$

$$= E^{\text{inc}} \left(r_1 - \frac{t_1^2}{r_1} \frac{r e^{i\delta}}{1 - r e^{i\delta}} \right), \tag{2.92}$$

where $r = r_1 r_2$ was introduced.

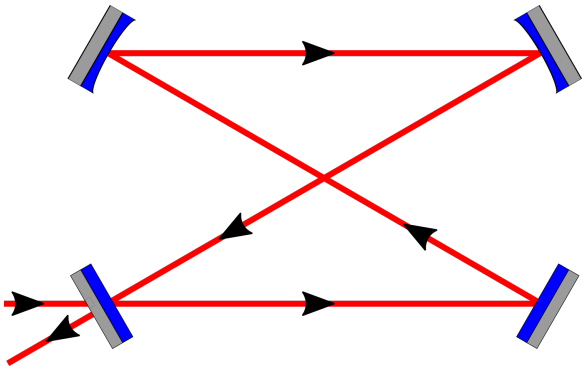

Figure 2.10: Schematic of a bow tie cavity. Two planar (bottom) and two spherical (top) mirrors are used in the shown arrangement. This generates a focus in the centre of each short arm. The reflection of the incoming beam can be accessed easily. The disadvantage of this setup is occurring astigmatism.

The discussion was limited to the Fabry-Pérot resonator. Other setup are also possible. For these the same concepts apply, i.e. only certain modes with a Lorentzian shape are supported, but they might have some other advantages and disadvantages. At CryPTEx, bow-tie resonators (see. Fig. 2.10) are used, which allow for easy access to the reflected beam, since the incoupling mirror is not perpendicular to the incoming light. Additionally, it provides two foci, one at centre of each short arm. The disadvantage of a bow tie cavity is the emerging astigmatism.

2.6.2 Frequency stabilization

As previously mentioned, optical resonators are used at CryPTEx to increase the efficiency of second harmonic generation. The length of these cavities has to be adjusted to support the needed mode (see Eq. (2.80)), since the frequency of the incoming light is fixed. Constant corrections are required due to air fluctuations, vibrations, and frequency changes of the laser. This is commonly achieved by mounting one of the resonator mirrors onto a piezo element, which is controlled by a PID (proportional–integral–derivative) controller. In this section two techniques will be described to generate a suitable error signal to lock the cavity to a single mode.

2.6.2.1 Hänsch-Couillaud method

The Hänsch-Couillaud method was first proposed by T.W. Hänsch and B. Couillaud in [41]. It uses the reflection from the incoupling mirror to lock the resonator.

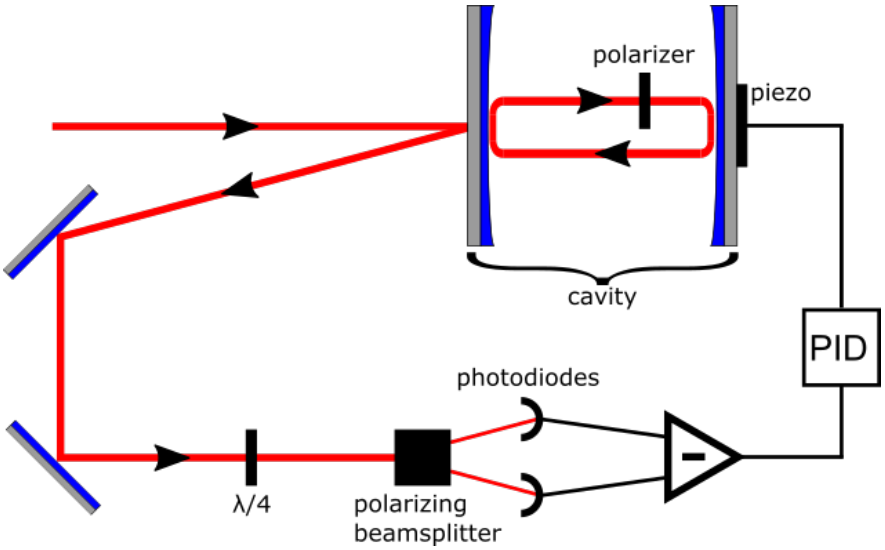

Figure 2.11: Setup of the Hänsch-Couillaud method. An incoming, linear polarized beam is sent into a cavity with a polarizer inside. The reflected beam contains information about the phase inside the cavity, encoded in its polarization. Analysing it generates a error signal which can be used to adjust the cavity length. Explanations are given in the text.

For this the polarization is analysed. The method will be discussed shortly, following [41].
A monochromatic linearly polarized laser beam is send into a resonator (see Fig. 2.11), so that the reflection of the incoupling mirror can be detected. Inside the cavity a linear polarizer is placed with an angle θ relative to the polarization axis of the incoming axis. In the plane wave approximation, the incoming wave can be decomposed into a parallel and perpendicular part:

$$E_{\parallel}^{\text{inc}} = E^{\text{inc}} \cos\theta, \tag{2.93}$$

$$E_{\perp}^{\text{inc}} = E^{\text{inc}} \sin\theta. \tag{2.94}$$

For the parallel component, the reflected wave is then (see Eq. (2.92))

$$\begin{aligned} E_{\parallel}^{\text{ref}} &= E_{\parallel}^{\text{inc}} \left(r_1 - \frac{t_1^2}{r_1} \frac{r e^{i\delta}}{1 - r e^{i\delta}} \right) \\ &= E_{\parallel}^{\text{inc}} \left(r_1 - \frac{t_1^2 r}{r_1} \frac{\cos(\delta) - r + i \sin(\delta)}{(1-r)^2 + 4r \sin^2(\frac{\delta}{2})} \right), \end{aligned} \tag{2.95}$$

where δ represents again the phase mismatch after one round trip with respect

to the initial wave. The reflected perpendicular component is simply

$$E_{\perp}^{\mathrm{ref}} = E_{\perp}^{\mathrm{inc}} r_1. \tag{2.96}$$

From this it can be seen, that only in the resonant case ($\delta = 2\pi n$) both parts $E_{\perp}^{\mathrm{ref}}$ and $E_{\parallel}^{\mathrm{ref}}$ are real and they remain in phase, i.e. the reflected beam will be linearly polarized. Off resonance, $E_{\parallel}^{\mathrm{ref}}$ acquires an imaginary component which leads to an elliptical polarization of the total reflected beam, where the handedness depends on the sign of the detuning.
To analyse the polarization of the reflected beam, it is sent through a $\lambda/4$ waveplate and a polarizing beam splitter as shown in Fig. 2.11. The fast axis of the $\lambda/4$ waveplate is rotated by 45° relative to one of the two outputs of the beam splitter. The intensities I_{a} and I_{b} of the two outputs are measured using photodiodes and $I_{\mathrm{a}} - I_{\mathrm{b}}$ is retrieved from a differential amplifier.
To understand this setup, it is the easiest to think of the elliptically polarized light as consisting of two counterrotating circularly polarized components of different amplitude. Then the $\lambda/4$ waveplate will transform them into two orthogonal linearly polarized components. The beam splitter separates them. For incoming linearly polarized light the two components are equal in magnitude and therefore $I_{\mathrm{a}} - I_{\mathrm{b}} = 0$, while for elliptically polarized light $I_{\mathrm{a}} - I_{\mathrm{b}} \neq 0$, where the sign depends on the handedness. The exact signal as a function of the phase mismatch δ can be calculated to be

$$I_{\mathrm{a}} - I_{\mathrm{b}} = I^{\mathrm{inc}} 2\cos(\theta)\sin(\theta)\frac{t_1^2 r \sin(\delta)}{(1-r)^2 4r\sin^2(\delta/2)}, \tag{2.97}$$

where $I^{\mathrm{inc}} = \frac{1}{2}c\epsilon|E^{\mathrm{inc}}|^2$ is the incoming intensity. Eq. (2.97) is plotted in Fig. 2.12 alongside the Lorentzian shaped intensity inside the cavity (see Eq. (2.86)), which shows that $I_{\mathrm{a}} - I_{\mathrm{b}}$ has a steep zero-crossing at maximum intensity. Therefore, it can be used as an error signal to frequency-lock a cavity. At CryPTEx, this technique is used to lock a cavity for second harmonic generation, which is part of the cooling laser setup for Doppler cooling of $^9Be^+$ ions (see Sec. 4.3).

2.6.2.2 Pound-Drever-Hall method

The Pound-Drever-Hall (PDH) method was first introduced in [42] by R.V. Pound, R. Drever, and J.L. Hall. It requires sidebands in frequency space of

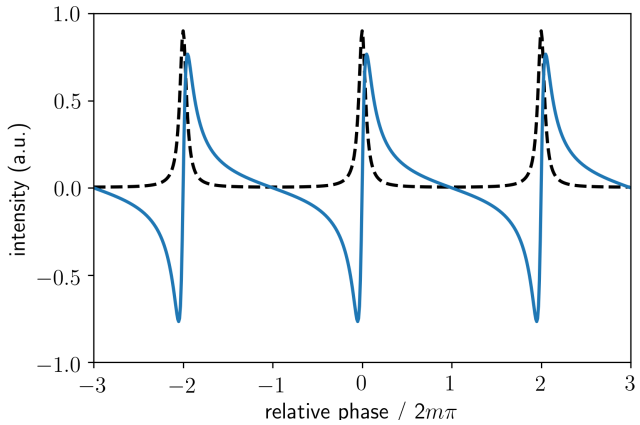

Figure 2.12: Error signal (light blue) generated by the Hänsch-Couillaud method and intensity inside the cavity (dashed black) as a function of the relative phase shift per round trip.

the incoming beam, which can be produced through phase modulation. The reflected beam contains information about the phase mismatch encoded in the interference of the carrier frequency and the sidebands. To extract this, the measured signal is mixed with an oscillator signal and a low pass filter is used. The following discussion is based on [43]. The general setup is shown in Fig. 2.13.

The incoming monochromatic laser beam is phase modulated with a frequency Ω_s, e.g. using a Pockels cell. The resulting beam can be described by

$$E^{\text{inc}} = E_0 e^{i(\omega t + \beta \sin(\Omega_s t))}. \tag{2.98}$$

Assuming that the modulation depth $\beta \ll 1$, Eq. (2.98) can be expanded using Bessel functions up to first order

$$E^{\text{inc}} \approx E_0 \left(J_0(\beta) e^{i\omega t} + J_1(\beta) e^{i(\omega+\Omega_s)t} - J_1(\beta) e^{i(\omega-\Omega_s)t} \right), \tag{2.99}$$

i.e. the phase modulation is equivalent to a frequency modulation, generating two sidebands at $\pm\Omega_s$. For the further discussion the mirrors of the cavity are assumed to have the same reflectivity r and the reflection coefficient of a monochromatic beam based on Eq. (2.92) is defined:

$$F(\omega) = \frac{E^{\text{ref}}}{E^{\text{inc}}} = \frac{r(1 - e^{i\omega/\nu_F})}{1 - r^2 e^{i\omega/\nu_F}}, \tag{2.100}$$

with the detuning per round trip written in terms of the free spectral range ν_F

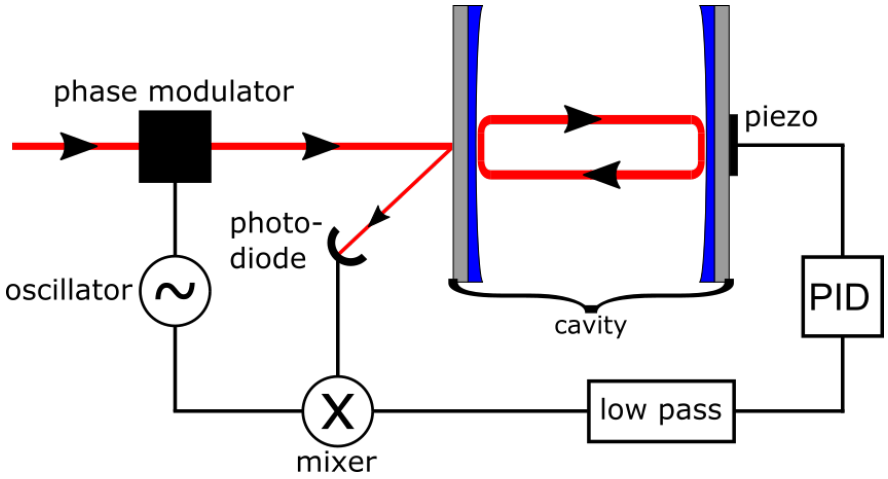

Figure 2.13: Setup of the PDH method. The incoming beam is phase modulated to generate sidebands in frequency space. The reflected beam can then be analysed to gain an error signal to lock the cavity to the laser frequency. Explanations are given in the text.

(see Eq. (2.81)). The total reflected beam of the modulated laser is

$$E^{\text{ref}} = E_0 \left(F(\omega) J_0(\beta) e^{i\omega t} + F(\omega+\Omega_\text{s}) J_1(\beta) e^{i(\omega+\Omega_\text{s})t} - F(\omega-\Omega_\text{s}) J_1(\beta) e^{i(\omega-\Omega_\text{s})t} \right). \tag{2.101}$$

Only the power $P^{\text{ref}} \propto |E^{\text{ref}}|^2$ can be measured and it is calculated to be

$$\begin{aligned} P^{\text{ref}} =& P_\text{c} |F(\omega)|^2 + P_\text{s} (|F(\omega+\Omega_\text{s})|^2 + |F(\omega-\Omega_\text{s})|^2) \\ &+ 2\sqrt{P_\text{c} P_\text{s}} \Big\{ \text{Re}\left[F(\omega)F^*(\omega+\Omega_\text{s}) - F(\omega)F^*(\omega-\Omega_\text{s})\right] \cos\Omega_\text{s} t \\ &\qquad \text{Im}\left[F(\omega)F^*(\omega+\Omega_\text{s}) - F(\omega)F^*(\omega-\Omega_\text{s})\right] \sin\Omega_\text{s} t \Big\} \\ &+ (2\Omega_\text{s} \text{ terms}), \end{aligned} \tag{2.102}$$

where $P_\text{c} \propto J_0^2(\beta)|E_0|^2$ and $P_\text{s} \propto J_1^2(\beta)|E_0|^2$ are the power of the carrier and sidebands respectively. This shows that a base signal with frequency ω is generated which is modulated with Ω_s due to interference of the carrier and the sidebands. The $2\Omega_\text{s}$ terms are from interference of the sidebands and are not relevant. The interesting parts are the $\cos(\Omega_\text{s} t)$ and $\sin(\Omega_\text{s} t)$ terms, since they give access to the carrier phase. As it turns out, $F(\omega)F^*(\omega+\Omega_\text{s}) - F(\omega)F^*(\omega-\Omega_\text{s})$ is either mostly real if $\Omega_\text{s} \ll \nu_\text{F}/\mathcal{F}$ or mostly imaginary if $\Omega_\text{s} \gg \nu_\text{F}/\mathcal{F}$, where $\mathcal{F}$ denotes the finesse of the cavity defined in Eq. (2.88). In either of those cases the signal can be extracted with a mixer and a low pass filter.
For example, if the cosine term needs to be extracted, the signal is mixed with

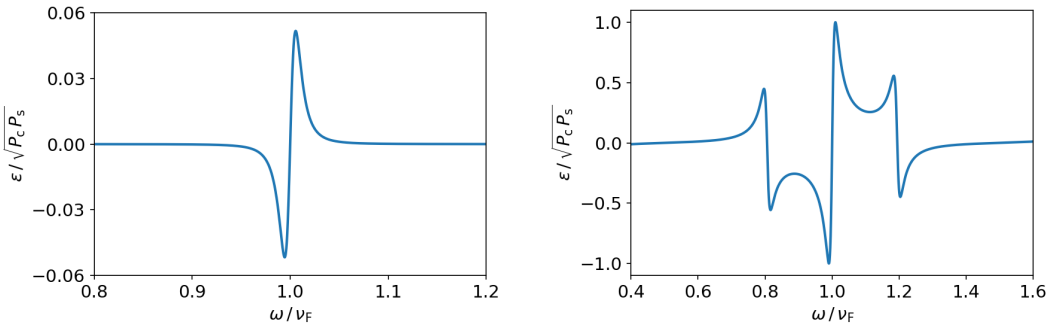

(a) Slow modulation $\Omega_s = 0.5\frac{\nu_F}{\mathcal{F}}$ **(b)** Fast modulation $\Omega_s = 20\frac{\nu_F}{\mathcal{F}}$

Figure 2.14: Error signal of the PDH method for the cases of slow and fast modulation. In either case a steep zero-crossing is observed on resonance and the signal can be used to lock a cavity.

$\cos(\Omega_s t)$ and since

$$\cos^2(\Omega_s t) = \frac{1}{2}(1 + \cos(\Omega_s t)), \tag{2.103}$$
$$\cos(\Omega_s t)\sin(\Omega_s t) = \frac{1}{2}\sin(2\Omega_s t)$$

a DC component from the cosine term is produced, but not from the sine term. This is obtained using a low pass filter. The same applies to the sine term when mixed with $\sin(\Omega_s t)$.
In the case of a slow modulation $\Omega_s \ll \nu_F/\mathcal{F}$ the relevant term can be written as

$$F(\omega)F^*(\omega+\Omega_s) - F(\omega)F^*(\omega-\Omega_s) \approx 2\,\mathrm{Re}\left[F(\omega)\frac{\mathrm{d}}{\mathrm{d}\omega}F^*(\omega)\right]\Omega_s \tag{2.104}$$
$$\approx \frac{\mathrm{d}|F|^2}{\mathrm{d}\omega}\Omega_s.$$

This means that the imaginary part in Eq. (2.102) can be neglected. Mixing the signal from Eq. (2.104) with $\cos(\Omega_s t)$, the output of the low pass filter is given by

$$\epsilon \approx \sqrt{P_c P_s}\frac{\mathrm{d}|F|^2}{\mathrm{d}\omega}\Omega_s, \tag{2.105}$$

which is shown in Fig. 2.14a.
For a fast modulation $\Omega_s \gg \nu_F/\mathcal{F}$ and close to the resonance of the carrier frequency, total reflection of the sidebands can be assumed: $F(\omega \pm \Omega_s) \approx 1$. Then

$$F(\omega)F^*(\omega+\Omega_s) - F(\omega)^*F(\omega-\Omega_s) \approx -2i\,\mathrm{Im}\left[F(\omega)\right]. \tag{2.106}$$

Therefore, the real part in Eq. (2.102) can be neglected. Mixing with $\sin(\Omega_s t)$ and using a low pass filter gives the error signal

$$\epsilon = -\sqrt{P_c P_s}\mathrm{Im}\left[F(\omega)F^*(\omega+\Omega_s) - F(\omega)F^*(\omega-\Omega_s)\right], \tag{2.107}$$

which is shown in Fig. 2.14b.
In both cases a steep zero-crossing on resonance is observed. Therefore, these signals can be used for a PID controller to lock a cavity. The PDH method is used at CryPTEx to lock two cavities for second harmonic generation to produce a photoionization laser for ^{9}Be atoms (see Sec. 4.2). It is useful in this case, since for slow modulation, the sidebands can lie within the linewidth of the cavity and are therefore preserved. They can then be used to lock a second cavity. This makes it possible to lock two cavities, while only modulating the initial beam once.

Chapter 3

The cryogenic Paul trap

In this chapter the cryogenic Paul trap used for the measurements of this thesis is described. It was specifically designed in [44] for storage of HCI. The lifetime of HCI inside a Paul trap is mostly limited by collisions with residual gas inside the vacuum chamber. In particular, charge exchange is a dominant loss mechanism, besides electrodynamic losses due to the high charge states To still be able to achieve long time storage of HCI a pressure $\ll 10^{-10}$ mbar is needed. At the cryogenic Paul trap experiment (CryPTEx) [17], this is achieved by cooling down the trap to cryogenic temperatures (4 K) where all gases besides H_2 and He condensate. Additionally, optical ports are required to give access for lasers and ion sources to enter and for imaging of the trap centre. In the follwing section the cryogenic Paul trap, its electronics and the optical setup at the trap are described.

3.1 The cryogenic system

Only a brief description of the cryogenic Paul trap is given here based on [44], which should be referred to for a more detailed description. A model of the cryogenic system and the trap electrodes is shown in Fig. 3.1.
The cooling power to get to cryogenic temperatures is provided by a pulse tube cryocooler with two temperature stages. It has a cooling power of 31 W at 40 K and 1 W at 4 K. The Paul trap can not directly be cooled down to 4 K, since blackbody radiation from 300 K provides to much heating to achieve it. Therefore, two nested temperature stages are used. The vacuum chamber on the outside is at 300 K and encloses the first heat shield at 40 K. Inside the 40 K shield the 4 K stage is nested on which the Paul trap is installed and thermalised to 4 K. The 40 K stage prevents blackbody radiation from 300 K from reaching the 4 K stage with the exception of optical ports. At cryogenic temperatures most gases condense on the heat shield surfaces and the remaining H_2 partial pressure was

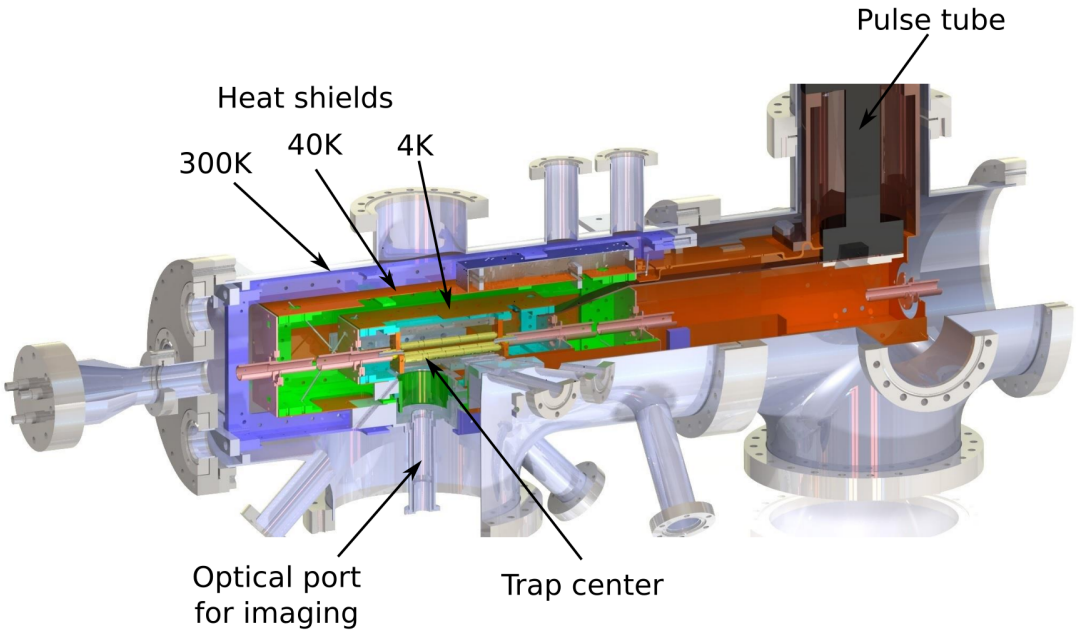

Figure 3.1: CAD (computer-aided design) rendering of the Paul trap and the cryogenic system of CryPTEX. The vacuum chamber at 300 K encloses the 40 K and the 4 K heat shield. Inside the 4 K environment the trap is mounted and thermalised to 4 K. Cooling is provided by a pulse tube cryocooler. The optical port below the trap is used for imaging of the trapped ions onto a CCD camera and a photomultiplier tube (PMT). The optical setup is described in Sec. 3.3. Adapted from [17].

estimated to be $\approx 6 \times 10^{-14}$ mbar at the trap centre [20].

The Paul trap is schematically shown in Fig. 3.2. It consists of four rod electrodes with six individual segments each, giving overall 24 electrodes. For trapping of $^9Be^+$ only the first three electrodes from the left on each rod in Fig. 3.2 are required. The other 12 electrodes can be used to produce a second trapping region as a reservoir or as a quadrupole guide for HCI [20], but were not used for the measurements presented in this thesis.

The larger end-cap electrodes shown in Fig. 3.2 have a length of $2z_{\mathrm{EC}} = 20$ mm and are used for axial confinement in the trap centre, which is in the centre of the middle electrodes with a length of $2z_0 = 5.4$ mm. z_0 was chosen in such a way to produce a highly harmonic potential in axial direction. The geometric factor in Eq. (2.4) was numerically determined to be $\kappa = 0.259$. The trap diagonal has a length of $2r_0 = 7$ mm and the diameter of the rods is $2r_{\mathrm{e}} = 8$ mm.

The electrodes are made of OFHC copper (oxygen-free high thermal conductivity), which are additionally gold-plated to avoid oxidation. All 24 electrodes are individually connected to a gold-plated copper wire and can be supplied with DC and RF voltages. The production of these voltages is described in the following

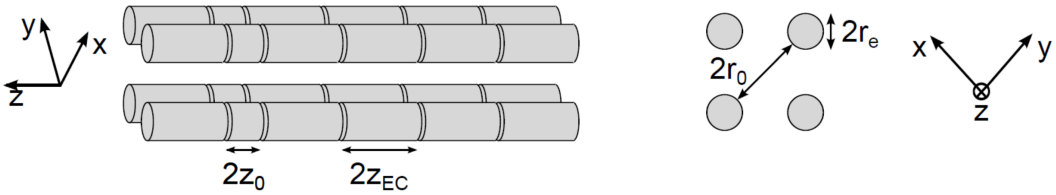

Figure 3.2: Schematic side view (left) and front view (right) of the Paul trap electrodes consisting of four rods with six segmented electrodes each. For trapping of $^9Be^+$ ions only the first three electrodes from the left are used on each rod. The end-cap electrodes have a length of $2z_{EC} = 20\,mm$. The shorter middle electrodes have a length of $2z_0 = 5.4\,mm$. The trap diagonal has a length of $2r_0 = 7\,mm$ and each electrodes has a diameter of $2r_e = 8\,mm$. Adapted from [29].

section.

3.2 Electronics

The electronics of the Paul trap consist of two parts: the DC voltages for axial trapping and the RF voltages for radial trapping, which are produced independently and are then coupled. A scheme is shown in Fig. 3.3. A detailed description can be found in [29]. Here only a short summary is given.
For the DC voltages a single power supply is used for all 24 electrodes, such that the intrinsic noise and ripple of the power supply affects all electrodes equally and does not lead to relative potential differences. The provided voltage is typically 150 V and can be adjusted for different electrodes by the use of voltage dividers. The middle electrodes can all be adjusted individually, while for the end-cap electrodes only the relative voltage of the four rods on each side of the trap region can be adjusted. By tuning the voltages of the middle and end-cap electrodes the positions of the ions is moved so that it coincides with the the potential minimum

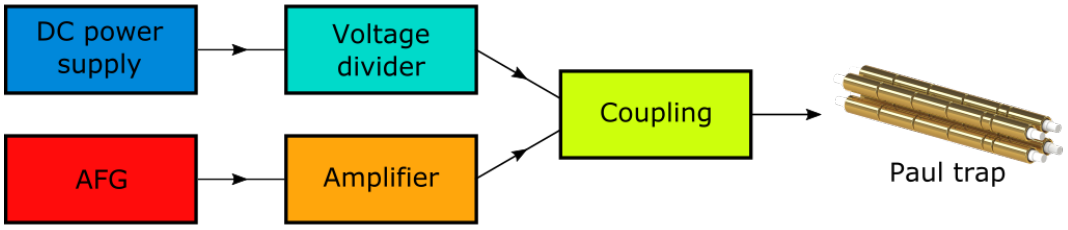

Figure 3.3: Scheme of the electronics for the Paul trap. The DC voltages and the RF voltages are produced separately and are then coupled. The coupled signal is sent to the Paul trap. A more detailed description can be found in the text.

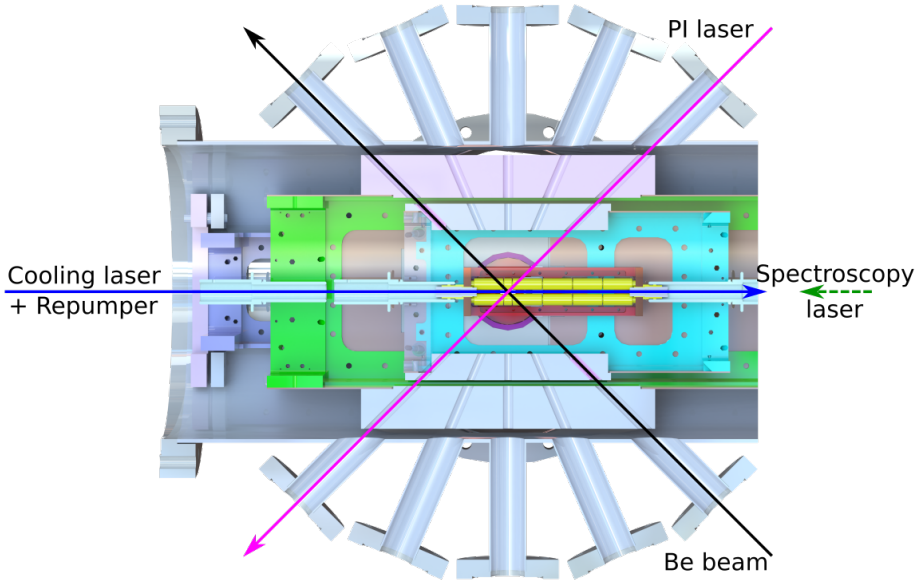

Figure 3.4: Optical setup for the experiments presented in this thesis seen as a top view. The ^{9}Be beam crosses the PI laser under an angle of 90° to reduce the first order Doppler shift and to produce $^9Be^+$ ions through resonance-enhanced two-photon ionization. Cooling laser and repumper pass through the trap centre along the trap axis. It is possible to sent in a spectroscopy laser collinear with the cooling laser and repumper through the trapping region.

of the RF voltage. The voltage difference between end-cap electrodes and middle electrodes is typically $\approx 1\,\mathrm{V}$.

The RF voltage is generated by an arbitrary function generator (AFG), with a peak-peak voltage of 460 mV and a frequency of 4.23 MHz. A RF amplifier is used to increase the peak voltage, since much higher amplitudes are required for trapping. Inside the coupling box a transformer is used to generate two opposite RF phases from this input for the different electrodes (see Fig. 2.1) and to further increase the peak-peak amplitude to 45 V at the trap the trap electrodes.

Each individual DC voltage is coupled with the corresponding RF voltage using a low pass filter with a cutoff frequency of $\approx 2\,\mathrm{Hz}$. The RF voltage can be adjusted for each individual electrode through a capacitive voltage divider. This is used for reduction of excess micromotion and was implanted in [29].

3.3 Optical arrangement

Optical access to the trap centre is granted by 13 optical ports, which are shown in the sectional view of the Paul trap from the top in Fig. 3.4. Beryllium is injected into the trap using a neutral ^{9}Be beam generated by an oven and sent

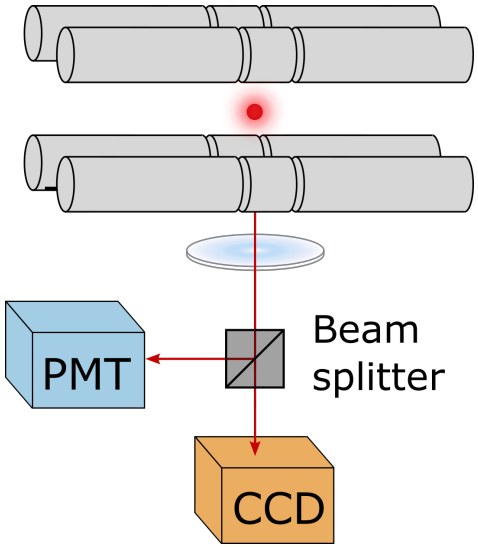

Figure 3.5: Schematic drawing of the imaging system. Ions stored in the Paul trap are imaged onto a CCD camera using a lens. In between lens and CCD camera a beam splitter is used to send 50 % of the photons to a photomultiplier tube (PMT). Adapted from [29].

collimated through the trap centre. The laser system for experimentation with $^9Be^+$ ions consists of a photoionization (PI) laser, a cooling laser, and a repumper. Here only the positions of the lasers, the atomic beam relative to the trap, as well as the imaging system are described. The oven and laser systems themselves are discussed in more detail in Sec. 4.

The PI laser is sent through the trap centre with an angle of 45° with respect to the trap axis and the ^{9}Be beam has an angle of $-45°$ with respect to the trap axis so that the angle between PI laser and ^{9}Be beam is 90° to reduce the first order Doppler shift. The cooling laser and repumper pass through the trapping region in axial direction. For spectroscopy of HCI, a spectroscopy laser can be guided into the trap along the axial direction, opposite to the cooling laser and repumper.

The following description of the imaging system is based on [20], which should be referred to for more details. The imaging system is placed below the trap (see Fig. 3.1) and the schematic setup is shown in Fig. 3.5. It consists of an aspheric lens mounted onto the 4 K stage at a distance of 25 mm to the trap centre, which images the ions on to a charge-coupled device (CCD) camera (*iStar 340T* from *Andor*) with 2048 pixel × 512 pixel and a pixel size of 13.5 µm × 13.5 µm. The magnification was measured in this thesis to be $M = -15.82 \pm 0.03$, giving a conversion factor of 1 pixel $\widehat{=}$ (0.853 ± 0.002) µm (see Sec. 5.2). Additionally, a 50 : 50 beam splitter is placed in between lens and CCD camera to sent 50 % of the light to a photomultiplier tube (PMT), which has a much higher temporal

resolution than the CCD camera, though it does not provide spatial resolution.

Chapter 4

Generation and cooling of $^9Be^+$

At CryPTEx, $^9Be^+$ ions are produced from neutral beryllium atoms through resonance-enhanced two-photon ionization in the trapping region. The produced ions are then stored in the cryogenic Paul trap and laser cooled. In this chapter the oven for the production of a ^{9}Be beam as well as the laser systems for its ionization and cooling of the $^9Be^+$ ions are described. Maintenance of the laser systems was performed as part of this thesis and they are intended to be used for CryPTEx II.

4.1 Beryllium oven

The ^{9}Be atomic beam is provided by an oven placed in a ultra high vacuum environment, which is attached to the vacuum chamber of the Paul trap and separated by a valve. It is only opened when new $^9Be^+$ ions are loaded into the trap. The oven consists of a crucible with 10 µg Be foil inside, which is electrically heated using a heating coil. The beryllium evaporates at ≈ 1250 K and the atoms leave in the direction of the trap region, passing through multiple skimmers, which are used for differential pumping. The skimmers additionally collimate the beam, which reduces the amount of beryllium deposited on the electrodes, which over time would lead to electrical patch potentials and thus to excess micromotion. Additionally, the velocity distribution in transverse direction becomes narrow, reducing the Doppler shift to a few MHz, when crossed with the photoionization laser at 90°. For a more detail discussion of the oven see [20].

4.2 Photoionization laser

^{9}Be is ionized by means of resonance-enhanced two-photon ionization. A photon with wavelength 235 nm excites the $2s^1S_0 \rightarrow 2p^1P_1$ transition with a natural

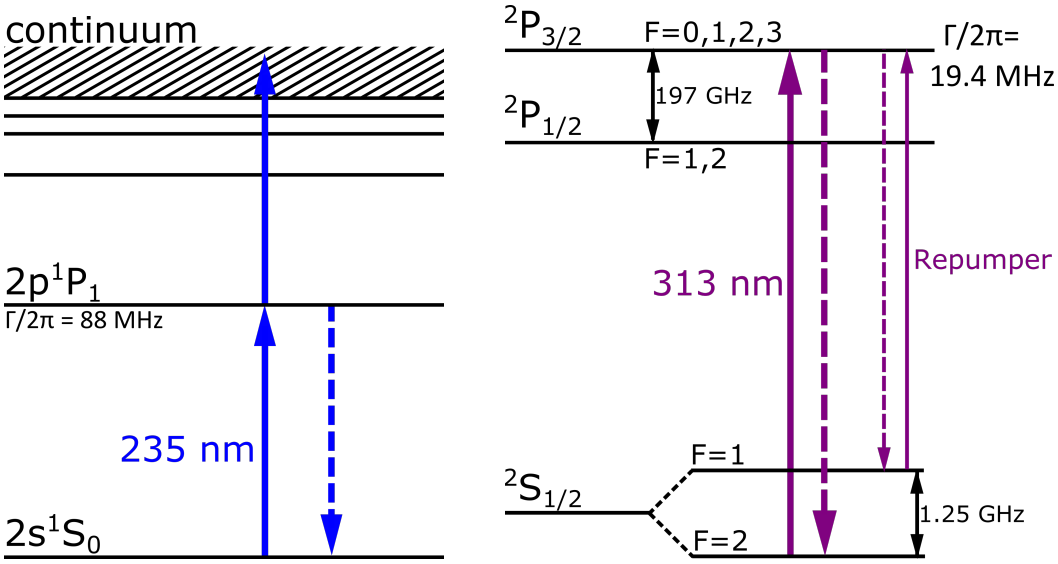

Figure 4.1: Left: Level scheme for photoionization of neutral ^{9}Be atoms. A 235 nm photon excites the $2s^1S_0$ ground state resonantly to the first excited state $2p^1P_1$. From there a second photon with a wavelength < 307 nm can transfer the electron into the continuum. Therefore, a single laser at 235 nm can photoionize ^{9}Be efficiently through the described two-photon process. **Right:** Level scheme for laser cooling of $^9Be^+$. The $^2S_{1/2},\ F = 2 \leftrightarrow {}^2P_{3/2}$ transition at about 313 nm is used for Doppler cooling. Due to the 1.25 GHz hyperfine splitting of the ground state, the excited state can decay into the $^2S_{1/2},\ F = 1$ state, removing the ion from the cooling cycle. Therefore, a repumper is required, which drives the $^2S_{1/2},\ F = 1 \leftrightarrow {}^2P_{3/2}$ transition. The hyperfine splitting of the $^2P_{3/2}$ is not resolved.

linewidth $\Gamma/2\pi = 88$ MHz. From there a second photon with the same wavelength can transfer the electron to the continuum (see Fig. 4.1). The photoionization (PI) laser design is based on [45] and consists of a commercial diode laser at 940 nm which is twice frequency doubled. The setup is shown in Fig. 4.3 and is described shortly in the following.

The diode laser (*TA Pro* from *Toptica*) has a maximum output power of 1.5 W at 940 nm. The light coming from the laser is sent through an optical isolator to prevent damage from back-reflections into the laser. It then passes through a $\lambda/2$-waveplate and a telescope to adjust the polarization and for mode-matching to the first bow-tie cavity. Inside the cavity, a periodically poled potassium titanyl phosphate (PPKTP) crystal is used for second harmonic generation, producing 470 nm light. This is coupled out of the cavity through the mirror directly after the crystal, which is highly reflective for 940 nm and has a high transmittance for 470 nm. For optimal quasi-phase matching the crystal is kept at approximately 22 °C. A PPKTP crystal is chosen for its high non-linearity and transparency at both wavelengths.

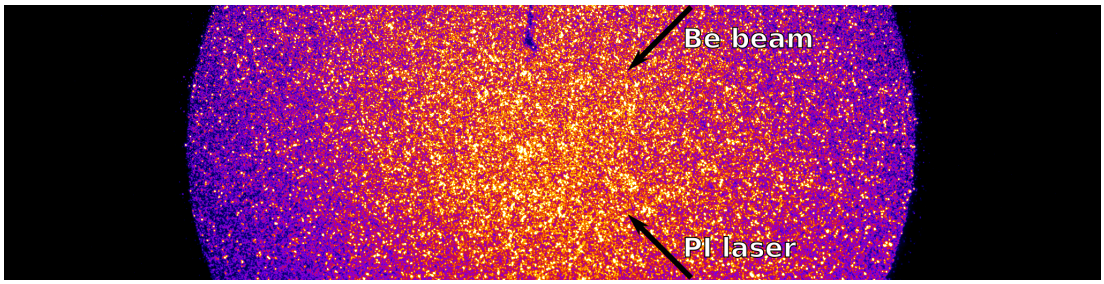

Figure 4.2: CCD image of the fluorescence produced by excitation of the $2s^1S_0 \rightarrow 2p^1P_1$ transition of neutral ^{9}Be atoms. The image was taken with a heating power of the Be oven approximately 70 % larger than typically used for loading the trap to increase visibility.

The 470 nm light is sent to a second bow-tie cavity, before which a telescope is placed for mode-matching. Inside the cavity, second harmonic generation of 235 nm light is achieved by using a beta barium borat (BBO) crystal with Brewster cuts at the ends to reduce reflections and with a phase-matching angle of 58.15°. The outcoupled light at 235 nm is sent through a cylindrical lens to compensate for astigmatism and goes on to the experiment.
Both cavities are locked using the Pound-Drever-Hall method, described in Sec. 2.6.2.2. For this the initial beam is modulated with sidebands inside the commercial system. They lie within the linewidth of the first cavity and are therefore carried over to the second cavity, making it possible to lock the second cavity using the same sidebands and without modulating the laser a second time. Typically an output power of 1 W from the diode laser generates about 200 mW at 470 nm. The second stage then produces 10 mW of output power at 235 nm. The total efficiency is about 1 %. During the measurements typically about 5 mW of 235 nm light before the Paul trap are used.
Deexcitation from $2p^1P_1 \rightarrow 2s^1S_0$ happens alongside ionization, since the $2s^1S_0 \rightarrow 2p^1P_1$ transition is resonantly excited. This can be used to optimize the alignment and achieve maximal overlap of the ^{9}Be beam and the PI laser by measuring the fluorescence. A CCD camera image of this fluorescence is shown in Fig. 4.2.

4.3 Laser cooling of $^9Be^+$

The generated $^9Be^+$ ions are cooled to the mK regime using Doppler cooling through the $^2S_{1/2} \leftrightarrow {}^2P_{3/2}$ transition at a wavelength of about 313 nm with a natural linewidth of $\Gamma/2\pi = 19.4$ MHz. The level scheme of $^9Be^+$ is shown in Fig. 4.1, which shows that the $^2S_{1/2}$ ground state has a hyperfine splitting of 1.25 GHz. Therefore, the excited $^2P_{3/2}$ state will either decay into the $F = 1$ or

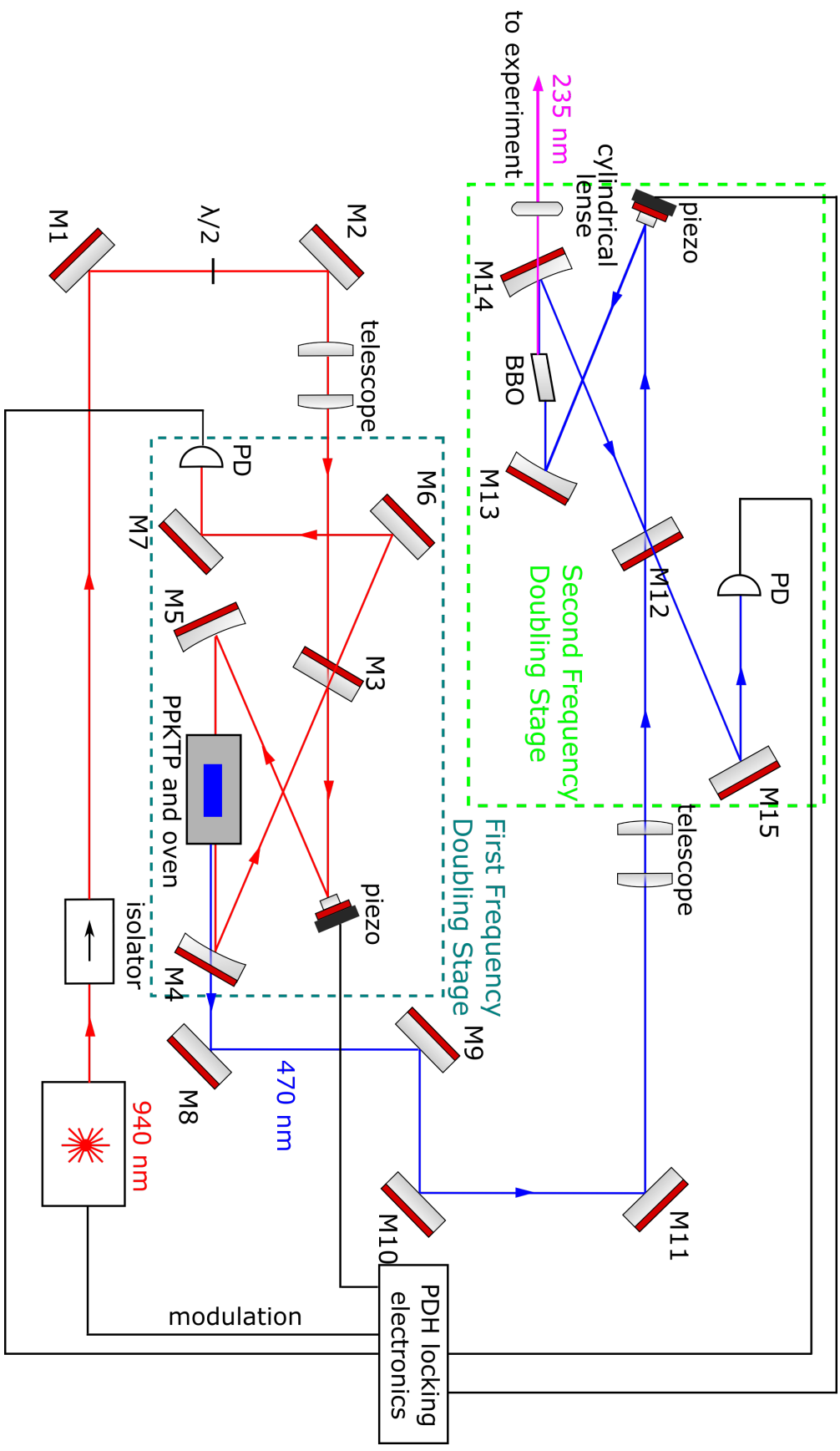

Figure 4.3: Setup of the photoionization laser. The diode laser produces 940 nm light, which is twice cavity-enhanced frequency doubled to generate 235 nm laser. Details are given in the text. Abbreviations: Mx - mirror, DM - dichroic mirror, $\lambda/2$ - waveplate, PD - photodiode. Adapted from [20].

the $F = 2$ hyperfine state. The $F = 1 \leftrightarrow F = 2$ transition is dipole forbidden, i.e. long-lived and any ion in the $F = 1$ state is effectively removed from the cooling cycle. Therefore, two lasers are required: a cooling laser for the $^2S_{1/2},\ F = 2 \leftrightarrow {}^2P_{3/2}$ transition at 313 nm and a 1.25 GHz frequency shifted repumper for the $^2S_{1/2},\ F = 1 \leftrightarrow {}^2P_{3/2}$ transition.

The design of the laser system is based on [46]. The starting point are two fibre laser at 1550 nm and 1050 nm respectively. Sum frequency generation of these produces 626 nm light. This is then cavity-enhanced frequency doubled generating the required 313 nm. The setup is shown in Fig. 4.4.

The fibre lasers are commercial systems consisting of two seed lasers (*Koheras Adjustik* from *NKT Photonics*) and two amplifiers (textitKoheras Boostik from *NKT Photonics*), producing up to 5 W of output power at 1050 nm and 1550 nm each. The light coming from each fibre laser is sent through an isolator to prevent damage from back scattering of any light into the lasers. $\lambda/2$-waveplates and telescopes are used to adjust the polarization and the beam parameters of each beam individually. The beams are overlapped using a dichroic mirror and focused into a periodically poled lithium niobate (PPLN) crystal for sum frequency generation. To achieve optimal phase-matching the crystal is heated to about 193 °C. The generated 626 nm and the non-conversed light are separated using a dichroic mirror. The non-converted light is sent into a beam dump, the 626 nm photons are guided to the next stage.

The frequency doubling stage uses a beta barium borate (BBO) crystal inside a bow-tie cavity for second harmonic generation. The BBO has a Brewster cut for 626 nm at the ends and a phase-matching angle of 38.4°. In front of the cavity a $\lambda/2$-waveplate is placed to control the polarization and a telescope is used for mode-matching to the cavity. The frequency doubled light leaves the cavity through the outcoupling mirror, which has a high transmittance for the generated 313 nm light, while being highly reflective for 626 nm photons. Behind the cavity, a cylindrical lens is used to compensate for the occurring astigmatism. The cavity is locked using the Hänsch-Couillaud method described in Sec. 2.6.2.1. For power stabilization a motorized $\lambda/2$ waveplate controlling the polarization of the 626 nm light is inserted between the first and the second stage. A with a photodiode detected 313 nm reflex of the cavity is used as a reference for a PID controller, which controls the motorized waveplate. The adjusted light is sent through a Glan-Taylor polarizer which transmits only a certain polarization. The transmitted power is therefore dependent on the orientation of the $\lambda/2$ waveplate and can be controlled this way. For a detailed description and analysis see [47]. Typically about 100 mW of 313 nm light can be produced from 800 mW at 626 nm

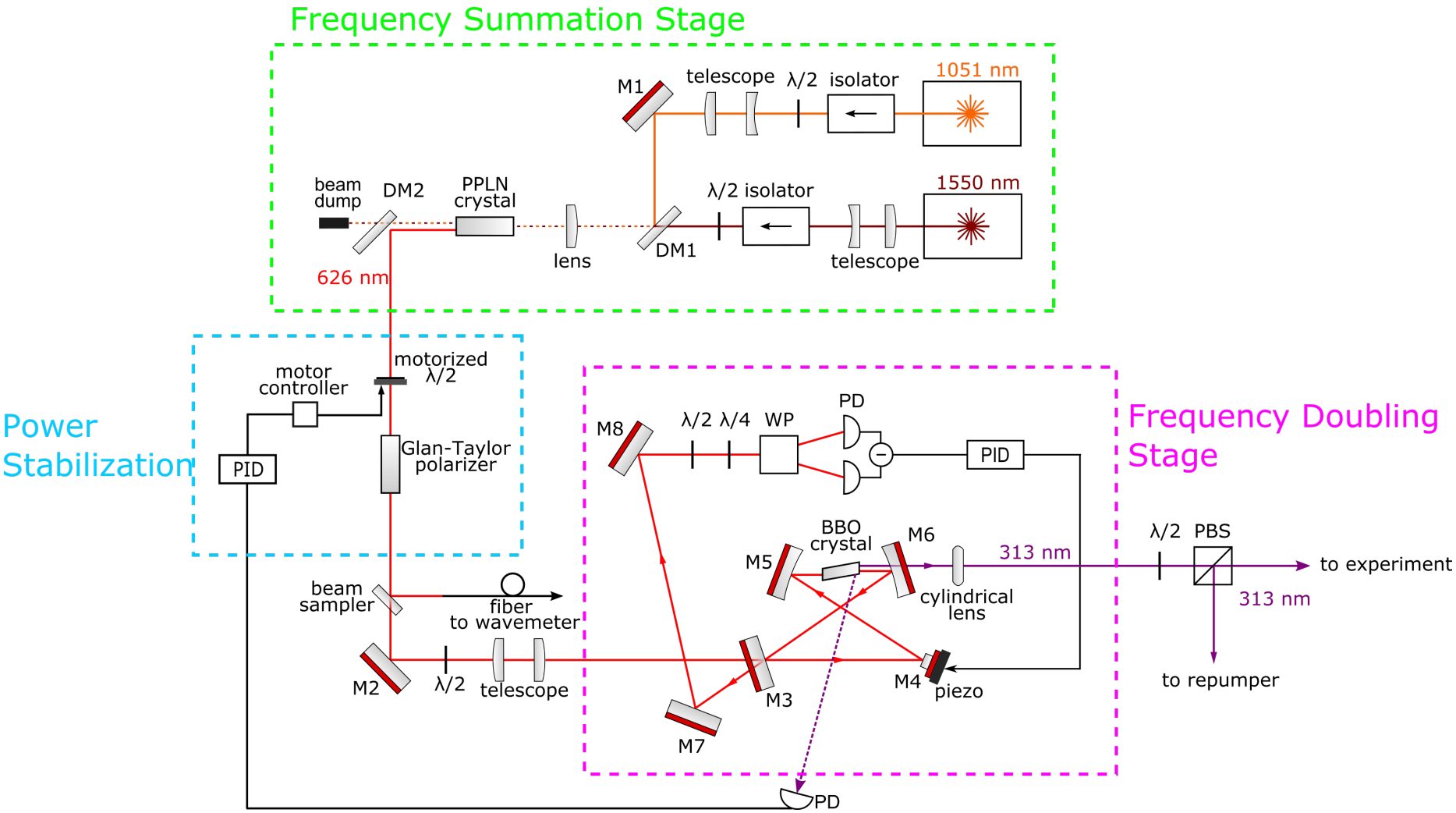

Figure 4.4: Setup of the cooling laser. Starting point are two fibre lasers with wavelengths of 1050 nm and 1550 nm. Through sum frequency generation 626 nm light is produced, which is cavity-enhanced frequency doubled to get 313 nm photons. A description is given in the text. Abbreviations: Mx - mirror, DM - dichroic mirror, $\lambda/2$, $\lambda/4$ - waveplate, WP - Wollaston prism, PBS - polarizing beam splitter, PD - photodiode. Adapted from [20].

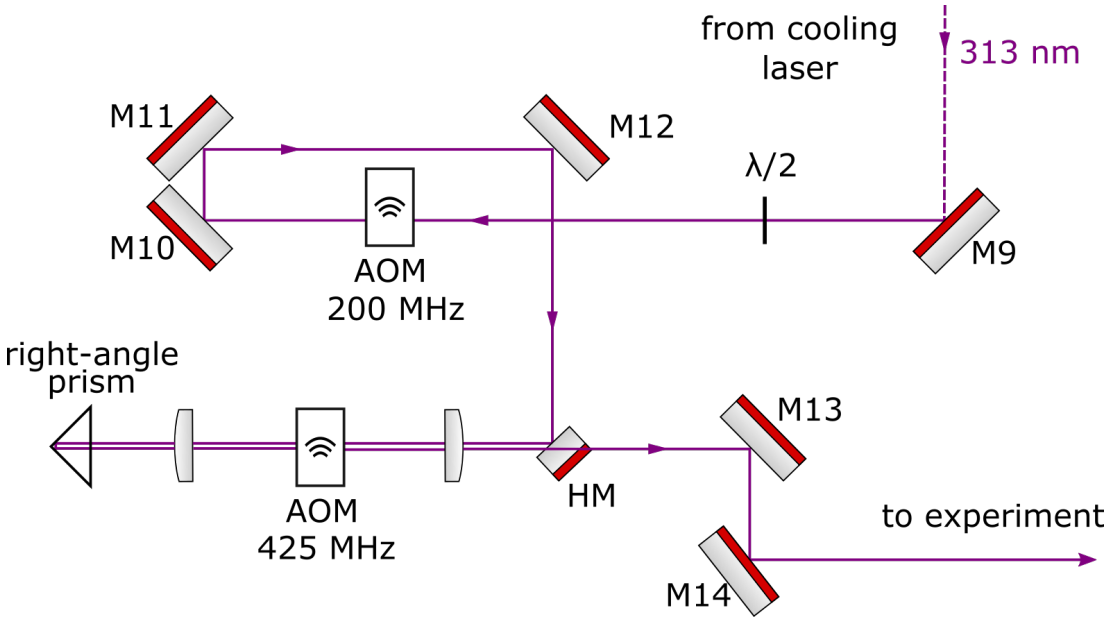

Figure 4.5: Setup of the repumper, which frequency shifts parts of the cooling laser at 313 nm by −1.05 GHz. This is necessary to account for the hyperfine splitting of the $^2S_{1/2}$ ground state. The frequency shift is achieved by sending the laser through an AOM with a frequency of 200 MHz at -1st order and subsequently on to a second AOM with 425 MHz were it is sent through twice at (-1st,-1st) order using a right-angle prism. Abbreviations: Mx - mirror, AOM - acousto-optical modulator, HM - half mirror.

before the cavity. About 60 % of the 313 nm light are sent to the experiment for laser cooling and the remaining 40 % are sent to the repumper. The ratio is regulated by a combination of a $\lambda/2$-waveplate and a polarization dependent beam splitter.

The current setup for the repumper is shown in Fig. 4.5. Overall a frequency shift of 1.25 GHz between cooling laser and repumper needs to be achieved. The cooling laser has a second power stabilization directly at the Paul trap using a 200 MHz acousto-optic modulator (AOM) in +1st order (see [47]), therefore the repumper only needs to be shifted by −1.05 GHz. This is done using two AOMs, one with 200 MHz and one with 425 MHz. The laser passes through the first AOM once in -1st order gaining −200 MHz and is then sent twice through the second AOM in (-1st,-1st) order. This is done using a right-angle prism to sent the beam back after the first pass (see Fig. 4.5) and gives an additional −850 MHz shift, adding up to −1.05 GHz. The efficiency of the repumper is approximately 20 %. In a previous setup the power stabilization was not implanted and the beam was sent twice thorough the first AOM using a right-angle prism.

To measure and adjust the wavelength of the laser a wavelength meter (*Wave-*

length Meter Ångstrom WS Ultimate 10 from *High Finesse*) is used. The wavelength of 626 nm light before the cavity is used for stabilization, since there are no efficient fibres for transportation of UV light commercially available. The wavelength can then be regulated to a set value, by changing the wavelength of one of the commercial lasers through a piezo.

4.4 Temperature estimation

To give an upper bound for the temperature of a single $^9Be^+$ ion in axial direction T_{axial} the fluorescence as a function of the cooling laser frequency was measured. This allows to estimate the temperature, since the line profile of the $^2S_{1/2} \leftrightarrow {}^2P_{3/2}$ transition is affected by Doppler broadening caused by thermal motion. This measurement was performed previously at CryPTEx in [20] and was repeated here to estimate T_{axial}.
The line profile of the cooling transition as a function of the laser detuning describing the fluorescence consists of multiple contributions. Fundamentally, the line shape is described by a Lorentzian function with the natural linewidth $\Gamma/2\pi = 19.4\,\text{MHz}$. This width is broadened mainly by two effects. Firstly, it is increased by saturation broadening to

$$\Gamma_{\text{sat}} = \Gamma\sqrt{1+s_0}, \tag{4.1}$$

with the saturation parameter defined in Eq. (2.24). This only widens the spectral line, but does not alter the underlying line shape and is described by Eq. (2.23). The second effect is Doppler broadening due to the Maxwell-Boltzmann distributed thermal motion at temperature T. This gives a Gaussian lineshape, with a full width at half maximum (FWHM) of [48]

$$\Gamma_{\text{D}} = \frac{2\pi}{\lambda_0}\sqrt{8\ln(2)\frac{k_{\text{B}}T}{m}}, \tag{4.2}$$

where λ_0 is the wavelength of the cooling transition on resonance. The combined effect of saturation and Doppler broadening is described by the convolution of the individual line profile, which is called a Voigt profile. If $\Gamma_{\text{sat}} \gg \Gamma_{\text{D}}$ or $\Gamma_{\text{sat}} \ll \Gamma_{\text{D}}$, the profile is mostly described by a Lorentzian or a Gaussian function respectively. For the measurement, a single $^9Be^+$ ion is trapped and the detuning of the laser is changed in steps of $5 \times 10^{-6}\,\text{nm}$, coming from far red detuning. At each step the fluorescence in a small region of interest around the ion is measured using the CCD camera with an exposure time of 1 s. The resulting data can be seen in

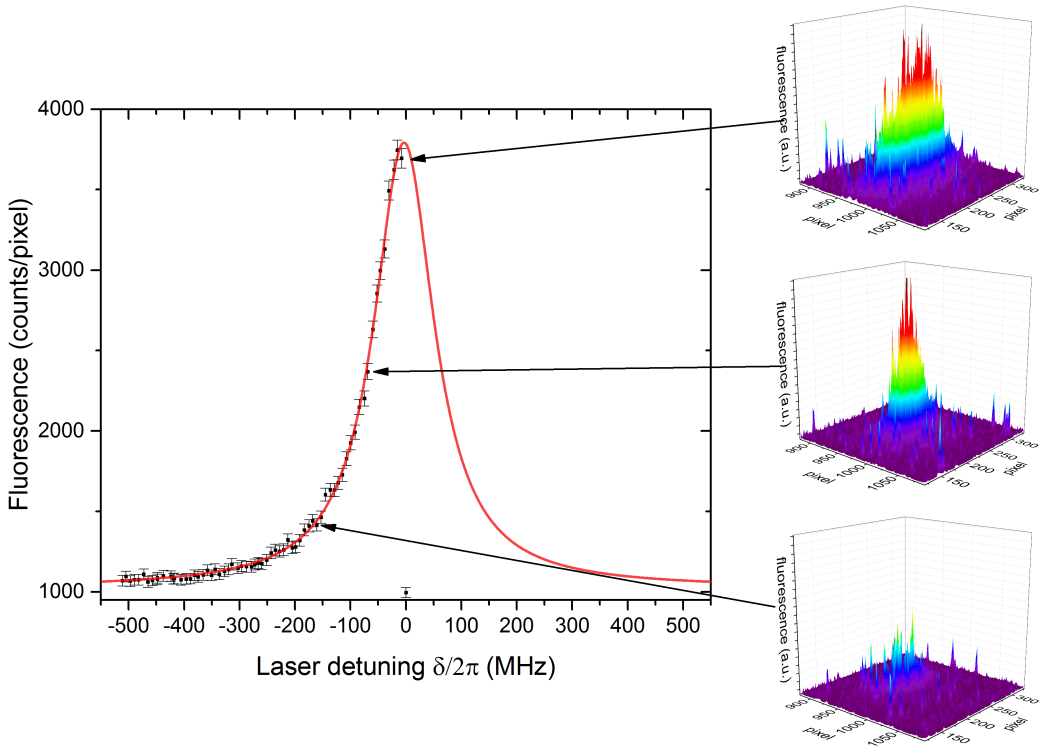

Figure 4.6: Measurement of the fluorescence of a single $^9Be^+$ ion as a function of the cooling laser detuning. Starting in the far red detuned, the fluorescence increases as the the frequency gets closer to resonance. On resonance the ion is lost, since for blue detuning heating instead of cooling occurs. The fitted function is a Lorentzian with $\Gamma/2\pi = (132 \pm 2)\,\mathrm{MHz}$ and $\chi^2_{\mathrm{red}} \approx 0.5$. The graphs on the right show the CCD camera images of the ion at the indicated detunings.

Fig. 4.6. The error is given by $\sqrt{N}$, where N is the measured fluorescence per pixel in the region of interest. Only for a red detuning of the cooling the ion is trapped, since for blue detuning the ion is heated instead of cooled, which results in the loss of the ion. Performing a Voigt fit shows that the Gaussian width is compatible with $\Gamma_{\mathrm{D}}/2\pi = 0\,\mathrm{MHz}$ within $\ll 1\sigma$ at $\chi^2_{\mathrm{red}} \approx 0.5$. Therefore a fit with a Lorentzian function is performed, which is shown in Fig. 4.6, giving a linewidth of $\Gamma/2\pi = (132 \pm 2)\,\mathrm{MHz}$ at $\chi^2_{\mathrm{red}} \approx 0.5$, indicating a high fidelity of the fit.
To estimate an upper bound for the temperature, different Voigt functions with a fixed Gaussian width are fitted corresponding to a fixed temperature. The temperature is increased until χ^2_{red} started to increase significantly. This point is then taken as an upper bound for the temperature and yielded $T_{\mathrm{upper}} \approx 40\,\mathrm{mK}$. The lower limit is identical to the Doppler limit given in Eq. (2.29) with $T_{\mathrm{D}} = (3.17 \pm 0.05)\,\mathrm{mK}$ for the measured linewidth Γ. Overall the temperature is estimated to be

$$3\,\mathrm{mK} \lessapprox T_{\mathrm{axial}} \lessapprox 40\,\mathrm{mK}. \tag{4.3}$$

This result needs to be treated carefully, since it only gives a rough estimation. By scanning the laser frequency, the temperature of Doppler cooling is also changing according to Eq. (2.28). For $\delta \leq \Gamma/2$, it increases only slowly with detuning (see Fig. 2.4) and for the farthest detuned data point, the temperature is limited to $\approx 12\,\mathrm{mK}$. For $\delta \geq \Gamma/2$ the increase of the temperature with detuning is much steeper and the last data point should have a minimal temperature of $\approx 20\,\mathrm{mK}$. Both points represent extreme detunings and all other data points are taken at lower temperatures. Therefore all data points are expected to be taken at an ion temperature within the estimated temperature range.

Chapter 5

Measuring coherent ion motion

In the following chapter the axial excess micromotion of a single $^9Be^+$ ion and the driven centre of mass (COM) motion for different numbers of $^9Be^+$ ions are measured using a photon-correlation technique [28], which relies on the motion being driven and in phase with its driving force. This motion modulates the fluorescence signal as a function of time, which can be measured.
For the measurements it is assumed that the driven ion motion along the propagation direction of the cooling laser can be described as

$$x(t) = A\cos(\omega t), \tag{5.1}$$

where A is the amplitude and ω is the frequency of the motion. It is essential that the frequency of the motion is always equal to the frequency of the driving force. The motion modulates the fluorescence Λ due to the Doppler effect (see Eq. (2.23)):

$$\Lambda = \Gamma\rho_{ee} = \frac{\Lambda_0}{1 + (2\delta/\Gamma_{\text{eff}}(1 - kv_{\max}/\delta\sin(\omega t + \varphi)))^2}, \tag{5.2}$$

where the effective linewidth $\Gamma_{\text{eff}} = \Gamma\sqrt{1+s_0}$ due to power broadening is introduced and

$$\Lambda_0 = \frac{\Gamma s_0}{2(1+s_0)}. \tag{5.3}$$

In order to characterize the ion's motion $x(t)$ in the trap, the fluorescence as a function of time is measured. As the oscillation frequency ω of the driven motion equals the frequency of the driving field, it is sufficient to record the number of scattered photons as a function of the excitation signal's phase.
To measure the modulation of the fluorescence a data acquisition system is required with a temporal resolution much larger than the period of the ion's motion $\ll 2\pi/\omega$, which is $\approx 250\,\text{ns}$ for the micromotion at the radio frequency

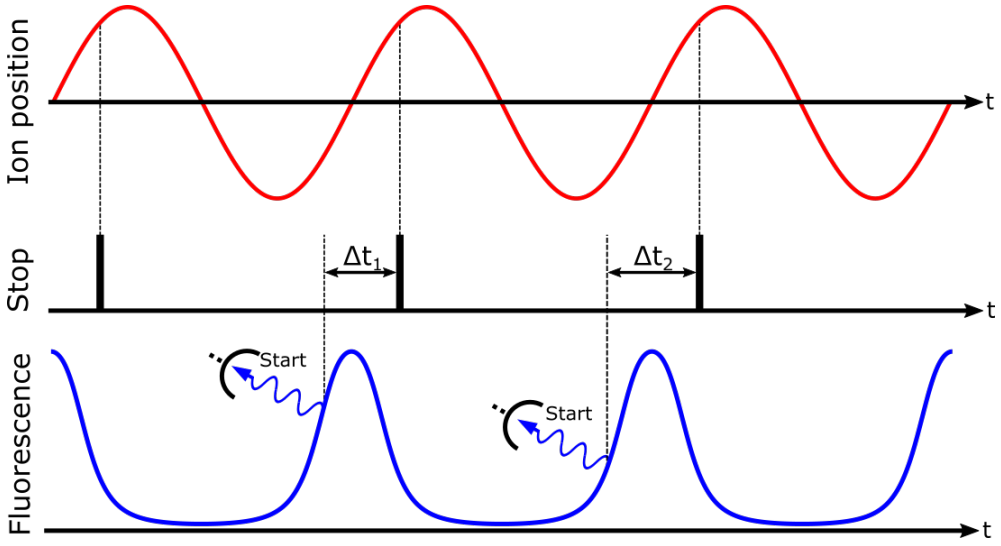

Figure 5.1: Measurement principle of the used photon-correlation method. The ion moves harmonically and in phase with a driving force. The fluorescence becomes modulated with the driving frequency ω due to the first order Doppler shift generated by this motion. The time between a single photon and a periodical stop signal in phase with the driving force is measured. This probes the fluorescence as a function of the phase of the driving force for sufficiently many photons.

$\omega/2\pi = \Omega/2\pi = 4.23\,\mathrm{MHz}$ and $\approx 10\,\mu\mathrm{s}$ for the COM mode at a trap frequency of $\omega/2\pi = \omega_z/2\pi \approx 100\,\mathrm{kHz}$. Therefore, to detect a scattered photon a PMT is used, which produces pulses with a width of 10 ns and has a pulse pair resolution of 20 ns. These pulses are sent to an analog-to-digital converter converter (ADC, model *7072T Dual Timing ADC* from *FAST ComTec*). The ADC operates in time to digital conversion mode (TDC) where it produces a voltage which is proportional to the time difference between a start and a stop pulse. The measured time intervals are sorted by their length and are counted into one of 8192 channels, where a higher channel number corresponds to a longer time. As a start pulse the pulses coming from the PMT are used. The stop signal is the synchronization output of the function generator, which drives the ion. Therefore, the fluorescence is measured as a function of the the driving AC field. The principle is illustrated in Fig. 5.1.

In the following chapters the used ADC will be characterized and a time calibration is performed. Then the secular motion for multiple amounts of ions is measured and is used to determine the trap frequency. The trap frequency and two $^9Be^+$ ions are used to infer the magnification of the imaging system. Finally, a measurement of the axial excess micromotion of a single $^9Be^+$ ion is shown.

5.1 Characterization of the ADC

The maximal time difference the ADC can convert to a channel can be adjusted and is called the conversion time. It needs to be $> 2\pi/\omega$ for the presented usage. For the measurement of the micromotion a conversion time of $t_{\mathrm{MM}} = 500\,\mathrm{ns}$ and for the COM mode a conversion time of $t_{\mathrm{COM}} = 20\,\mu\mathrm{s}$ is used. For both settings the resolution is measured, corrections for systematic errors are performed and a time calibration is determined.

5.1.1 Temporal resolution

The temporal resolution of the ADC is measured using an AFG with two synchronized outputs, which are both generating pulses with a frequency of 10 kHz. The beating of the two signals is measured for t_{MM} and t_{COM} and a Gaussian function with a fixed offset of zero is fitted to the data. Only channels with non-zero counts are taken for the fit with an error of $\sqrt{N}$ (N: counts). The result for t_{COM} is shown in Fig. 5.2. The full width at half maximum (FWHM) gives a measure for the temporal resolution of the data acquisition system and is determined to be

$$\begin{aligned} t_{\mathrm{COM}}: &\quad \mathrm{FWHM} = (2.545 \pm 0.005) \quad \text{channel}, \\ t_{\mathrm{MM}}: &\quad \mathrm{FWHM} = (2.546 \pm 0.002) \quad \text{channel}. \end{aligned} \tag{5.4}$$

With the time calibration performed in Sec. 5.1.3 this can be converted to

$$\begin{aligned} t_{\mathrm{COM}}: &\quad \mathrm{FWHM} = (5.56 \pm 0.01) \times 10^{-3}\,\mu\mathrm{s}, \\ t_{\mathrm{MM}}: &\quad \mathrm{FWHM} = (150.2 \pm 0.1) \times 10^{-3}\,\mathrm{ns}. \end{aligned} \tag{5.5}$$

This shows that the temporal resolution satisfies the requirement $\ll 2\pi/\omega$.

5.1.2 Normalisation

It is also observed that not every channel of the ADC counts at equal rates. This is also shown in the manual [49] and an inherent property of the system. It is particularly prominent in the case of the micromotion measurement for channels $\lessapprox 500$ as shown in Fig. 5.2. To account for this noise is measured for multiple hours, which should give a constant signal in the ideal case of identical ADC channels. Any deviation is expected to be a characteristic of the ADC. The noise is generated by two AFGs with different frequencies, which were chosen in such a way that no beating occurred. From the resulting data a correction factor for

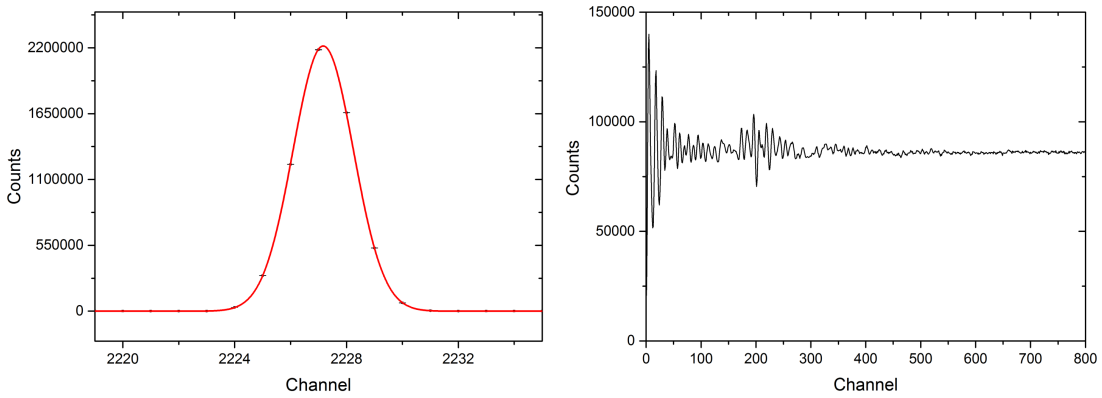

Figure 5.2: Left: Temporal resolution of the ADC for t_{COM}. The signal is generated from the beating of two synchronized signals and a Gaussian function is fitted. The FWHM is given in Eq. (5.4) and gives a measure of the temporal resolution. **Right:** Noise measured with the ADC at t_{MM}. It shows that not all channels count at equal rates. In particular the channels $\lessapprox 500$ show systematic differences, which is inherent to the ADC [49].

each channel is determined by calculating its ratio with respect to a reference channel. The reference is randomly chosen from the centre. Additionally, the first 100 channels were removed from the data, since these showed the largest systematics.

5.1.3 Time calibration

For the time calibration of the ADC it is used that the stop signal is periodic with the driving frequency ω. Therefore, if the conversion time is larger than $2\pi/\omega$, the maximum time that can be recorded is $2\pi/\omega$. A time calibration is then done by varying ω. The highest channel, which data is written to is determined and is assigned to the time $2\pi/\omega$. To reduce measurement time a second AFG is used as a start signal with a frequency of $\approx 10\,\mathrm{kHz}$ for the t_{COM} calibration and $\approx 100\,\mathrm{kHz}$ for the t_{MM} calibration. The starting frequency has to be chosen in a way such that no beating between the start and stop signal occurs. 10 different stop frequencies were used for t_{COM} and 14 different stop frequencies were used for t_{MM} . At each frequency noise is recorded for two to three minutes and the counts for all frequencies were summed up. The acquired data for t_{COM} is shown in Fig. 5.3.

The position of the steps are measured at half height with an estimated error of 3 channels, similar to the resolution. The error of the AFG frequency of the stop signal is neglected, since it is much smaller than the relative error of the channels. The positions of the steps are plotted as a function of $2\pi/\omega$ and a linear fit is performed. In Fig. 5.3 this is shown for t_{COM}. The inversion of the fit function

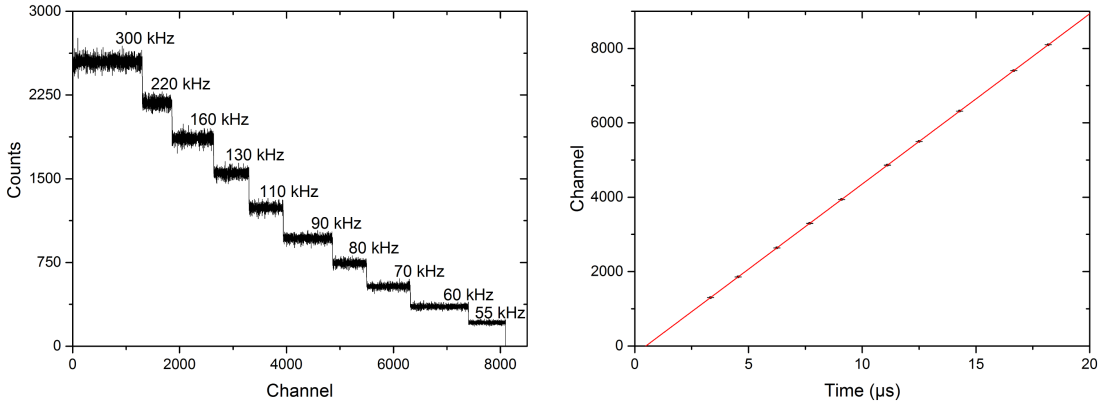

Figure 5.3: Time calibration for t_{COM}. **Left:** The last channel that can be written to for a given stop signal angular frequency ω corresponds to the time $2\pi/\omega$. By changing ω a time calibration can be found. **Right:** Channels as a function of the corresponding time. The inversion of the linear fit gives the time calibration.

gives the time calibration function

$$t = t_0 + a x_c, \tag{5.6}$$

where a is the slope, t_0 is the y-intersection and x_c represents the ADC channel. The fitted parameters are

$$t_{\mathrm{COM}}: \quad t_0 = (0.48663 \pm 0.0009)\,\mu\mathrm{s} \qquad a = (2.1852 \pm 0.0001) \times 10^{-3}\,\mu\mathrm{s}, \tag{5.7}$$

$$t_{\mathrm{MM}}: \quad t_0 = (2.74 \pm 0.02)\,\mathrm{ns} \qquad a = (59.001 \pm 0.007) \times 10^{-3}\,\mathrm{ns}. \tag{5.8}$$

5.2 Centre of mass mode

In this part the driven motion of the centre of mass mode is used to measure the trap frequency. It is extracted once from the motional amplitude and once from the relative phase between driving field and ion motion for different numbers of $^9Be^+$ ions. The trap frequency is used in the next section to calculate the magnification of the imaging system from an ion chain, consisting of two $^9Be^+$ ions.

To measure the COM mode a look at the equation of motion for an ion chain is taken on the basis of the discussion in Sec. 2.3.1. For a pure COM mode and no contribution from higher modes Eq. (2.46) can be written as

$$\ddot{q}_i + \omega_z^2 q_i = 0, \tag{5.9}$$

which is the equation of motion for a free harmonic oscillator. Although this was

derived by approximating the potential, it is an exact solution, since for the COM mode the distance between the ions does not change. The whole system can then be regarded as a single rigid object moving in a harmonic potential. Therefore, this description is also valid for a 3-dimensional crystal. For a single ion in a Paul trap this motion corresponds to the secular motion (see Sec. 2.1) and is in general incoherent. If an AC field with frequency ω is added to one of the Paul trap electrodes it couples to the ions with a force $F(t)/m \coloneqq K_0 \sin(\omega t)$. This modifies the equation of motion Eq. (5.9) to

$$\ddot{q}_i + 2\gamma\dot{q}_i + \omega_z^2 q_i = K_0 \sin(\omega t), \tag{5.10}$$

where a damping term γ was added to account for laser cooling, assuming γ to be constant over time and for all positions of the ion's motion. This describes a driven harmonic oscillator and results in a harmonic motion coherent with the driving field (see Sec. 2.4):

$$q_i = A(\omega)\cos(\omega t + \varphi(\omega)). \tag{5.11}$$

The amplitude $A(\omega)$ and phase $\varphi(\omega)$ are expected to be depending on ω/ω_z and γ/ω_z (see Eq. (2.54) and Eq. (2.55)). The applied AC voltage from the AFG used to drive the ion has typically a peak voltage of 200 mV - 500 mV, though this is not the voltage at the electrode, since a low pass filter is in between (see Sec. 3.2).

The simplest way to measure the COM mode is to take images with the CCD camera, where an increase in motional amplitude for a single ion can be seen close to the resonance frequency. An example is shown in Fig. 5.4. This method has the disadvantage that it only provides information about the amplitude and not the phase of the ion's motion, since the CCD camera takes pictures on a much slower time scales than $\omega/2\pi$. Additionally, driven, coherent motion can not be separate from thermal, incoherent motion. A complete description is difficult and not analytically known.

A more quantitative measurement can be obtained using the above described photon-correlation method, giving access to phase and amplitude of the ion's motion. This has the additional benefit of measuring only the coherent motion and effectively removing the incoherent motion as it only produces a homogeneous background. The scattering rate (5.2) becomes:

$$\Lambda = \Gamma\rho_{ee} = \frac{\Lambda_0}{1 + (2\delta/\Gamma_{\text{eff}}(1 - \omega k A(\omega)/\delta \sin(\omega t + \varphi)))^2}. \tag{5.12}$$

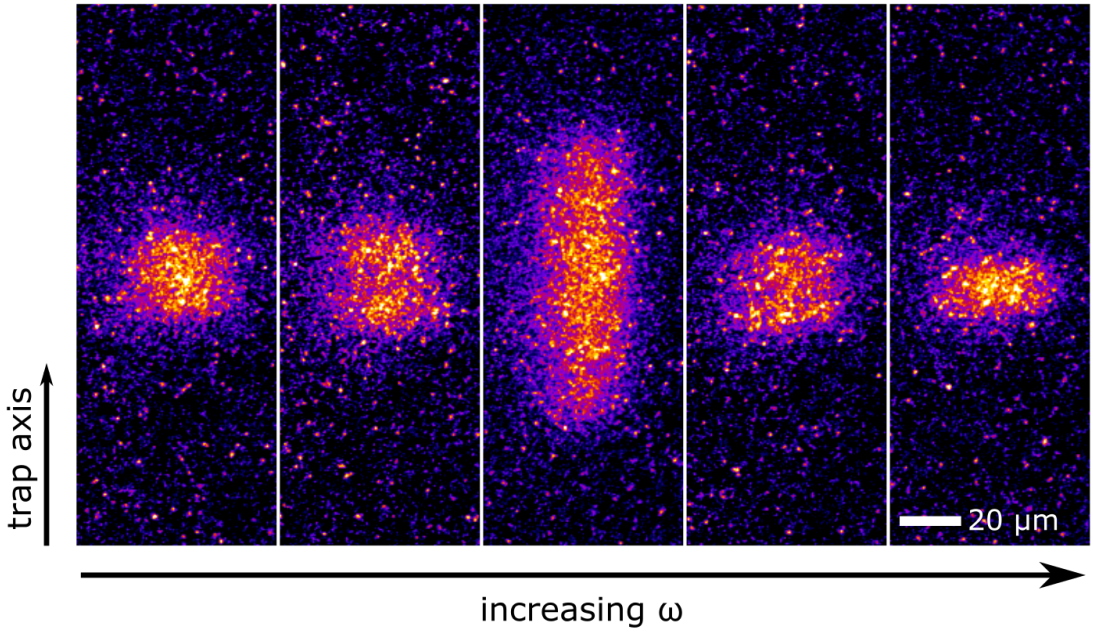

Figure 5.4: CCD camera images of a single ion driven by an AC field with different frequencies ω around the resonance frequency $\omega_R/2\pi \approx 70\,\text{kHz}$ and an amplitude of 500 mV at the AFG. The driving frequency increases by 10 kHz from left to right. The central image is recorded for $\omega \approx \omega_R$ and shows the maximal amplitude of the driven motion. Increasing or decreasing the excitation frequency reduces it. For $\omega \gg \omega_R$ the amplitude of the driven motion vanishes and only thermal motion remains. For $\omega \ll \omega_R$ the motional amplitude decreases to an asymptotic value larger than the thermal distribution. The detuning of the cooling laser is $\delta/2\pi \approx 170\,\text{MHz}$ and the saturation parameter is $s_0 \approx 20$.

From this function $kA(\omega)/\delta$ and $\varphi(\omega)$ can be extracted, which are fitted using the analytic solutions of the driven harmonic oscillator given by Eq. (2.54) and (2.55). From this the trap frequency ω_z can be obtained, which should be independent of the number of ions.

To get a first estimation of the trap frequency the CCD camera is used and ω is scanned through the AFG providing the AC voltage. From this the resonance frequency is estimated to be $\omega_R/2\pi \approx 81\,\text{kHz}$. A measurement using the PMT consisted of scanning the excitation frequency from 75 kHz to 90 kHz in steps of 1 kHz. At each point the fluorescence is measured for 2 min, except for the case of ≈ 100 ions where the measurement time is only 1 min. Afterwards, the RF voltage is turned off and the background is measured without trapped ions at each excitation frequency for 1 min, since the amount of ADC channels data is written to depends on the excitation frequency. The laser settings are typically

$\delta \approx 100\,\mathrm{MHz}$ and $s_0 \approx 12$.
The measured fluorescence and background are first normalised as discussed in Sec. 5.1. Then the average background per channel is calculated and subtracted from the data. A least square fit of Eq. (5.12) to the measured fluorescence signal is performed, where ω is held constant at the corresponding excitation frequency. The individual data points are weighted equally due to the large scattering of data points, which acts as an error. Examples for the result are plotted in Fig. 5.5.
This is performed for each excitation frequency and from the fits the fitting parameters kA'/δ and φ as functions of ω are extracted. So far it is neglected that in between the AFG and the electrodes a low pass filter is installed with a cutoff frequency $\approx 2\,\mathrm{Hz}$ (see Sec. 3.2). This means that the voltage applied to the electrodes varies as a function of ω and the resulting force $F \propto 1/\omega$. This does not effect $\varphi(\omega)$ (see Eq. (2.55)), though it changes $A(w) \propto F$ (see Eq. (2.54)). The fitted parameter $kA'(\omega)/\delta$ is scaled relative to the lowest excitation frequency $\omega_{\mathrm{start}}/2\pi = 75\,\mathrm{kHz}$ to account for this, i.e.

$$\frac{kA(\omega)}{\delta} = \frac{\omega}{\omega_{\mathrm{start}}} \frac{kA'(\omega)}{\delta}. \tag{5.13}$$

This is possible, since only the relative amplitude is relevant. Assuming that k and δ do not depend on ω, $kA(\omega)/\delta$ is plotted as a function of ω and Eq. (2.54) is fitted. $\varphi(\omega)$ is also plotted and fitted by Eq. (2.55). From the results the trap frequency ω_z is obtained.
The measurement is performed for one ion, two ions, four ions and a crystal consisting of $\approx$ 100 ions. The case of one and two ions can be described by an ion chain as discussed by in Sec. 2.3.1. Four ions are chosen, since for the used trap frequencies it is the lowest number of ions, which show a 3-dimensional structure. The results of the measurements, including CCD images of the used ions, are shown in Fig. 5.6. The extracted trap frequencies $\omega_z/2\pi$ are given in Tab. 2, where the errors are only given by the fitting errors, since these are dominating compared to any systematic effects of the ADC discussed in Sec. 5.1. For $\approx$ 100 ions no result could be obtained for the amplitude due to a low signal. This is probably related to the reduced measurement time of 1 min compared to 2 min for the other cases. The trap frequencies determined from the amplitude are significantly different to each other and significantly different to the results obtained from the phase for one and four ions. The results from the phases show no significant differences to each other.
In general the phase measurement is expected to be the more reliable, since the

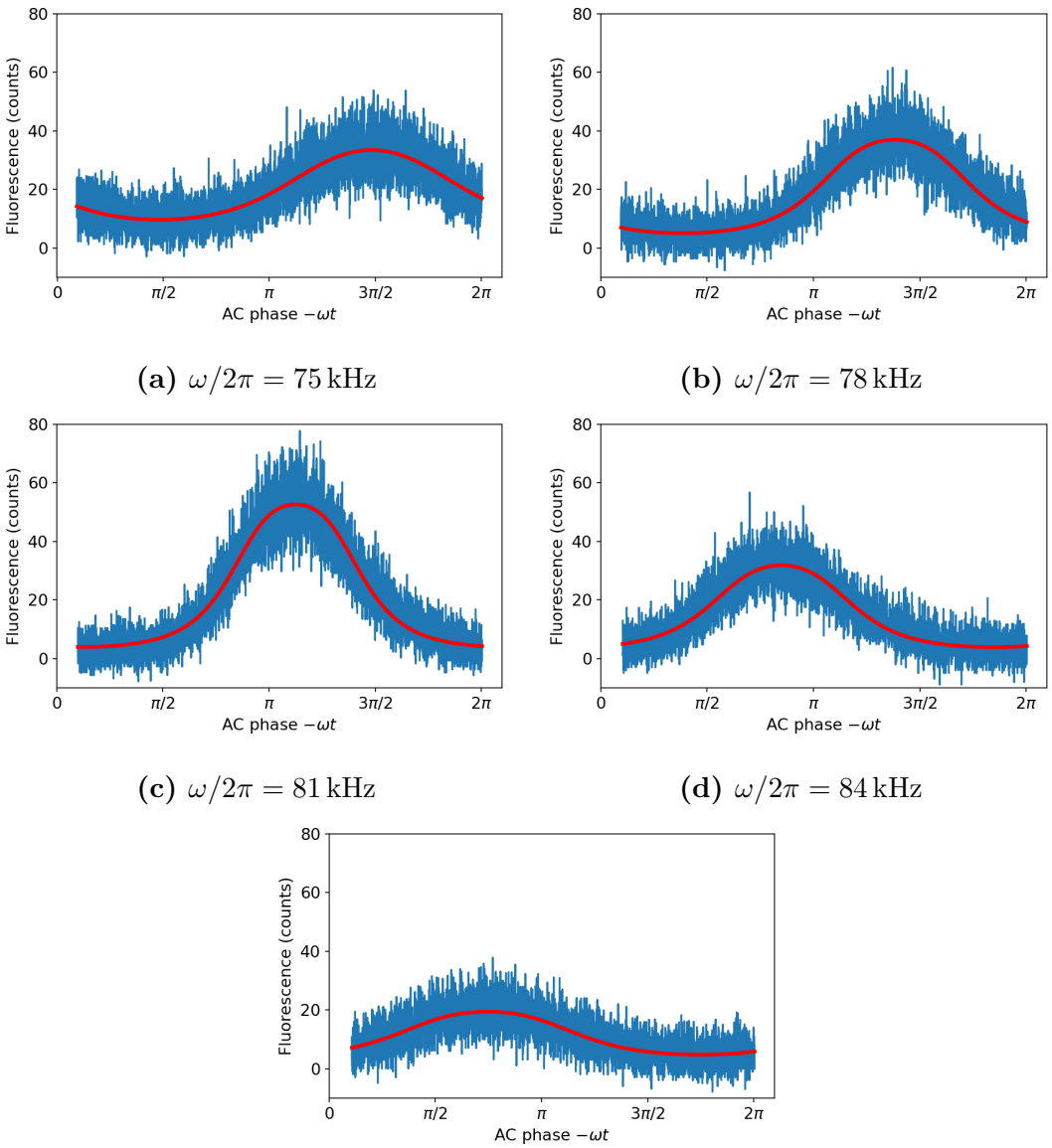

(a) $\omega/2\pi = 75\,\mathrm{kHz}$ **(b)** $\omega/2\pi = 78\,\mathrm{kHz}$

(c) $\omega/2\pi = 81\,\mathrm{kHz}$ **(d)** $\omega/2\pi = 84\,\mathrm{kHz}$

(e) $\omega/2\pi = 87\,\mathrm{kHz}$

Figure 5.5: Measurement of the driven motion of two $^9Be^+$ ions using the photon-correlation method, showing the fluorescence as a function of the phase of the exciting field. The resonance frequency is $\omega_R/2\pi \approx 81\,\mathrm{kHz}$ and the applied amplitude is 200 mV at the AFG. The amplitude of the modulation increases towards the resonance and the phase shifts by π when going from $\omega \ll \omega_R$ to $\omega \gg \omega_R$. The red line describes a fit using Eq. (5.12). The laser parameters are $\delta/2\pi \approx 90\,\mathrm{MHz}$ and $s_0 \approx 10$.

phase is less effected by systematic errors and noise. The phase is derived from the position of the peak, while the amplitude is determined from the height. In Fig. 5.5 the position of the fluorescence maximum is clearly visible, while the height becomes washed out due to low statistics.

Another problem for the amplitude is that only the product $kA(\omega)/\delta$ can be

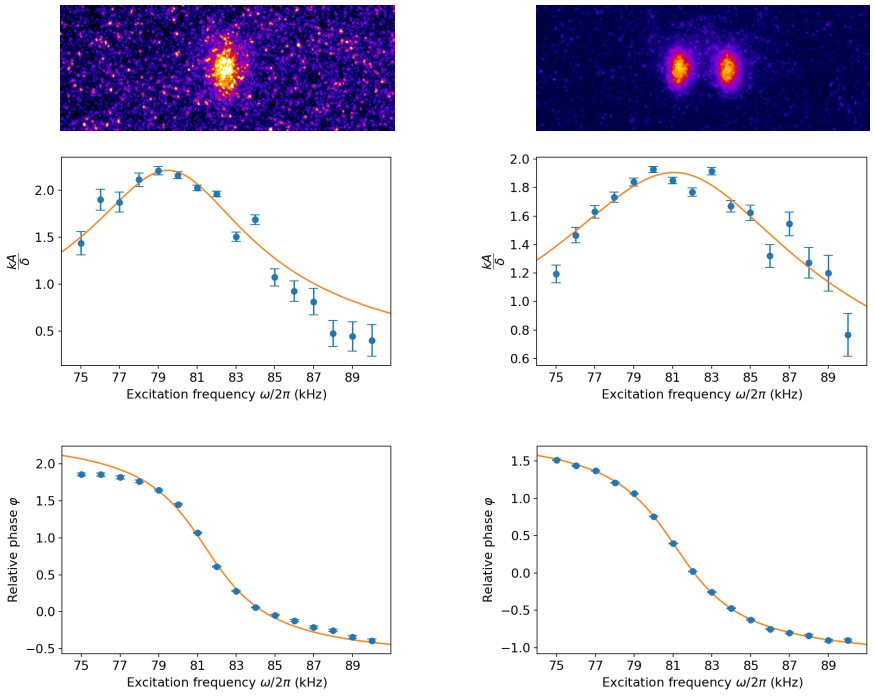

(a) 1 ion **(b)** 2 ions

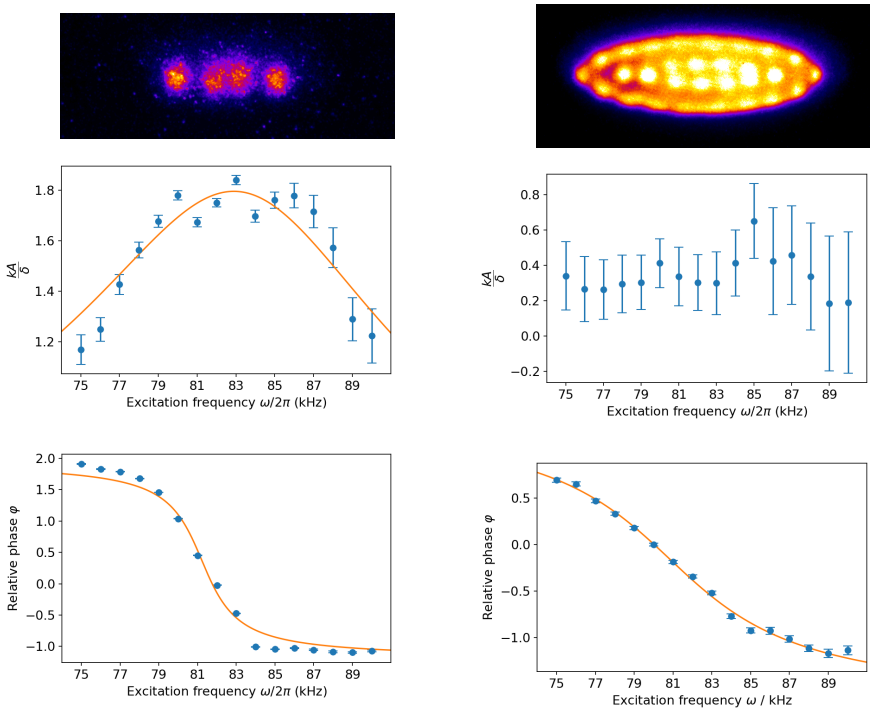

(c) 4 ions **(d)** ≈100 ions

Figure 5.6: Excitation amplitude $kA(\omega)/\delta$ and relative phase $\varphi(\omega)$ between the driving AC field and ion motion as a function of the excitation frequency ω for different numbers of stored ions. The amplitude and the phase are fitted by Eq. (2.54) and Eq. (2.55) respectively. The change in amplitude for ≈ 100 ions is too small and no fit is provided. Together with the measurement data a CCD image of the trapped ions is shown for $\omega \gg \omega_R$ for all configurations a-d.

Table 2: Trap frequencies determined from the driven COM mode.

	$\omega_z/2\pi$ (kHz) from amplitude	$\omega_z/2\pi$ (kHz) from phase
1 Ion	79.7 ± 0.3	81.4 ± 0.1
2 Ions	81.5 ± 0.3	81.16 ± 0.04
4 Ions	83.7 ± 0.5	81.2 ± 0.2
100 Ions	-	81.0 ± 0.2

extracted. Both k and δ are functions of the wavelength, which were assumed to be constant, but fluctuations on the order of 20 MHz are possible due to the accuracy of the wavemeter. For $k = \omega/c$ these fluctuations are negligible, but for $\delta/2\pi \approx 100$ MHz this is not the case.
Therefore, the phase measurement is more accurate and the average of the four data points of the axial trap frequency from the phase is calculated to

$$\bar{\omega}_z = 2\pi \times (81.19 \pm 0.08)\,\text{kHz}. \tag{5.14}$$

The radial trap frequency ω_r can not be measured by this method in the used setup, since the cooling laser and the excited motion are perpendicular to each other, i.e. no modulation due to Doppler shifts occur. It can be implemented by adding a cooling laser in radial direction. The radial trap frequency can then only be estimated using the excitation on the CCD camera, though this often leads to the loss of the ion since no damping from the laser restricts the oscillation amplitude.
Another method to determine ω_r is to use a 3-dimensional crystal and Eq. (2.34), which expresses the ratio of the trap frequencies as a function of the aspect ratio of the crystal. A crystal consisting of ≈ 100 ions was used for the measurement of the COM mode and is again plotted alongside the two projections through the symmetry axes of the crystal in Fig. 5.7. Measuring the radial and axial extension is done by hand at about half height of the outer lying peaks in the projections with an estimated error of 15 pixel. For the axial length $L = (515 \pm 15)$ pixel and for the radial width $R = (165 \pm 15)$ pixel are determined. From this the radial trap frequency is calculated using Eq. (2.34) to be

$$\omega_r = 2\pi \times (169 \pm 2)\,\text{kHz}. \tag{5.15}$$

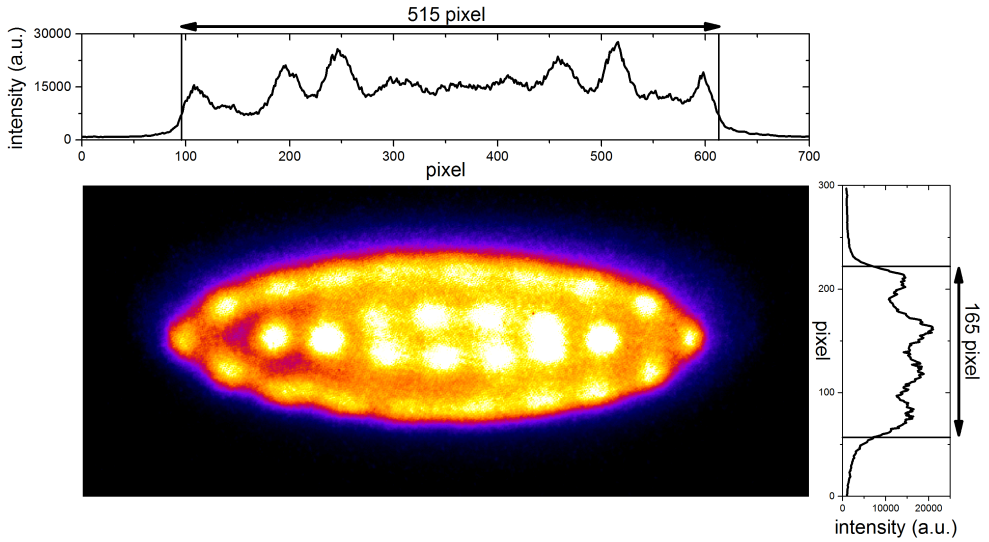

Figure 5.7: CCD image of a Coulomb crystal consisting of ≈ 100 $^9Be^+$ ions. The projections are done along a line through the crystal centre. The vertical lines in the projections indicate from where to where the size of the crystal is measured. The aspect ratio is used to calculate the radial trap frequency given in Eq. (5.15).

5.3 Magnification of the imaging system

The measured axial trap frequency ω_z can be used to calibrate the imaging system. For this CCD images of a crystal consisting of two $^9Be^+$ ions is used, which are projected onto the trap axis and the distance of the ions is measured. This is compared with the theoretical value discussed in Sec. 2.3.1 for the given trap frequency.

The expected distance d between two trapped $^9Be^+$ ions is given by Eq. (2.40):

$$d_{\text{theo}} = 2\sqrt[3]{\frac{Q^2}{16\pi\epsilon_0 m\omega_z^2}} \tag{5.16}$$
$$= (49.14 \pm 0.05)\,\mu\text{m}.$$

10 CCD images of two $^9Be^+$ ions in the Paul trap, each with an exposure time of 10 s, are taken and the intensity in a small region of interest around the ions is projected onto the trap axis. The resulting double peak structure is fitted using the sum of two Gaussian functions, where every data point is weighted with $1/\sqrt{N}$ (N: number of pixel counts). From the fits the peak-peak distance is extracted for each CCD image individually. The error is given by the fitting error of the individual peaks. An example of such a projected CCD image of two ions as well as the distances for all CCD images is shown in Fig. 5.8. The average distance

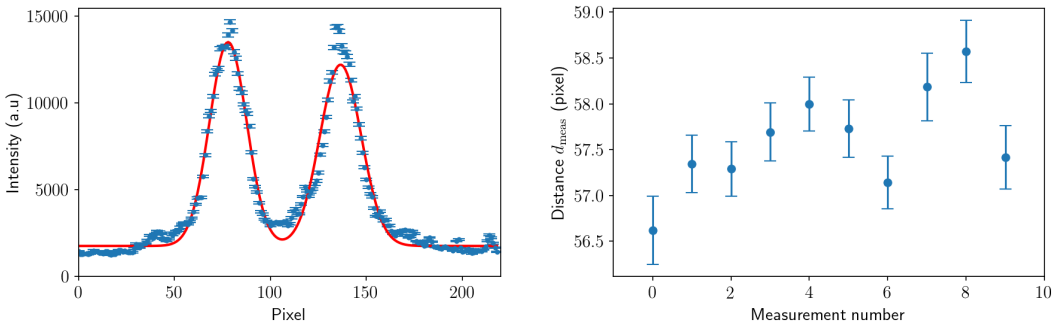

Figure 5.8: Left: Projection of a CCD image of two $^9Be^+$ ions onto the trap axis. The fitting function is given by the sum of two Gaussian functions. **Right:** Measured axial distance d_{meas} between two trapped $^9Be^+$ ions. The distance is given by the peak-peak distance of the two fitted Gaussian functions. The error is given by the fit error of the peaks.

$\bar{d}_{\mathrm{meas}}$ is calculated to be

$$\bar{d}_{\mathrm{meas}} = (57.6 \pm 0.1)\,\mathrm{pixel}, \tag{5.17}$$

where the error is the standard error of the mean. From this the conversion factor

$$\zeta = \frac{d_{\mathrm{theo}}}{\bar{d}_{\mathrm{meas}}} = (0.853 \pm 0.002)\,\mu\mathrm{m\ pixel}^{-1} \tag{5.18}$$

and the magnification

$$M = -\frac{13.5\,\mu\mathrm{m}}{\zeta} = -15.82 \pm 0.03, \tag{5.19}$$

are determined, where it was used that each pixel of the CCD camera has a size of 13.5 µm×13.5 µm.

So far it was neglected that the scattering rates of the the two ions can be different. Scattering photons from the cooling laser adds another constant force as given by Eq. (2.26). For the laser parameters ($s_0 \approx 12$, $\delta/2\pi \approx 100\,\mathrm{MHz}$) the force is estimated to be $F_0 \approx 1 \times 10^{-20}\,\mathrm{N}$. If the same force is acting on both ions, only the central position is shifted in the direction of the laser and the distance is not influenced. However, if the ion further along the laser direction scatters less/more photons the ion distance would decrease/increase.

To estimate the influence of this effect, it is used that the total force acting on

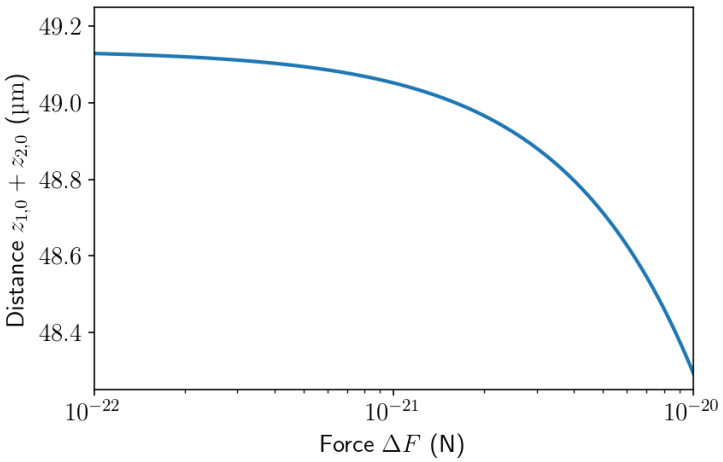

Figure 5.9: Distance $(z_1, 0+z_2, 0)$ between two $^9Be^+$ ions in a harmonic potential with trap frequency $\omega_z/2\pi = 81.19\,\text{kHz}$ as a function of the force difference ΔF due to different photon scattering rates. In the shown case $\Delta F > 0$ the ion upstream the laser scatters more photons and is pushed closer to the second ion, reducing their distance for increasing ΔF.

each of the two ions in equilibrium is zero:

$$m\omega_z^2 z_{1,0} - \frac{Q^2}{4\pi\epsilon_0 m(z_{1,0}+z_{2,0})^2} + F_1 = 0, \tag{5.20}$$

$$-m\omega_z^2 z_{2,0} + \frac{Q^2}{4\pi\epsilon_0 m(z_{1,0}+z_{2,0})^2} + F_2 = 0, \tag{5.21}$$

where F_i accounts for the light force on each ion individually. Subtracting Eq. (5.21) from Eq. (5.20) gives

$$m\omega_z^2(z_{1,0}+z_{2,0}) - \frac{2Q^2}{4\pi\epsilon_0 m(z_{1,0}+z_{2,0})^2} + \Delta F = 0, \tag{5.22}$$

where $\Delta F = F_1 - F_2$. For $\Delta F = 0$ this reproduces Eq. (5.16). Eq. (5.22) can be solved analytically and the distance $z_1 + z_2$ as a function of ΔF is shown in Fig. 5.9.

To estimate the force difference ΔF on the two ions in the trap it is used that the area A_i of the fitted Gaussian functions (see Fig. 5.8) is proportional to the scattering rate. Then the ratio of the areas gives access to the relative force. This ratio is calculated for each of the 10 data points and gives an average $A_1/A_2 = 1.03 \pm 0.07$, with the standard error of the mean. The corresponding force difference is estimated to be

$$\Delta F = (1 - \frac{A_1}{A_2})F_0 \approx 3 \times 10^{-22}\,\text{N}, \tag{5.23}$$

giving a change of the inter ion distance with respect to the case of equal forces $\Delta F = 0$ of about $-0.03\,\mu\text{m}$. This is considerably less than the uncertainty of the measured distance in Eq. (5.17) and is therefore negligible.
Previously the magnification was estimated to be $M = -14.4 \pm 0.5$ by using a glass fibre with a known diameter which was put into the trap centre [20]. From the image on the CCD camera the magnification of the imaging system was inferred. This result differs by $\approx 2.8\sigma$ from the measurement presented in this thesis, which is not significant though it is a large discrepancy. This difference could be explained by the different measurement methods. The new method has the advantage of being independent of a glass fibre, which might introduce uncertainties due to not well known properties like the diameter and how it scatters light. Additionally, the position of the fibre perpendicular to the CCD might not be the same as for trapped ions and can only be judged by whether the fibre and ions are focused when seen on CCD images, which relies on optical comparisons. The new result avoids this by using ions directly.

5.4 Axial excess micromotion

The axial excess micromotion along the trap axis at CryPTEx has previously been measured in [29] with the photon-correlation method described above and showed a velocity amplitude of $v_{\text{max}} = (67 \pm 2)\,\text{m}\,\text{s}^{-1}$ at the trap centre. Such a large micromotion can lead to heating effects and limits the temperature achievable through Doppler cooling [28]. Additionally, it introduces second-order Doppler shifts, which need to be avoided for high precision spectroscopy. For reduction, new Paul trap electronics were built in [29] and are used here for compensation of micromotion. To verify the reduction of axial micromotion it is measured for a single $^9\text{Be}^+$ ion in the trap centre.
Axial excess micromotion can be described to first order as a harmonic motion (see Eq. (2.15)) in phase with the RF voltage used for radial trapping. Therefore, it can be measured with the above described method, using a signal that is synchronized with the RF drive at the frequency $\Omega/2\pi = 4.23\,\text{MHz}$ as a stop signal. Also, it needs to be considered that the cooling laser and the trap axis might not be aligned perfectly and are rotated with respect to each other by an angle θ , which is estimated to be

$$\theta < 0.78^\circ. \tag{5.24}$$

The resulting velocity then consists of the projections of axial and radial micro-

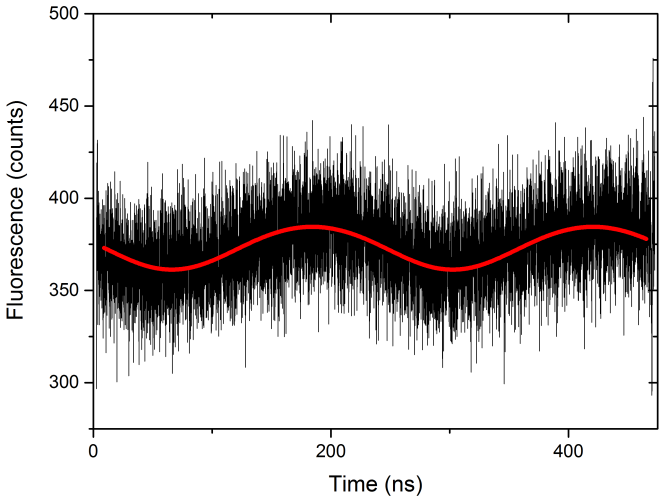

Figure 5.10: Measurement of the micromotion in the trap centre. The fit function is given by Eq. (5.2). Micromotion causes modulation of ≈ 10 counts on top of the constant background at ≈ 380 counts.

motion, where the radial component is

$$v_{\text{radial}}^{\text{Proj}} = \cos(\theta) v_{\text{radial}} < 1.4\,\%\ v_{\text{radial}}. \tag{5.25}$$

Therefore, the result gives only an upper amplitude for the axial micromotion. One could also implement radial cooling additionally to axial cooling, to reduce radial micromotion, though this would also produce a signal from the additional laser.

A frequency divider for the stop signal coming from the AFG is used, in order to measure two periods instead of one, since $2(2\pi/\Omega) \approx 473\,\text{ns} < t_{\text{MM}}$. The complete measurement consists of recording the fluorescence for 1 min and measuring the background for several minutes directly afterwards. The measurement time of 1 min is chosen to reduce wavelength drifts, which are given by drifts from the wavemeter. The data is corrected for counting characteristics of the different ADC channels (see Sec. 5.1.2) and the average background is subtracted. An example for the acquired data is shown in Fig. 5.10. It can be seen that the micromotion is small since the modulation amplitude is ≈ 10 counts for a signal of ≈ 380 counts. Performing a least-square fit of the time-dependent fluorescence from Eq. (5.2) gives $kv/\delta = (0.2 \pm 0.1)$.

It remains to determine the absolute detuning. Previously in [29] this has been done, by measuring the micromotion at different relative detunings, which can be done with the wavelength meter if the detuning is sufficiently large. The resulting change can be fitted and the absolute detuning extracted. Here this is not possible as the axial micromotion is too small.

The modulation is $\propto 1/\delta$ as can be seen in Eq. (5.2), i.e. a smaller detuning yields a larger modulation. For typically $\Gamma_{\text{eff}}/2\pi \approx 60\,\text{MHz}$, it is found that $\delta/2\pi < 20\,\text{MHz}$ is required to see any signal that could be fitted so that the uncertainties do not exceed the fitted values by far. Knowledge of the cooling lasers frequency is limited by the absolute accuracy of 10 MHz of the wavelength meter [50], since frequency stabilization is done using it. This makes a measurement at different detunings impossible.
To estimate the velocity a frequency-stabilized Helium-Neon laser is used with drifts $< 2\,\text{MHz}\,\text{h}^{-1}$ [51] as a reference. Resonance is found by changing the set point of the wavelength meter and observing the ion on the CCD camera. The detuning is measured as the distance from resonance, giving for the measurement shown in Fig. 5.10 $\delta/2\pi = (10 \pm 20)\,\text{MHz}$. Note that the error is twice the wavelength meter accuracy, since it is stabilized at 626 nm rather than 313 nm. The resulting peak velocity is then

$$v_{\text{max}} = (0.6 \pm 1.2)\,\text{m}\,\text{s}^{-1}. \tag{5.26}$$

This is considerably lower than the previously measured value of $v_{\text{max}} \approx (67 \pm 2)\,\text{m}\,\text{s}^{-1}$, which was achieved through compensation of the micromotion with the new coupling box built in [29].
To assess the result given in Eq. (5.26) it is looked at in a typical experimental situation with $s_0 \approx 10$ and $\Gamma_{\text{eff}}/2\pi \approx 65\,\text{MHz}$. To achieve the Doppler limit $\delta = \Gamma_{\text{eff}}/2$ is set. For micromotion to be insignificant, its modulation of the fluorescence needs to be small, i.e.

$$\frac{kv}{\delta} = \frac{2kv}{\Gamma_{\text{eff}}} \ll 1. \tag{5.27}$$

This is equivalent to

$$v \ll \frac{\Gamma_{\text{eff}}}{2k} \approx 10\,\text{m}\,\text{s}^{-1}. \tag{5.28}$$

For the given value in Eq. (5.26) this is satisfied to a decent degree. This indicates that the temperature through Doppler cooling is not limited by micromotion, though the large error needs to be taken into account. The result is mostly limited by the wavelength stability and accuracy given by the wavemeter. A higher accuracy would allow for a better determination of δ, which is currently the largest error source. A higher stability would allow for longer measurement times, which on the one hand reduces the statistical uncertainty. On the other hand it would allow for measurements at high detunings reducing the relative error of the detuning, where long measurement times are required due to a low

signal to noise ratio.
This measurement technique can also be used for CryPTEx II, where a small micromotion is a necessity, since quantum logic spectroscopy (QLS) [27] is intended. Firstly, to enable sufficiently low temperatures close to the Doppler limit to make resolved-sideband cooling [35] possible. Secondly, it can limit the precision of spectroscopy by inducing a second-order Doppler shift, which sometimes is the largest uncertainty in optical clocks [10, 12].

Chapter 6

CryPTEx II

CryPTEx II is the successor experiment of CryPTEx and was designed to improve the mechanical stability of the trap environment as well as the stability of the overall trapping conditions. At CryPTEx, vibrations caused by the pulse tube are directly transported to the trap through their semi-rigid connection. This is undesirable for high precision measurements, since motion of the trap relative to the laser systems leads to systematic shifts. Therefore, a vibrationally decoupled cryogenic supply system was designed by Maria Schwarz and Julian Stark. The system was built in collaboration with the group of Piet O. Schmidt at the Physikalisch Technische Bundesanstalt in Braunschweig. A twin setup of the cryogenic system is currently in operation in Braunschweig.
Additionally, a superconductive Paul trap was designed [29] to reach a high stability of the RF trapping potential and allow for longtime storage of HCI. This trap will have a radial trap frequency of $\omega_r/2\pi \approx 4\,\mathrm{MHz}$ and an axial trap frequency of $\omega_z/2\pi \approx 2\,\mathrm{MHz}$ at $U_{\mathrm{DC}} = 100\,\mathrm{V}$ which allows for resolved-sideband Raman cooling, currently impossible at CryPTEx due to the low trap frequencies ($\omega_{z/r}/2\pi \approx 100\,\mathrm{kHz}$). The RF resonator will not be discussed here, since it is still under construction by the end of this thesis. CryPTEx II was partly assembled during the scope of this thesis. The setup of the cryogenic system and the results of its first cool down are presented in this chapter.

6.1 The cryogenic supply

Every system held at a reduced temperature with respect to its environment will be subject to different heating mechanisms. Even when put into ultra high vacuum, where convection becomes negligible, blackbody radiation as well as thermal conduction through any mechanical connections to the environment can heat up the system considerably. These effects need to be minimized to make it

Table 3: Estimated heat load of the two temperature stages through blackbody radiation and through the spokes. A detailed list for the spokes is given Tab. 4. Source [52].

	Blackbody radiation (W)	Spokes (W)
4 K stage	0.01	0.08
40 K stage	13.5	1.91
4 K total	**13.5**	**1.99**

possible to cool the trap region to cryogenic temperatures. In the following these effects will be discussed shortly and it will be explained how they are minimized at CryPTEx II.

Any body with a temperature $T > 0\,\mathrm{K}$ emits thermal radiation where the spectrum is depending on T. This is called blackbody radiation and the emitted power Q_{BB} is described by the Stefan-Boltzmann law:

$$Q_{\mathrm{BB}} = \epsilon \sigma A T^4, \tag{6.1}$$

where σ is the Stefan-Boltzmann constant, A is the surface area and ϵ describes the emissivity of the body. $\epsilon = 1$ represents an ideal black body, while for real materials $\epsilon < 1$ holds. By reducing the temperature of the body, the radiated power can be reduced strongly, since $Q_{\mathrm{BB}} \propto T^4$. For this reason the cryogenic system has two temperature stages. The first stage at 40 K works as a heat shield to protect the inner 4 K stage from thermal radiation from the vacuum chamber at room temperature and almost completely surrounds the 4 K stage. This almost entirely eliminates the heating of the 4 K stage due to blackbody radiation. The exception are optical ports for injection of lasers and ion sources to the Paul trap, which allow for blackbody radiation from 300 K to reach the 4 K stage. The estimated heat inflow through blackbody radiation for both temperature stages is given in Tab. 3, which shows that the heat input to the 4 K stage is three orders of magnitude smaller than the heat load onto the 40 K stage.

The second relevant heating effect is the heat flow Q_{con} between two objects at temperature T_1 and T_2 which are connected by a link with uniform cross section A_{cs} and length l. This is described by

$$Q_{\mathrm{con}} = \frac{A_{\mathrm{cs}}}{l} \int_{T_1}^{T_2} \lambda_{\mathrm{t}}(T) \mathrm{d}T. \tag{6.2}$$

The function $\lambda_{\mathrm{t}}(T)$ is the thermal conductivity of the connection and depends on

Table 4: Heat inflow through the stainless steel spokes used for the mechanical mounting of the temperature stages for the different parts. The total heat input for each temperature stage is also given. Source [52].

Location	Amount	Length (cm)	Heat (W)
Pendulum 300 K - 40 K	2	15	0.49
Below trap 300 K - 40 K	12	12	0.92
Trap 300 K - 40 K	12	22	0.50
Total 300 K - 40 K	**26**		**1.91**
Pendulum 40 K - 4 K	6	9.7	0.017
Below trap 40 K - 4 K	6	4.3	0.038
Trap 40 K - 4 K	12	17	0.020
Total 40 K - 4 K	**26**		**0.075**

the material and the temperature. Eq. (6.2) has two implications for the design of a cryogenic system. Firstly, mechanical connections to mount the 40 K stage in the vacuum chamber and the 4 K stage in the 40 K stage should be long and have a small cross sectional area to limit the heat flow. Additionally, a suitable material with low thermal conductivity and high mechanical stability needs to be chosen. For CryPTEx II, these requirements are fulfilled by using spokes with typically $l \approx 15\,\mathrm{cm}$ and $A_{\mathrm{cs}} \approx 3.14\,\mathrm{mm}^2$ made of stainless steel, which has a low thermal conductivity while providing sufficient stability. The estimated thermal conductivity through the spokes is given in detail in Tab. 4. For the 40 K stage blackbody radiation is the dominant heating effect, while for the 4 K stage it is significantly smaller than the heat coming through the spokes (see Tab. 3).
Secondly, Eq. (6.2) has consequences for the thermal links between the pulse tube cooler and the Paul trap, which should transport the heat efficiently to achieve a low trap temperature. For these parts a high cross sectional area and a material with a high thermal conductivity is desirable. For CryPTEx II, these parts are made of highly pure annealed copper ($> 99.995\,\%$ purity) and are designed to have a thermal resistance below $0.3\,\mathrm{K\,W^{-1}}$ for all individual parts. The estimated values for the thermal resistance of all parts connecting the pulse tube cryocooler to the Paul trap are given for both temperatures stages in Tab. 5.
As for CryPTEx, the cooling power is produced by a commercial pulse tube cryocooler with a pumping frequency of about 1 Hz providing a cooling power of 40 W at 40 K and 1 W at 4 K. An overview of the cryogenic setup is shown in Fig. 6.1. It consists of a pulse tube connected through flexible copper links to the so called pendulum which is connected through another set of flexible copper

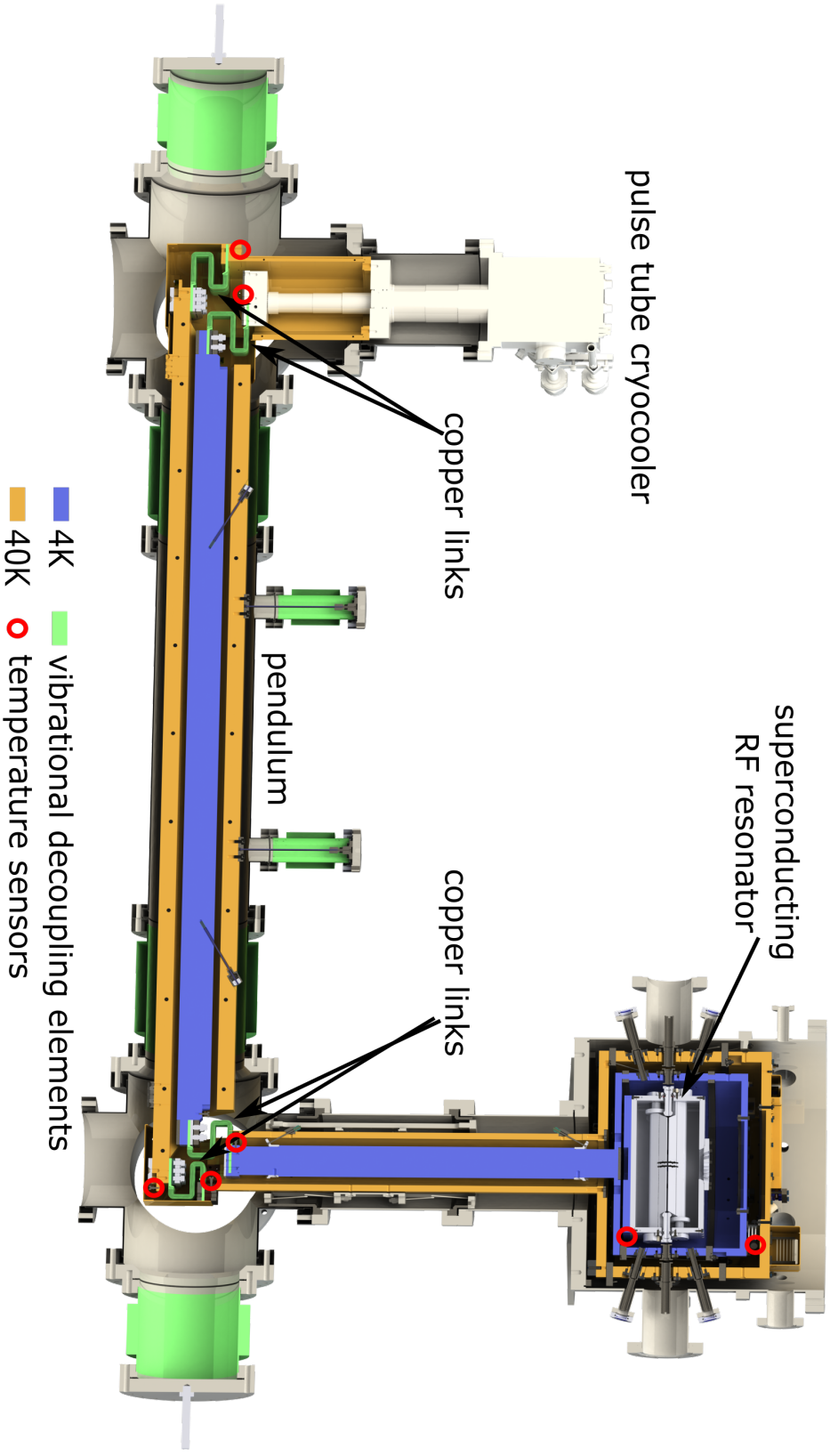

Figure 6.1: CAD rendering of the setup of CryPTEx II. For explanations see Sec. 6.1. Source [52].

Table 5: Estimated thermal resistance of the copper parts of the cryogenic system connecting the pulse tube to the trap environment. The used values for the material specific thermal conductivity is taken at the temperature of the two stages, i.e. 4 K and 40 K respectively. The differences in thermal conductivity for parts at the same temperature is caused by different purities of the used copper. Source [52].

Location	Thermal conductivity λ_t of the material ($W\,cm^{-1}\,K^{-1}$)	Thermal resistance of the parts ($K\,W^{-1}$)
4 K pulse tube links	70	0.16
4 K pendulum	30	0.22
4 K trap links	70	0.14
4 K below trap	30	0.10
40 K under pulse tube	20	0.03
40 K pulse tube links	20	0.29
40 K pendulum	17	0.11
40 K trap links	20	0.21
40 K below trap	20	0.02

links to a vertical assembly connected directly to the trap chamber. This makes thermalisation alongside vibrational decoupling of the pulse tube and the trap environment possible. The length of the complete setup permits to put pulse tube and the required compressor in a machine room, while Paul trap and laser systems are placed in a separate room. This will suppress the acoustical noise at the Paul trap from vacuum pumps, compressor and pulse tube.
The central part of the cryogenic supply system is the horizontal pendulum (see Fig. 6.1). It is suspended from two spokes attached to the top of the surrounding vacuum chamber. The 40 K stage is made up of of eight trapezoidal bars, which

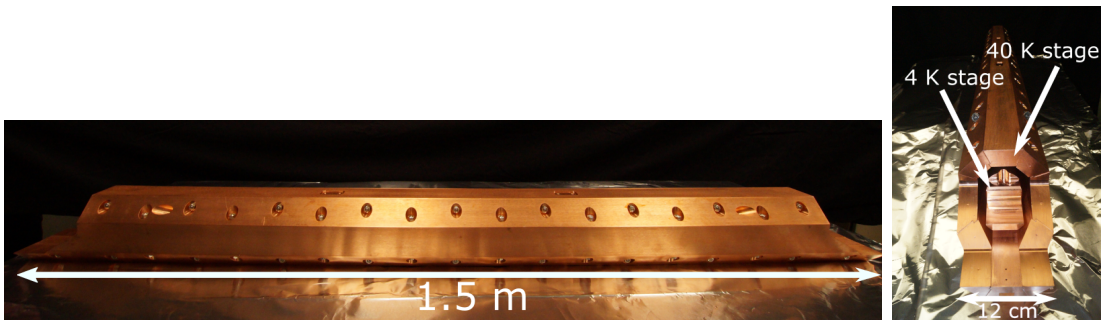

Figure 6.2: Side view (left picture) and front view (right picture) of the pendulum made of highly pure copper. Source [52].

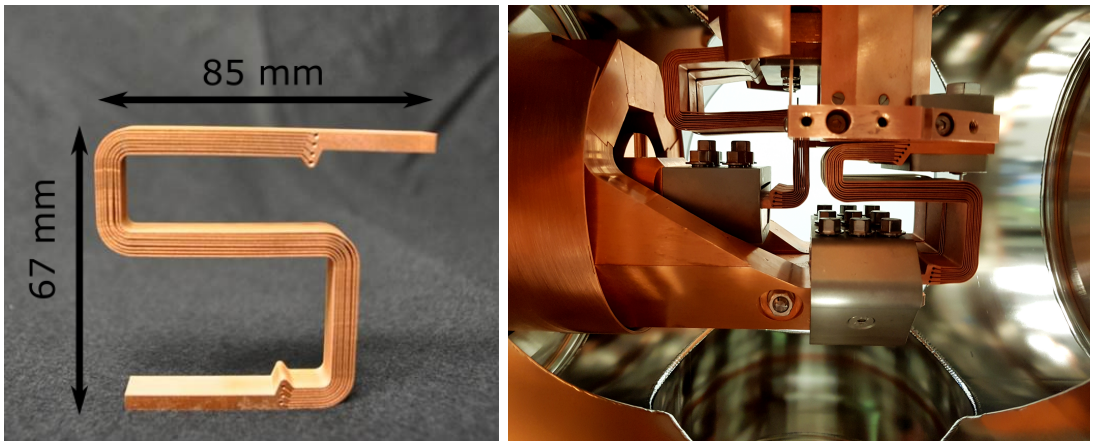

Figure 6.3: Left: Copper link for connection of the pendulum to the vertical parts. They were specifically designed for vibrational decoupling while maintaining a good thermal connection. **Right:** Copper links installed under the Paul trap chamber. Three links per temperature stage are used. Source [52].

are held together by stainless steel screws, forming a hollow tube. Inside, the 4 K stage consisting of a massive copper rod is mounted with six spokes. A side view as well as a front view of the pendulum is shown in Fig. 6.2.
The pendulum is connected to the pulse tube and to the vertical part leading to the trap chamber through the flexible copper links shown in Fig. 6.3. These were specifically designed to provide a high mechanical flexibility for vibrational decoupling, while maintaining a cross section area as large as possible to reduce the thermal resistance (see Eq. (6.2)). The links are machined from highly pure copper (99.999 %) and were annealed at 800 °C. At each temperature stage three links are installed per side. A picture of the links connecting pendulum and vertical part attached to the trap chamber is shown in Fig. 6.3.
The heat shields for the trap chamber are cylindrical with an inner diameter of 269 mm and a height of 165 mm for the 4 K stage. They are shown in Fig. 6.4 without the top cover. Additionally to being made of highly pure copper, the heat shields were first silver- and then gold-plated with a layer thickness of 10 µm and 0.5 µm respectively. The gold prevents oxidation of the copper and has a low emittance ϵ while the silver is needed to prevent diffusion of gold into the copper. The 4 K stage is fixed to the 40 K stage through 12 spokes and the 40 K is mounted to the vacuum chamber through 12 spokes. Optical access to the centre of the Paul trap is granted through 12 ports with an angle of 30° in between them as shown in Fig. 6.4. The holes in the 4 K and 40 K heat shields are extended using tubes, to reduce the thermal load onto the 4 K stage by blackbody radiation through the ports by reducing the solid angle. Imaging of the trapped ions is possible through a small optical access in the top cover.

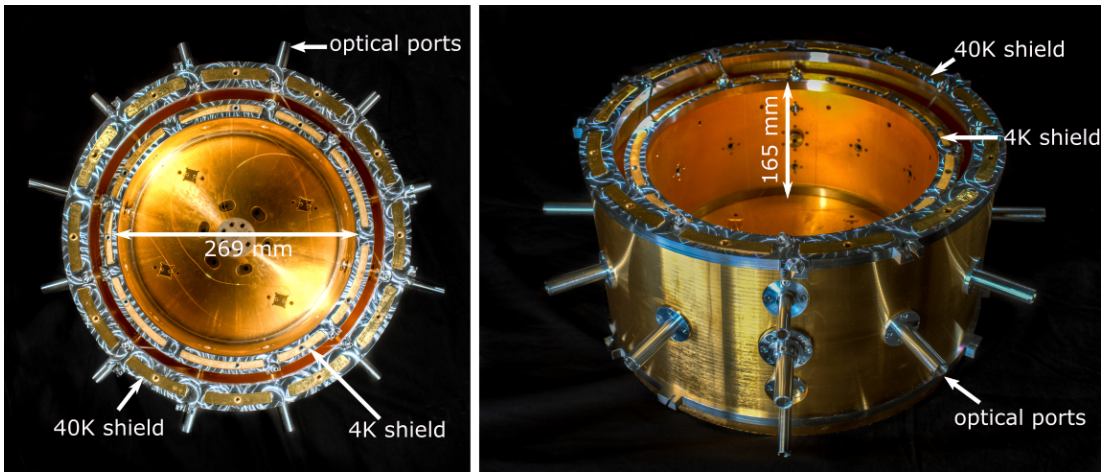

Figure 6.4: Top (left picture) and side view (right picture) of the heat shields for the trap chamber without the top cover. They are gold-plated to prevent oxidation of the copper and for the low emissivity ϵ of gold. The optical ports in the 4 K and 40 K heat shields are extended to reduce the solid angle at which blackbody radiation from 300 K can enter the 4 K heat shield. Pictures made by Christian Föhr.

6.2 Cooling down

A first cool down of the complete cryogenic system without Paul trap and cabling was performed with a base pressure at room temperature of $\approx 1\times10^{-7}$ mbar before the pulse tube cryocooler was turned on. Seven temperature sensors are installed to measure the temperature gradients in the setup: three on the 4 K stage and four on the 40 K stage. Their positions are shown in Fig. 6.1. They are typically located before and after the copper links, to precisely measure the temperature gradient over those. The temperature was measured as a function of time and is shown in Fig. 6.5. It took $\approx$ 200 h to a reach the steady-state temperature for all sensors. At the 4 K trap chamber heat shield, which will later surround and thermalise with the trap, the final temperature was 4.23 K with an uncertainty of 5 mK [53]. This is sufficiently low to allow for superconducting operation of the intended RF-resonator [29] made of Nb [54].

At the beginning of the cool down, the temperatures on the pulse tube fell much faster compared to the other locations as can be seen in Fig. 6.5. This is to be expected due to the limited thermal conductivity of copper at 300 K. As the temperature falls, the thermal conductivity increases, which can be seen in particular on the 4 K sensors, showing an increasingly faster reduction in temperature over time. Once the temperature on the 4 K stage reaches $\approx$ 25 K, a sharp decrease on all 4 K temperatures can be seen, which is related to a highly increased heat flow, further reducing the temperature and accelerating this effect. A maximum

thermal conductivity is reached at $\approx 20\,\mathrm{K}$. After that, it decreases again and at $\approx 5\,\mathrm{K}$ the sharp decrease stops and only slow thermalisation is observed. It took an additional $\approx 150\,\mathrm{h}$ for full thermalisation. The sudden increase in thermal conductivity of the 4 K stage after 54 h also leads to a short spike in the temperature of the 40 K pulse tube stage. This is attributed to the sudden heat flow coming from the 4 K stage.

A residual temperature gradient between the different copper parts according to their thermal resistance remains. The temperature gradient for the 40 K stage showed an increase from pulse tube at 30 K to trap chamber at 61 K. The temperature increase over each set of links is approximately the same for pulse tube and trap side, indicating a similar thermal connection on both sides. Before the installation of the trap chamber, a previous cool down showed only a increase of $\approx 3\,\mathrm{K}$ over each set of copper links at the 40 K stage and overall only a small temperature gradient over the complete system of $\approx 7\,\mathrm{K}$. To explain the differences, further investigations are required.

The steady-state temperature measured in the trap chamber is 0.2 K lower than the temperature measured below the trap. This is unexpected but might be explained by the way the sensors are installed. The sensor in the trap chamber is fully surrounded by parts at 4 K, while the sensor below the trap has is surrounded by the 40 K stage. The inflowing heat through blackbody radiation might heat the sensor slightly, resulting in a higher measured temperature. Overall, the temperature gradient at 4 K from the pulse tube to the trap chamber is only 0.2 K over a distance of 1.7 m, which is an excellent result. The temperature at the trap chamber might even be reduced slightly, if the temperature of the 40 K shield can be reduced further.

The pressure at 300 K was measured during the cool down and is shown in Fig. 6.5. When going to cryogenic temperatures residual gas in the vacuum chamber freezes to the cryogenic surfaces, reducing the pressure. It decreased from the initial $\approx 1 \times 10^{-7}\,\mathrm{mbar}$ to $\approx 2 \times 10^{-9}\,\mathrm{mbar}$ at the end of the measurement, though it was still falling. A lower pressure is expected to be achievable by pumping longer before starting to cool down and by replacing the Viton gasket of the CF400 trap chamber with a copper gasket. Inside the 4 K trap chamber only H_2 does not condense and the pressure is correspondingly expected to be much lower [44].

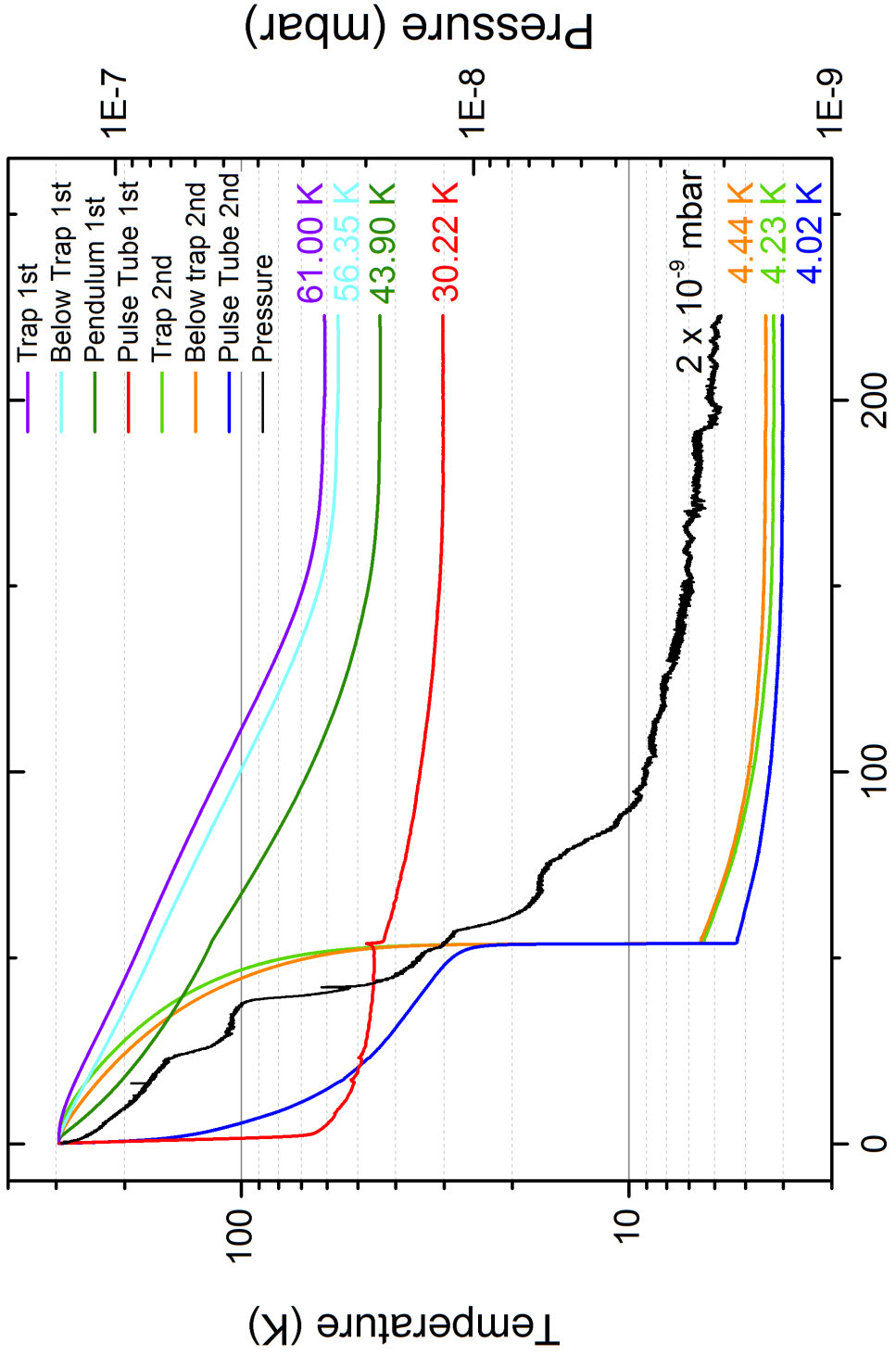

Figure 6.5: First cool down of the cryogenic supply system for CryPTEx II. "1st" refers to the 40 K stage and "2nd" refers to the 4 K stage. The uncertainty of the 4 K sensors is < 5 mK and the uncertainty of the 40 K sensors is < 40 mK [53]. For explanations see Sec. 6.2.

Chapter 7

Summary and outlook

This thesis paved the way for the start-up of CryPTEx II. The first part consists of measurements of the trapping potentials performed at CryPTEx using a photon-correlation technique, which is also applicable to CryPTEx II. This allows for the determination of the trap frequencies and micromotion as well as the magnification of the imaging system. In particular, a suppressed excess micromotion is measured, which is an essential prerequisite for ground state cooling. In the second part of this thesis, the cryogenic system for CryPTEx II was partly assembled and the first cool down measurement was performed, showing good results.

The axial trap frequency at CryPTEx was determined using the COM mode of different numbers of $^9Be^+$ ions giving $\omega_z = (81.19 \pm 0.08)\,\mathrm{kHz}$. For this, the trapped ions were driven by an external AC field and the modulated scattering rate of photons from the cooling laser was measured. Especially the relative phase between the driving field and the ion's motion were in very good agreement with the ideal driven harmonic oscillator. This allowed for accurate measurement of the trap frequency with very small regards to systematic errors compared to a determination via the CCD camera, where also the incoherent motion of the ion in measured. The magnification of the imaging system was inferred from CCD camera images of two trapped $^9Be^+$ ions and the measured trap frequency giving $M = -15.82 \pm 0.03$. This method to determine the magnification reduced the uncertainty by one order of magnitude compared to a previous measurement [20], which deviated from this new result by $\approx 2.8\sigma$.

Axial excess micromotion was measured and compared to a previous result [29]. It showed a current peak velocity of $v_{\mathrm{max}} = (0.6 \pm 1.2)\,\mathrm{m\,s^{-1}}$, which is ≈ 100 smaller than a previous measurement [29]. The reduction was achieved by use of a new Paul trap electronics built in [29]. The precision in the determination of the peak velocity is limited by the wavelength accuracy and stability of the wavelength

meter used for frequency stabilization of the cooling laser. This introduces large uncertainties and limits the measurement time due to frequency fluctuations. To improve this another way of wavelength stabilization needs to be employed. This greatly reduced axial excess micromotion is sufficiently small to not cause significant heating effects counteracting Doppler cooling. Micromotion also causes a second-order Doppler shift, limiting the precision of high precision spectroscopy. In the last chapter, the cryogenic supply of the successor experiment CryPTEx II is described, which was partly assembled during this thesis. It is designed to allow for small thermal gradient while vibrationally decoupling pulse tube and Paul trap. The first cool down of the whole system showed promising results where a temperature of 4.23 K was achieved for the trap environment. This is sufficiently low to make superconducting operation of the intended RF resonator [29] made of Nb possible, which will be used to trap HCI in ultra-stable RF potentials. It will also permit sideband-cooling due to the much higher trap frequencies compared to CryPTEx. The resonator is currently being assembled in the workshop of the Max Planck Institute for Nuclear Physics.
The long term goal for CryPTEx II is Quantum logic spectroscopy (QLS) [27]. It has been shown that a single $^{9}Be^{+}$ ion is sufficient to sympathetically cool one HCI [18], making QLS possible. Ground state cooling needs to be performed before QLS can be employed and is the next required step. At CryPTEx this is not possible, as a result of too low trap frequencies. CryPTEx II is expected to achieve sufficiently high trap frequencies so that resolved-sideband Raman cooling is possible. For this, a cooling scheme needs to be developed and a second 313 nm laser, similar to the current one used for Doppler cooling, is required. The first candidate for QLS is Ar^{+13}, since it possesses a transition at 441 nm and was previously measured [55]. A spectroscopy laser for this wavelength range is available in the laboratories of CryPTEx [56]. Also the search for other candidates, accessible with the existing laser, are under investigation using electron beam ion traps.

Bibliography

[1] P. J. Mohr, D. B. Newell, and B. N. Taylor, "CODATA Recommended Values of the Fundamental Physical Constants: 2014," July 2015. Online; accessed 18.09.2018.

[2] J.-P. Uzan, "The fundamental constants and their variation: observational and theoretical status," *Reviews of Modern Phyiscs*, vol. 75, pp. 403–455, Apr 2003.

[3] P. A. M. Dirac, "The Cosmological Constants," *Nature*, vol. 139, no. 3512, pp. 323–323, 1937.

[4] P. A. M. Dirac, "A New Basis for Cosmology," *Proceedings of the Royal Society of London A: Mathematical, Physical and Engineering Sciences*, vol. 165, no. 921, pp. 199–208, 1938.

[5] T. Chiba, "The Constancy of the Constants of Nature: Updates," *Progress of Theoretical Physics*, vol. 126, no. 6, pp. 993–1019, 2011.

[6] J. K. Webb, J. A. King, M. T. Murphy, V. V. Flambaum, R. F. Carswell, and M. B. Bainbridge, "Indications of a Spatial Variation of the Fine Structure Constant," *Phys. Rev. Lett.*, vol. 107, p. 191101, Oct 2011.

[7] J. C. Berengut and V. V. Flambaum, "Manifestations of a spatial variation of fundamental constants in atomic and nuclear clocks, Oklo, meteorites, and cosmological phenomena," *Europhysics Letters*, vol. 97, no. 2, p. 20006, 2012.

[8] V. A. Dzuba, V. V. Flambaum, and M. V. Marchenko, "Relativistic effects in Sr, Dy, Yb II, and Yb III and search for variation of the fine-structure constant," *Phys. Rev. A*, vol. 68, p. 022506, Aug 2003.

[9] V. Dzuba and V. Flambaum, "Atomic calculations and search for variation of the fine structure constant in quasar absorption spectra," *Canadian Journal of Physics*, vol. 87, 06 2008.

[10] N. Huntemann, C. Sanner, B. Lipphardt, C. Tamm, and E. Peik, "Single-Ion Atomic Clock with 3×10^{-18} systematic uncertainty," *Phys. Rev. Lett.*, vol. 116, p. 063001, Feb 2016.

[11] T. L. Nicholson, S. L. Campbell, R. B. Hutson, G. E. Marti, B. J. Bloom, R. L. McNally, W. Zhang, M. D. Barrett, M. S. Safronova, G. F. Strouse, W. L. Tew, and J. Ye, "Systematic evaluation of an atomic clock at 2 x 10-18 total uncertainty," *Nature Communications*, vol. 6, p. 6896, 2015-04 2015.

[12] C. W. Chou, D. B. Hume, J. C. J. Koelemeij, D. J. Wineland, and T. Rosenband, "Frequency Comparison of Two High-Accuracy Al^+ Optical Clocks," *Phys. Rev. Lett.*, vol. 104, p. 070802, Feb 2010.

[13] T. Rosenband, D. B. Hume, P. O. Schmidt, C. W. , A. Brusch, L. Lorini, W. H. Oskay, R. E. Drullinger, T. M. Fortier, J. E. Stalnaker, S. A. Diddams, W. C. Swann, N. R. Newbury, W. M. Itano, D. J. Wineland, and J. C. Bergquist, "Frequency Ratio of Al+ and Hg+ Single-Ion Optical Clocks; Metrology at the 17th Decimal Place," *Science*, vol. 319, no. 5871, pp. 1808–1812, 2008.

[14] J. C. Berengut, V. A. Dzuba, V. V. Flambaum, and A. Ong, "Electron-Hole Transitions in Multiply Charged Ions for Precision Laser Spectroscopy and Searching for Variations in α," *Phys. Rev. Lett.*, vol. 106, p. 210802, May 2011.

[15] V. A. Dzuba, V. V. Flambaum, and J. K. Webb, "Calculations of the relativistic effects in many-electron atoms and space-time variation of fundamental constants," *Physical Review A*, vol. 59, no. 1, pp. 230–237, 1999.

[16] M. S. Safronova, V. A. Dzuba, V. V. Flambaum, U. I. Safronova, S. G. Porsev, and M. G. Kozlov, "Highly Charged Ions for Atomic Clocks, Quantum Information, and Search for α variation," *Phys. Rev. Lett.*, vol. 113, p. 030801, Jul 2014.

[17] M. Schwarz, O. O. Versolato, A. Windberger, F. R. Brunner, T. Ballance, S. N. Eberle, J. Ullrich, P. O. Schmidt, A. K. Hansen, A. D. Gingell, M. Drewsen, and J. R. C. López-Urrutia, "Cryogenic linear Paul trap for cold highly charged ion experiments," *Review of Scientific Instruments*, vol. 83, no. 8, p. 083115, 2012.

[18] L. Schmöger, O. O. Versolato, M. Schwarz, M. Kohnen, A. Windberger, B. Piest, S. Feuchtenbeiner, J. Pedregosa-Gutierrez, T. Leopold, P. Micke,

A. K. Hansen, T. M. Baumann, M. Drewsen, J. Ullrich, P. O. Schmidt, and J. R. C. López-Urrutia, "Coulomb crystallization of highly charged ions," *Science*, vol. 347, no. 6227, pp. 1233–1236, 2015.

[19] L. Schmöger, M. Schwarz, T. M. Baumann, O. O. Versolato, B. Piest, T. Pfeifer, J. Ullrich, P. O. Schmidt, and J. R. Crespo López-Urrutia, "Deceleration, precooling, and multi-pass stopping of highly charged ions in Be+ Coulomb crystals," *Review of Scientific Instruments*, vol. 86, no. 10, p. 103111, 2015.

[20] L. Schmöger, *Kalte hochgeladene Ionen für Frequenzmetrologie*. PhD thesis, Heidelberg University, 6 2017.

[21] M. G. Kozlov, M. S. Safronova, J. R. Crespo López-Urrutia, and P. O. Schmidt, "Highly charged ions: optical clocks and applications in fundamental physics," *Reviews of Modern Phyiscs*, 2018. Accepted.

[22] T. Pruttivarasin, M. Ramm, S. G. Porsev, I. I. Tupitsyn, M. S. Safronova, M. A. Hohensee, and H. Häffner, "Michelson-Morley analogue for electrons using trapped ions to test Lorentz symmetry," *Nature*, vol. 517, Jan 2015.

[23] R. Shaniv, R. Ozeri, M. S. Safronova, S. G. Porsev, V. A. Dzuba, V. V. Flambaum, and H. Häffner, "New Methods for Testing Lorentz Invariance with Atomic Systems," *Phys. Rev. Lett.*, vol. 120, p. 103202, Mar 2018.

[24] C. Gohle, T. Udem, M. Herrmann, J. Rauschenberger, R. Holzwarth, H. A. Schuessler, F. Krausz, and T. W. Hänsch, "A frequency comb in the extreme ultraviolet," *Nature*, vol. 436, pp. 234 EP –, Jul 2005.

[25] C. Benko, T. K. Allison, A. Cingöz, L. Hua, F. Labaye, D. C. Yost, and J. Ye, "Extreme ultraviolet radiation with coherence time greater than 1 s," *Nature Photonics*, vol. 8, Jun 2014. Article.

[26] A. Derevianko, V. A. Dzuba, and V. V. Flambaum, "Highly Charged Ions as a Basis of Optical Atomic Clockwork of Exceptional Accuracy," *Phys. Rev. Lett.*, vol. 109, p. 180801, Oct 2012.

[27] P. O. Schmidt, T. Rosenband, C. Langer, W. M. Itano, J. C. Bergquist, and D. J. Wineland, "Spectroscopy Using Quantum Logic," *Science*, vol. 309, no. 5735, pp. 749–752, 2005.

[28] D. J. Berkeland, J. D. Miller, J. C. Bergquist, W. M. Itano, and D. J. Wineland, "Minimization of ion micromotion in a Paul trap," *Journal of Applied Physics*, vol. 83, no. 10, pp. 5025–5033, 1998.

[29] J. Stark, "Design ultrastabiler Hochfrequenzfelder für die Langzeitspeicherung hochgeladener Ionen," Master's thesis, Heidelberg University, 2015.

[30] A. D. Ludlow, M. M. Boyd, J. Ye, E. Peik, and P. O. Schmidt, "Optical atomic clocks," *Rev. Mod. Phys.*, vol. 87, pp. 637–701, Jun 2015.

[31] W. Paul, "Electromagnetic traps for charged and neutral particles," *Reviews of Modern Physics*, vol. 62, no. 3, pp. 531–540, 1990.

[32] W. M. Itano, J. C. Bergquist, J. J. Bollinger, and D. J. Wineland, "Cooling methods in ion traps," *Physica Scripta*, vol. 1995, no. T59, p. 106, 1995.

[33] M. K. Oberthaler, "Matter Waves and Light." `https://www.kip.uni-heidelberg.de/kw/image/f/group/f17/files/matterwaves_and_light.pdf`, 2007. Lecture notes; online; accessed 04-October-2018.

[34] W. D. Phillips and H. Metcalf, "Laser Deceleration of an Atomic Beam," *Phys. Rev. Lett.*, vol. 48, pp. 596–599, Mar 1982.

[35] C. Monroe, D. M. Meekhof, B. E. King, S. R. Jefferts, W. M. Itano, D. J. Wineland, and P. Gould, "Resolved-Sideband Raman Cooling of a Bound Atom to the 3D Zero-Point Energy," *Phys. Rev. Lett.*, vol. 75, pp. 4011–4014, Nov 1995.

[36] L. Hornekær and M. Drewsen, "Formation process of large ion Coulomb crystals in linear Paul traps," *Physical Review A*, vol. 66, 2002.

[37] K. Okada, M. Wada, T. Takayanagi, S. Ohtani, and H. A. Schuessler, "Characterization of ion coulomb crystals in a linear Paul trap," *Phys. Rev. A*, vol. 81, p. 013420, Jan 2010.

[38] D. James, "Quantum dynamics of cold trapped ions with application to quantum computation," *Applied Physics B*, vol. 66, pp. 181–190, Feb 1998.

[39] W. Demtröder, *Mechanik und Wärme*. Berlin, Germany: Springer Spektrum, 8. edition ed., 2018.

[40] B. E. A. Saleh and M. C. Teich, *Fundamentals of photonics*. Wiley series in pure and applied optics, Hoboken, N.J.: Wiley, 2. ed. ed., 2007.

[41] T. Hänsch and B. Couillaud, "Laser frequency stabilization by polarization spectroscopy of a reflecting reference cavity," *Optics Communications*, vol. 35, no. 3, pp. 441–444, 1980.

[42] R. W. P. Drever, J. L. Hall, F. V. Kowalski, J. Hough, G. M. Ford, A. J. Munley, and H. Ward, "Laser phase and frequency stabilization using an optical resonator," *Applied Physics B*, vol. 31, pp. 97–105, Jun 1983.

[43] E. D. Black, "An introduction to Pound–Drever–Hall laser frequency stabilization," *American Journal of Physics*, vol. 69, no. 1, pp. 79–87, 2001.

[44] M. Schwarz, *Lasermanipulation von rotationsgekühlten Molekülionen in einer neuen kryogenen Paul-Falle*. PhD thesis, Heidelberg University, 7 2012.

[45] H.-Y. Lo, J. Alonso, D. Kienzler, B. C. Keitch, L. E. de Clercq, V. Negnevitsky, and J. P. Home, "All-solid-state continuous-wave laser systems for ionization, cooling and quantum state manipulation of beryllium ions," *Applied Physics B*, vol. 114, no. 1, pp. 17–25, 2014.

[46] A. C. Wilson, C. Ospelkaus, A. P. VanDevender, J. A. Mlynek, K. R. Brown, D. Leibfried, and D. J. Wineland, "A 750-mW, continuous-wave, solid-state laser source at 313 nm for cooling and manipulating trapped 9Be+ ions," *Applied Physics B*, vol. 105, pp. 741–748, Dec 2011.

[47] S. Feuchtenbeiner, "Lasersysteme für die Präzisionsspektroskopie sympathetisch gekühlter hochgeladener Ionen," Master's thesis, Heidelberg University, 2015.

[48] C. J. Foot, *Atomic physics*. Oxford master series in physics, Oxford ; New York: Oxford University Press, 2005.

[49] Fast ComTec GmbH, Oberhaching, Germany, *7072T Dual Timing 500ns ADC User Manual*, 2009.

[50] High Finesse, Tübingen, Germany, *Wavelength Meter Ångstrom WS Ultimate 10 - User Manual*, 2011.

[51] Thorlabs, Dachau, Germany, *HRS015 Stabilized Red HeNe Laser User Guide*, 2015.

[52] J. Stark. Private communication.

[53] Lake Shore Cryotronics, Inc., Westerville, Ohio, USA, *Silicon Diode - Calibration Certificat*, 2016.

[54] B. T. Matthias, T. H. Geballe, and V. B. Compton, "Superconductivity," *Rev. Mod. Phys.*, vol. 35, pp. 1–22, Jan 1963.

[55] V. Mäckel, R. Klawitter, G. Brenner, J. R. Crespo López-Urrutia, and J. Ullrich, "Laser Spectroscopy on Forbidden Transitions in Trapped Highly Charged Ar^{13+} Ions," *Phys. Rev. Lett.*, vol. 107, p. 143002, Sep 2011.

[56] T. Leopold, L. Schmöger, S. Feuchtenbeiner, C. Grebing, P. Micke, N. Scharnhorst, I. D. Leroux, J. R. C. López-Urrutia, and P. O. Schmidt, "A tunable low-drift laser stabilized to an atomic reference," *Applied Physics B*, vol. 122, p. 236, Aug 2016.

Erklärung

Ich versichere, dass ich diese Arbeit selbstständig verfasst und keine anderen als die angegebenen Quellen und Hilfsmittel benutzt habe.

Heidelberg, den 17.10.2018